Dissertation

submitted to the
Combined Faculties for the Natural Sciences
and for Mathematics
of the Ruperto-Carola University of Heidelberg, Germany

for the degree of

Doctor of Natural Sciences

Put forward by

Dipl.-Phys. Sabri Rahmouni
Born in Waiblingen, Germany

Oral examination: July 26th, 2013

Poly(ethylene glycol) Micropillar Arrays as Force Sensors for Biophysical Applications

Referees: Prof. Dr. Joachim P. Spatz
Prof. Dr. Ulrich S. Schwarz

Poly(ethylene glycol) Micropillar Arrays as Force Sensors for Biophysical Applications

Forces play a crucial role in the regulation and function of biological processes. One of the most commonly used tools for measuring forces are elastic micropillars made of poly(dimethylsiloxane). By using poly(ethylene glycol) (PEG) micropillars, several new experimental approaches could be developed. The aim of this thesis was the enhancement and the experimental application of these PEG micropillars. Not only the achievable geometries, but also the functionalization potential was significantly enhanced. For this, the PEG micropillar fabrication was combined with the transfer of hexagonal gold nanoparticle structures to PEG hydrogels. As a result, PEG micropillars exhibiting gold nanoparticle structures on their tops were obtained. These gold nanoparticles can serve as anchor points for a variety of proteins or other biologically active compounds. To study integrin dependent cell adhesion they were functionalized with $\alpha_v\beta_3$- or $\alpha_5\beta_1$-integrin selective peptidomimetics. Cell experiments showed that fibroblasts exerted higher maximum forces on the $\alpha_5\beta_1$-integrin selective ligand than cells on the $\alpha_v\beta_3$-integrin ligand. These observations were supported by higher local zyxin densities in adhesion clusters and the analysis of further proteins involved in the adhesion process. Furthermore, the achievable PEG pillar force resolution of $9 \pm 2\,\mathrm{pN}$ was demonstrated by investigating the contractile forces of *in vitro* actin networks bundled by magnesium ions.

Poly(ethylen glycol) Mikrosäulenfelder als Kraftsensoren für biophysikalische Anwendungen

Kräfte spielen eine der zentralen Rollen bei der Regulierung und Funktion von biologischen Prozessen. Ein weit verbreitetes Hilfsmittel zur Messung von Kräften sind elastische Mikrosäulen aus Poly(dimethylsiloxan). Durch die Verwendung von Poly(ethylen glycol) (PEG) Mikrosäulen wurden diverse neue experimentelle Möglichkeiten entwickelt. Ziel der vorliegenden Arbeit war die Weiterentwicklung und der experimentelle Einsatz solcher PEG-Mikrosäulen. Dabei wurden nicht nur die erreichbaren Geometrien verbessert sondern vor allem die Funktionalisierungsmöglichkeiten beträchtlich erweitert. Hierzu wurde die PEG-Mikrosäulenherstellung mit dem Transfer von hexagonalen Goldnanopartikelstrukturen auf PEG-Hydrogele kombiniert. Das Resultat waren PEG-Mikrosäulen mit Goldnanopartikelstrukturen auf der Oberseite. Diese Goldnanopartikel können als Ankerpunkte für eine Vielzahl von Proteinen oder anderen biologisch aktiven Substanzen fungieren. Um das integrinabhängige zelluläre Adhäsionsverhalten zu untersuchen, wurden PEG-Mikrosäulen mit $\alpha_v\beta_3$- oder $\alpha_5\beta_1$-Integrin selektiven Peptidmimetica funktionalisiert. Zellexperimente zeigten, dass Fibroblasten auf den $\alpha_5\beta_1$-Integrin selektiven Liganden höhere maximale Kräfte auf die Säulen ausüben können als Zellen auf der $\alpha_v\beta_3$-Integrin Variante. Diese Beobachtungen konnten durch lokal erhöhte Zyxin-Konzentrationen und Untersuchungen von weiteren Proteinen, die im Adhäsionsprozess involviert sind, unterstützt werden. Des Weiteren wurden die Kräfte von *in vitro* Aktinnetzwerken untersucht, welche durch Magnesiumionen zur Kontraktion gebracht wurden. Damit konnte die erreichbare Kraftauflösung von $9 \pm 2\,\mathrm{pN}$ gezeigt werden.

Contents

List of Abbreviations

ADP	adenosine diphosphate
AFM	atomic force microscope/microscopy
ATP	adenosine triphosphate
CAM	cell adhesion molecule
cRGD	cyclic arginylglycylaspartic acid
ctc	center-to-center
ECM	extracellular matrix
FAK	focal adhesion kinase
GPPP	gold nanoparticle PEG pillar
MEF	mouse embryonic fibroblast
PBS	phosphate buffered saline
PDMS	poly(dimethylsiloxane)
PEG	poly(ethylene glycol)
PEG-DA	poly(ethylene glycol) diacrylate
PTFE	poly(tetrafluorethylene)
rpm	rounds per minute
TRITC	tetramethylrhodamineisothiocyanate
SEM	scanning electron microscope/microscopy
Rac1	ras-related C3 botulinum toxin substrate 1
REF	rat embryonic fibroblasts
RGD	arginylglycylaspartic acid
RhoA	ras homolog gene family, member A
UV	ultra violet
YFP	yellow fluorescent protein

Chapter 1

Introduction and Motivation

Force generation is essential for all living organisms. Walking men, flying insects or swimming bacteria all share, despite their differences in size, appearance and force applications, the same microscopic motor proteins as their basic force generators. These motor proteins operate either in highly organized macroscopic muscle cell assemblies or downscaled, in cooperation with actin filaments, as part of the cytoskeleton of single cells.

Equally important as the generation of forces is their transfer to the desired position or target. On the macroscopic scale the mediating connections can be directly observed and understood. On the microscopic scale of single cells, however, this task is much more demanding. The most prominent force transmitting connections of cells to their surrounding are focal adhesions. They consist of complex protein clusters, whose exact properties and abilities exceed the functions of a simple connection point by far. The interplay between these focal adhesions, their protein composition and their influence on force generation are a challenging area of research and part the mechanobiology.

Mechanobiology seeks to gain a fundamental understanding of the correlations between forces and their effects from single cells over tissues and organs to the entire organism. At the cellular level, there are two main regions of interest, force generation and transmission from cells to their surroundings and, the opposite direction, the influence of external forces on cells. For traction force studies it is crucial to have reliable force measurement tools, as well as control over the interface between cells and the measurement devices. In the last years, several approaches were developed for this purpose.

The first qualitative observations of traction forces were achieved by A. K. Harris et al. in 1980 [52]. Fibroblasts seeded on a thin silicon rubber layer caused a wrinkling of the substrate due to the forces exerted by the cells, as shown in Figure 1.1 a. However, the complex correlation between wrinkle size and the actual force values made it impossible to draw clear conclusions about the acting forces.

Based on the same principles of measuring forces by the deformation of flat elastic substrates

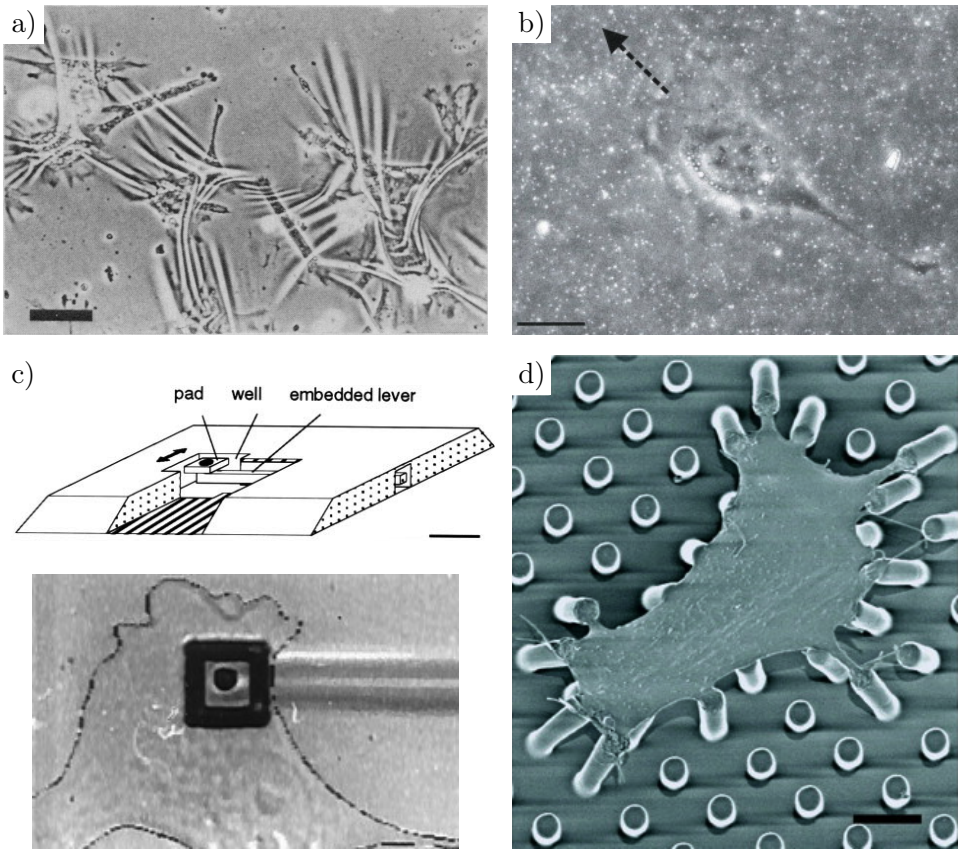

Figure 1.1: Milestones in the development of instruments for cellular traction force studies. The forces were observed by monitoring: a) wrinkling of a thin silicon rubber layer [52], b) displacement of fluorescent microbeads in a gel [102], c) deflection of a horizontal cantilever with an "adhesion pad" at its end [41] and d) deflection of elastic pillar arrays [157]. Scale bars are a) 100 µm, b) 20 µm, c) 10 µm and d) 10 µm.

more sophisticated traction force microscopy techniques were developed [24, 102]. Therefore, thick elastic gels with embedded fluorescence microbeads were used (see Figure 1.1 b). Adherent cells deform the gel and thus displace the incorporated beads. The quantification was achieved by transforming the matrix deformations observed by the bead displacement into traction stress, thus force per area [25]. Solving the mathematical transformation was a very demanding task, due to the inherent noise sensitivity and the fact that it does not have a unique solution. There were several theoretical methods developed to overcome these issues [7, 12, 142], but the fundamental noise sensitivity of the transformation between the deformation field and the force field persisted.

To allow a more direct measurement of the forces C. G. Galbraith and M. P. Sheetz designed bendable horizontal cantilevers with an 4 to 25 μm^2 sized pad at their ends as shown in Figure 1.1 c [41]. Adherent cells deflected these pads and with the known cantilever spring constant

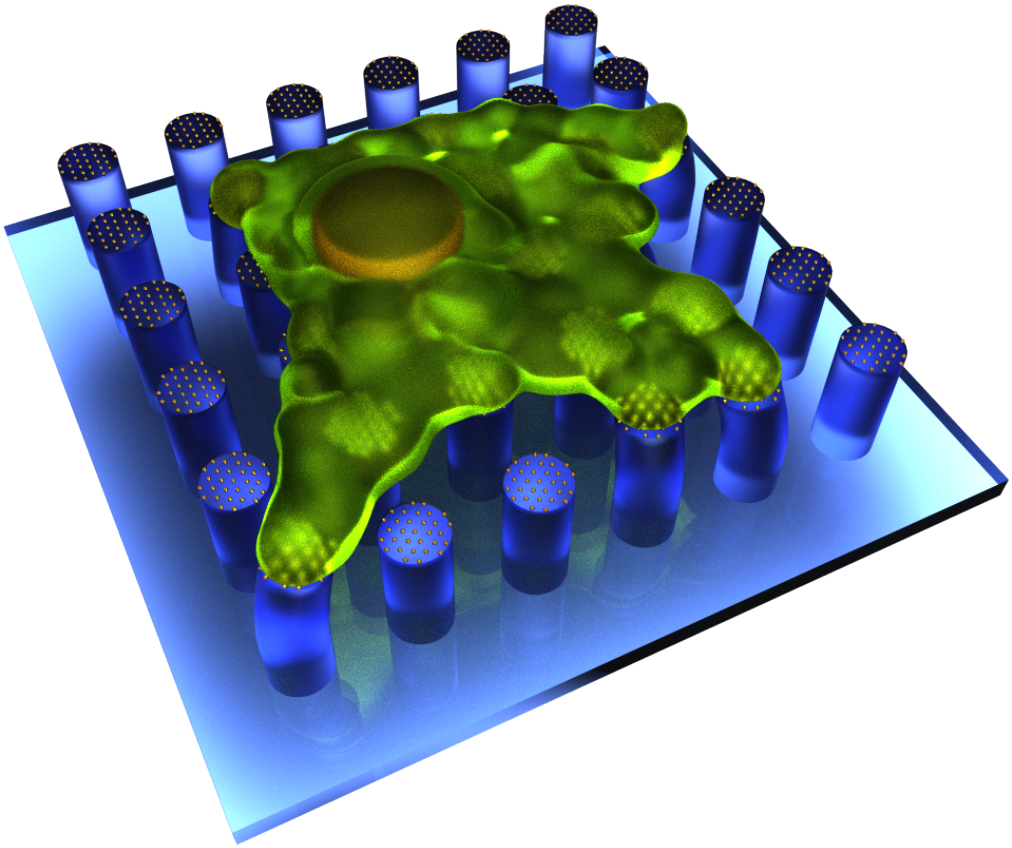

Figure 1.2: 3D rendered image of a cell spreading on an GPPP array, illustrating the working principle of the GPPPs. The gold nanoparticles on the PEG pillars can be functionalized with adhesion mediating ligands, allowing the cell to adhere only to the pillar tops. With the known spring constant of the pillars and by measuring the pillar deflection the exerted forces can be calculated.

and the detected deflection, the force was determined. The shortcomings of these systems were the complex fabrication, associated with a low density of force sensors and the ability to measure forces only perpendicular to the cantilevers. Following the same idea, arrays of flexible micro pillars were developed consisting of etched silicon wafers [119] or the meanwhile widely used elastic polymer poly(dimethylsiloxane) (PDMS) (see Figure 1.1 d) [157].

Micropillar systems are well established and have provided a lot of new insights into the force generation and adhesion relations of cells [28, 39, 44, 158]. To achieve a reproducible adhesion of the cells the pillars tops had to be functionalized with adhesion mediating proteins. This was necessary due to the fact that adherence of cells to bare PDMS is highly dependent on the chemical or physical surface treatments [78]. The proteins are either incubated on the pillar fields or applied by micro contact printing techniques [165]. In both cases the proteins are not covalently bound to the PDMS, but physisorbed on the pillars. Furthermore, PDMS can have

a Young's modulus as low as 5 kPa [111], but the casting mold fabrication techniques used for the PDMS pillar arrays prohibit the usage of such soft PDMS and limit its Young's modulus to values above 300 kPa. This restricts the possible combinations of pillar geometry, spring constant and Young's moduli.

In this thesis, the development and application of gold nanoparticle functionalized poly(ethylene glycol) micro pillars (GPPPs) is presented. By combining poly(ethylene glycol) (PEG) micropillars [83, 135] and gold nanoparticle structuration [86] the micropillar approach was greatly enhanced (see Figure 1.2). This novel technique allows not only to select the spring constant in a wider range than earlier micropillar systems without changing the geometry, but also gives control over parameters like ligand type, density and spacing. In addition, PEG has the inherent property of being protein repellent thereby prohibiting unspecific adhesion.

GPPP arrays were functionalized with ligands which only allow the binding to one of two different integrin heterodimers, one of the most important focal adhesion proteins. Cell experiments on these GPPPs revealed significant differences in the force generation and protein recruitment behavior of adherent cells.

Furthermore, highly sensitive PEG pillars were used to investigate the motor protein free force generation of contractile *in vitro* actin networks, proving the applicability of the PEG pillars in force regimes below 100 pN.

Chapter 2

Theoretical Background

This chapter covers the theoretical background necessary for the development, evaluation and execution of the presented experiments, as well as the basic principles of the involved biological and biophysical processes. The sections are divided into two categories: biological informations and biophysical or mathematical derivations. Outlined biological topics are the cellular adhesion with its most prominent processes, parts and proteins, cellular force generation and the properties of actin filaments. Physical and biophysical subjects include beam theory, theoretical description of adhesion processes, particle tracking and myosin-independent force generation of simple actin filament configurations. Furthermore, the material properties of poly(ethylene glycol), as the main fabrication material of the PEG pillars, are briefly described.

2.1 Pillars as Force Sensors

Pillars and pillar arrays can be used as force sensors by correlating their deflection to an acting force. Therefore, two essential values have to be identified, the pillar spring constant and the position of the pillar top. The spring constants of pillars can be calculated (for small deflections) based on the bending beam theory. For the efficient and precise localization of the pillar top position image analysis algorithms allow a subpixel tracking. The theoretical principles behind these two essential parts are briefly outlined in the following two sections.

2.1.1 Beam Theory

Pillar bending and the acting forces can be derived from the Euler-Bernulli beam equation [74]:

$$\frac{\mathrm{d}^2}{\mathrm{d}z^2}\left(EI\frac{\mathrm{d}^2x}{\mathrm{d}z^2}\right) = \omega \tag{2.1}$$

with E being the Young's modulus, I the second moment of the area, x the deflection of the beam at the position z and ω the load distribution ($^{\text{force}}/_{\text{unit length}}$). In the case of a cylindrical

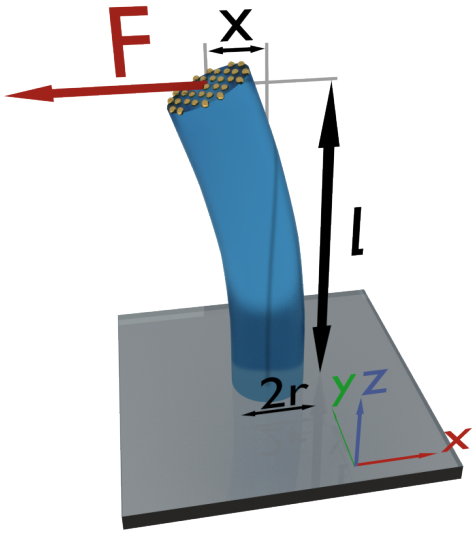

Figure 2.1: Illustration of a pillar bent by a horizontal force F acting only on the pillar top. The parameters needed for the derivation of the relation between deflection x, the applied force F, the pillar length l and its radius r are shown.

pillar the Young's modulus E, the cross section as well as I do not change along z, so equation 2.1 can be simplified to:

$$EI\frac{\mathrm{d}^4x}{\mathrm{d}z^4} = \omega \tag{2.2}$$

The derivatives of the pillar deflection x represent the following properties of the system:

$$\begin{aligned} \frac{\mathrm{d}x}{\mathrm{d}z} &\mathrel{\widehat{=}} \text{slope of the pillar} \\ EI\frac{\mathrm{d}^2x}{\mathrm{d}z^2} &\mathrel{\widehat{=}} \text{bending moment } M \end{aligned} \tag{2.3}$$

The bending moment M of the pillar with a length l, a fixed end at $z = 0$ and a free end at $z = l$ on which a force F is acting perpendicular to z can be written (for deflections $< 5°$ and aspect ratios of $1:10$) as

$$M = F\,(l - z)\,. \tag{2.4}$$

Together with equation 2.3 this leads to the differential equation

$$EI\frac{\mathrm{d}^2x}{\mathrm{d}z^2} = F\,(l - z)\,. \tag{2.5}$$

Dividing by $\mathrm{d}z^2$ as well as EI and factoring out l leads to

$$\mathrm{d}^2x = \frac{Fl}{EI}\left(1 - \frac{z}{l}\right)\mathrm{d}z^2. \tag{2.6}$$

After integrating twice this leads to

$$x\,(z) = \frac{Fl}{EI}\left(\frac{z^2}{2} - \frac{z^3}{6l}\right) + c_1z + c_2. \tag{2.7}$$

Due to the fact that one end is fixed, the slope $\mathrm{d}x/\mathrm{d}z$ and the deflection x have to be zero at $z = 0$, which means for the integration constants c_1 and c_2:

$$\left.\frac{\mathrm{d}x}{\mathrm{d}z}\right|_{z=0} \stackrel{!}{=} 0 \quad \Rightarrow \quad c_1 = 0 \tag{2.8}$$

$$x\,(z=0) \stackrel{!}{=} 0 \quad \Rightarrow \quad c_2 = 0 \tag{2.9}$$

With these boundary conditions equation 2.7 can be simplified to

$$x\,(z) = \frac{Fl}{EI}\left(\frac{z^2}{2} - \frac{z^3}{6l}\right). \tag{2.10}$$

For forces only exerted at the top of the pillar and perpendicular to it, the height value $z = l$ and equation 2.10 can be reduced to

$$x\,(l) = \frac{Fl^3}{3EI}. \tag{2.11}$$

The only unknown part of the equation 2.11 is the second moment of area I, which can be calculated from the pillar cross section by the integral over the elemental area $\mathrm{d}A$. That means

$$I = \int_A x^2\,\mathrm{d}A \tag{2.12}$$

in an cartesian coordinate system. Since the pillar has a cylindrical shape, the integral is solved by using the polar coordinates $x = \rho\sin\phi$ and $\mathrm{d}A = \rho\,\mathrm{d}\rho\,\mathrm{d}\phi$, transforming equation 2.12 into

$$I = \int_0^{2\pi}\mathrm{d}\phi\int_0^r \mathrm{d}\rho\,\rho^3\sin^2\phi = \frac{\pi}{4}r^4. \tag{2.13}$$

With this result for I and equation 2.11 the deflection of the pillar can be calculated by

$$x = \frac{4Fl^3}{3\pi Er^4}. \tag{2.14}$$

The right side of this equation contains only constants and the force F similar to Hook's law $F = -kx$ with k being the spring constant. In the case of a cylindric pillar the spring constant is

$$k = \frac{3\pi Er^4}{4l^3}, \tag{2.15}$$

containing only constants and the geometric values r and l of the pillar, as well as the pillar Young's modulus E. Formulated like Hook's law this leads to

$$F = \frac{3\pi Er^4}{4l^3}x, \tag{2.16}$$

allowing the calculation of the acting forces by observing the deflection x after identifying the geometric (r, l) and physical property (E) of the pillar.

This whole derivation has some approximations and assumptions involved, as it holds only true for small deflections ($< 5°$), aspect ratios of $1:10$ or higher and does note take shear forces inside the pillar into account. There are more sophisticated calculations which provide more accurate solutions, but they are also much harder to apply to the experimental conditions [80, 167]. The calibration procedure described in section 3.5 revealed that the fabrication process for the PEG pillar led to a too high variety in the Young's moduli E to be able to just calculate the spring constants by equation 2.15. Therefore, all pillar fields used as force sensors had to be calibrated thus it was not necessary or advantageous to use or adapt any of the more sophisticated bending models. To estimate the Young's modulus E of calibrated pillars we used the equation 2.15 by solving it for E.

2.1.2 Particle Tracking

Traction force measurements rely on the ability to track deflections. Furthermore, the tracking accuracy defines, together with the spring constant, the achievable force resolution. This makes the tracking algorithms to one essential part of the force evaluation, especially in the nanonewton and subnanonewton regime.

Both tracking software solutions used for the force evaluations (see section 3.9 and section 4.2) are based on the algorithm of J. C. Crocker and D. G. Grier [20]. Basically, the algorithm achieves its subpixel particle positioning precision by the following steps.

First, the image with the intensities $A(x, y)$ is improved by subtracting the boxcar average

$$A_w(x, y) = \frac{1}{(2w+1)^2} \sum_{i,j=-w}^{w} A(x+i, y+j) \tag{2.17}$$

with w being an integer value bigger than the particle radius in pixel. This value $A_w(x, y)$ is the mean intensity of $A(x, y)$ in a quadratic area with the side length $2w + 1$ pixel around the center point (x, y). By subtracting $A_w(x, y)$ from $A(x, y)$ the background intensity surrounding the particle is reduced. To reduce the noise in the image it is convoluted by a Gaussian surface with the width $\lambda = 1$ pixel. This value was chosen, due to the random nature of the image noise resulting in a correlation length of one pixel.

$$A_\lambda(x, y) = \frac{1}{B} \sum_{i,j=-w}^{w} A(x+i, y+j) \cdot e^{-\frac{i^2+j^2}{4\lambda^2}} \tag{2.18}$$

with the normalization factor

$$B = \left[\sum_{i=-w}^{w} e^{-\frac{i^2}{4\lambda^2}} \right]^2 . \tag{2.19}$$

The convolution leads to a smoothening to the image but does not reduce the final particle positioning significantly. Both steps can be combined to one convolution kernel

$$K(i,j) = \frac{1}{K_0} \left[\frac{1}{B} e^{-\frac{i^2+j^2}{4\lambda^2}} - \frac{1}{(2w+1)^2} \right] \tag{2.20}$$

with the normalization factor

$$K_0 = \frac{1}{B} \left[\sum_{i=-w}^{w} e^{-\frac{i^2}{4\lambda^2}} \right]^2 - \frac{B}{(2w+1)^2}. \tag{2.21}$$

Following these image enhancements steps the pixels with the highest local intensities are chosen to be the first rough positions of the particles. Around every position a circular area with the radius $w = \sqrt{i^2 + j^2}$ is defined. For each of these particle positions (x, y) the intensity centroid offset (ϵ_x, ϵ_y) of the intensity values within the sphere area can be calculated by

$$\begin{pmatrix} \epsilon_x \\ \epsilon_y \end{pmatrix} = \frac{1}{m_0} \sum_{i^2+j^2 \leq w^2} \begin{pmatrix} i \\ j \end{pmatrix} A(x+i, y+j). \tag{2.22}$$

Here, m_0 is the sum of the intensities within the spherical area. The new, and more accurate position can then be calculated by adding the shift to the previously rough estimated position. This then leads to the final particle position ($x+\epsilon_x$, $y+\epsilon_y$), giving them a subpixel precision. One crucial experimental point is that no saturated pixels are involved in the centroid calculation process, since they would distort the subpixel position calculation.

2.2 Properties of Poly(ethylene glycol) and Poly(ethylene glycol) diacrylate

Poly(ethylene glycol) (PEG) is the polymer obtained by the polycondensation of ethylene glycol Figure 2.2. Despite its very simple form, PEG has many useful and exceptional properties. PEG is transparent for visible light, flexible, non-toxic and biocompatible but protein repellent. Due to its properties, PEG is used in many cosmetic, pharmaceutic and biotechnology products like contact lenses, creams, toothpaste, drug carrier or medical implants.

To form 3D-hydrogel network structures and still retain the before mentioned properties, PEG chains with two acrylate groups (poly(ethylene glycol) diacrylate, PEG-DA) at their chain ends are cross-linked to a mesh structure by a radical initiator (see Figure 3.5). This

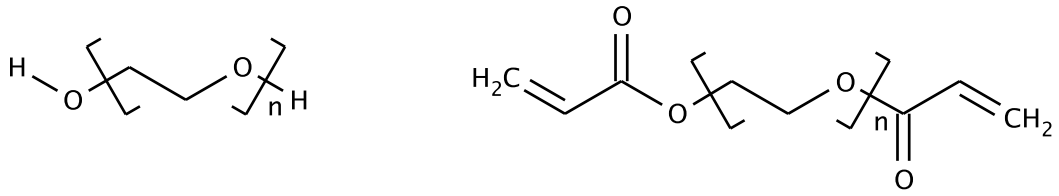

Figure 2.2: Chemical structures of poly(ethylene glycol) (left) and poly(ethylene glycol) diacrylate (right).

enabled a controlled photopolymerization of the PEG-DA by using a radical starter molecule which is cleaved by UV illumination [124, 125]. These experimental approaches were improved to achieve the PEG pillar fabrication described in section 3.4. The PEG chain length of the PEG-DA has a direct influence on the physical properties of the resulting hydrogel. In general, a longer PEG chain results in a softer hydrogel. Longer PEG chains form bigger mesh sizes and less cross connections (formed by the acrylate groups), leading to a more flexible network. By choosing the PEG chain length according to the wished Young's modulus E, the pillar spring constants can be varied without changing the geometry as can be directly seen in the equation 2.15. Atomic force microscopy (AFM) indentation measurements of different bulk PEG hydrogels have shown possible Young's moduli between approximately 1 kPa and 10 MPa [87].

The origin of the protein repellent properties of PEG are still a matter of debate. There are theories trying to explain possible reasons, but none of them is totally compelling. The most widespread models fore the explanation are:

- **Free energy theory:** The free energy of the interface between water and PEG is near its minimum, leading to a very low driving force to react with other materials [18]. But other polymers show the same water interface behavior and are not protein repellent.

- **Steric repulsion theory:** PEG chains are very hydrophilic and have a high solubility in water, allowing PEG chains on the surface to move very rapid in water. This leads to very short contact times between proteins and surface minimizing the reaction probability [66, 77].

- **Volume restriction theory:** Under the assumption that PEG surfaces show a dense brush-like structure of PEG chains on the surface, an approaching object, too large to penetrate between them, would have to confine the space of the PEG chains. Entropically this is unfavorable for the system [77]. However, also the PEG-DA networks show the protein repellent behavior despite their shorter length and, due to the network structure, less dense and shorter brush-like surface.

- **Exlusion of volume theory:** If a protein or an object coated with proteins is approaching the brush-like PEG surface, as described in the "volume restriction theory", an enthalpy effect might also play a role [77]. The PEG-water interactions are then replaced by PEG-protein interactions, which are disadvantageous for the hydrophilic PEG.

Other experiments showed that the conformation of the PEG chains also plays a crucial role regarding its protein repellent character. While amorphous or helical conformations on surfaces repel proteins, "all-trans" conformations absorb proteins [51]. Theoretical calculations and simulations also confirmed that the high affinity of helical or amorphous PEG to water prevents the approach of proteins to the surface and thus repel them [117, 164].

2.3 Cellular Adhesion

In general, cellular adhesion can be divided into two main groups: cell-cell adhesion and cell-matrix adhesion. All multicellular organisms rely on the interplay of these two adhesion types influencing and controlling the differentiation, movement and death of single cells or groups of cells [1].

In a simplified view, the formation of adhesion sites involves two steps. First, individual cell adhesion receptors, located on the outer part of the cell membrane, bind to their compatible counterpart, the ligands, located either on the extracellular matrix (ECM) or on another cell. After this initial step, dependent on the adhesion type, a variety of proteins are recruited, building an adhesion cluster and stabilizing the connection.

The first binding for the formation of an adhesion cluster is usually achieved by transmembrane proteins, also called cell adhesion molecules (CAMs). They commonly have three main parts, the intra- and extracellular domains linked by the transmembrane domain. Both CAM termini have their distinct function. The intracellular domain recruits further proteins within the cell depending on the purpose of the CAM. Extracellular domains can either form a homophilic binding to CAMs of the same kind or a heterophilic binding by connecting to other CAMs or the ECM. Additional to their tissue forming and stabilization function, the CAMs are also signaling molecules. They deliver information about the ECM (e.g. mechanical or chemical properties) and arrange a cell-cell communication.

In general the CAMs can be subdivided into five superfamilies: cadherins and immunoglobulins which form homophilic cell-cell adhesions, selectins which heterophilically bind to other CAMs amongst others mucins and integrins. Integrins are the most important CAMs for the cell-matrix contact. They play a crucial role in the formation of focal adhesions and in the mechanotransduction of forces between the cytoskeleton and the ECM. Furthermore, integrins are involved in different signaling pathways and transductions.

A main part of this work deals with the different roles and abilities of distinct integrin types

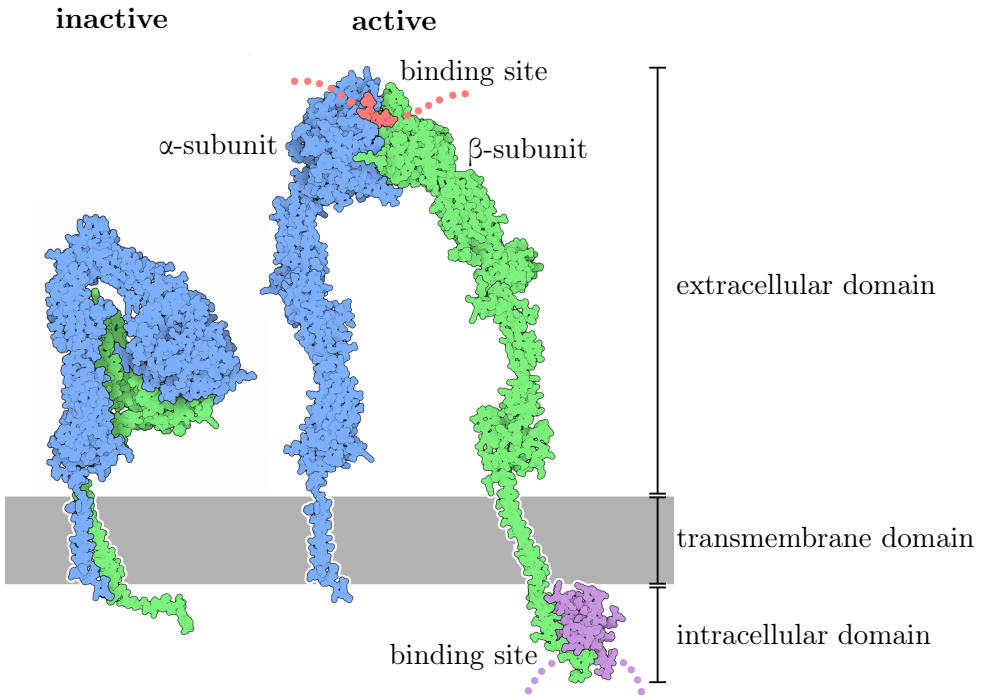

Figure 2.3: Structure and conformation of an inactive (folded, left) and active (unfolded, right) integrin. All integrins share the basic structure as a heterodimer consisting of an α- and β-subunit. A small cytoplasmic tail is connected through the transmembrane domain with the much larger extracellular part. Adapted from [46].

(namely $\alpha_v\beta_3$- and $\alpha_5\beta_1$-integrin). Therefore, the next sections will provide more insight into this special subtype of CAMs.

2.3.1 Integrins and Focal Adhesion

The main function of integrins, as transmembrane proteins, is to provide a physical connection between the cytoskeleton and the ECM. These connections are necessary for the cell motility, stability and force transmission from or to the ECM. Furthermore, integrins not only transduce mechanical properties or deformations from the ECM to the intracellular space [42], but also act as bidirectional mediators for cell signaling between the ECM and the cell [43, 62]. Integrin signaling influences differentiation, proliferation, apoptosis and the cell cycle [105].

Integrins consist of an α- and β-subunit noncovalently connected forming heterophilic heterodimers. Since there are 18 different α- and 8 different β-subunits and due to the fact that not all combinations are possible, a total number of 24 integrin dimers exist. All of these 24 integrins can bind with specific affinities to adhesion sites or ligands at the ECM [60]. As depicted in Figure 2.3, the extracellular domain of the integrin, also called head group, represents the bigger part of the heterodimer, establishing the connection to the ECM. The inner shorter

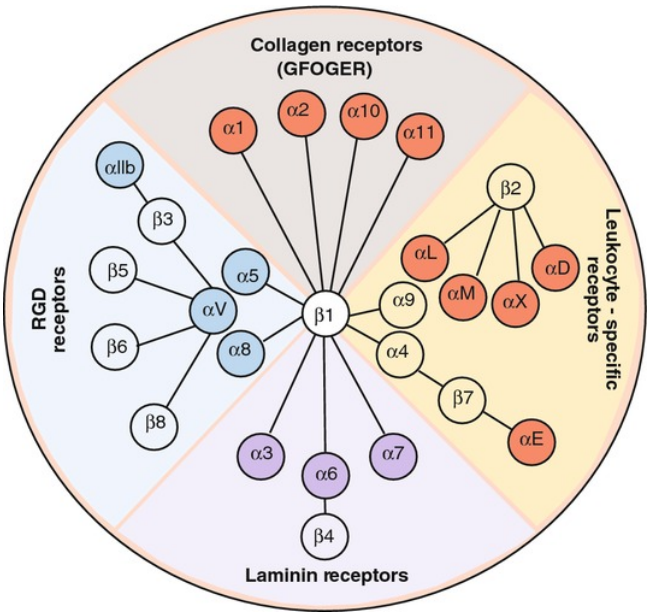

Figure 2.4: An overview of all integrin α- and β-subunit combinations and their ECM binding partners. As can be seen not all combinations of integrin heterodimers exist in nature [6].

domain mediates the connection to the cytoskeleton. To allow binding to different parts of the ECM, cells typically express several different integrins.

Since all specific interactions in biological systems are noncovalent (further discussed in subsection 2.5.1) the only way to achieve a connection with similar or higher strength than a covalent bond is accomplished by aggregation of several single integrin-ECM-connections forming an adhesion cluster. The formation of these adhesion clusters has several benefits for the cell. A force acting on the adhesion site is homogeneously distributed over the whole cluster reducing the unbinding probability of single bonds. In the case of a bond breakage, the probability of the connection to reestablish is high since the possible binding partner remains close. Due to the high density of integrins, the diffusion in the cluster is reduced which further increases the rebinding probability.

The formation of integrin binding clusters is always strongly connected to a large number (>100) of different intracellular proteins. These proteins have in most cases the potential to interact with multiple other proteins leading to an extremely heterogeneous complex protein with many potential functions [67, 175]. One of these functions is mechanosensing of ECM properties and to react on changes in rigidity [120]. It is still unclear which part exactly is responsible for these mechanosensing capabilities and if it is a small machinery within one adhesion site or an interplay of several adhesion clusters [44, 158].

Like many other proteins, integrins also show different steric conformations. These states comprise an inactive state, where the extracellular head parts are bent towards the cell membrane with no coupling avidity and a fully activated state with high binding avidity [14]. This activation process is still not completely understood and involves several intracellular binding and signaling steps [3, 101, 149].

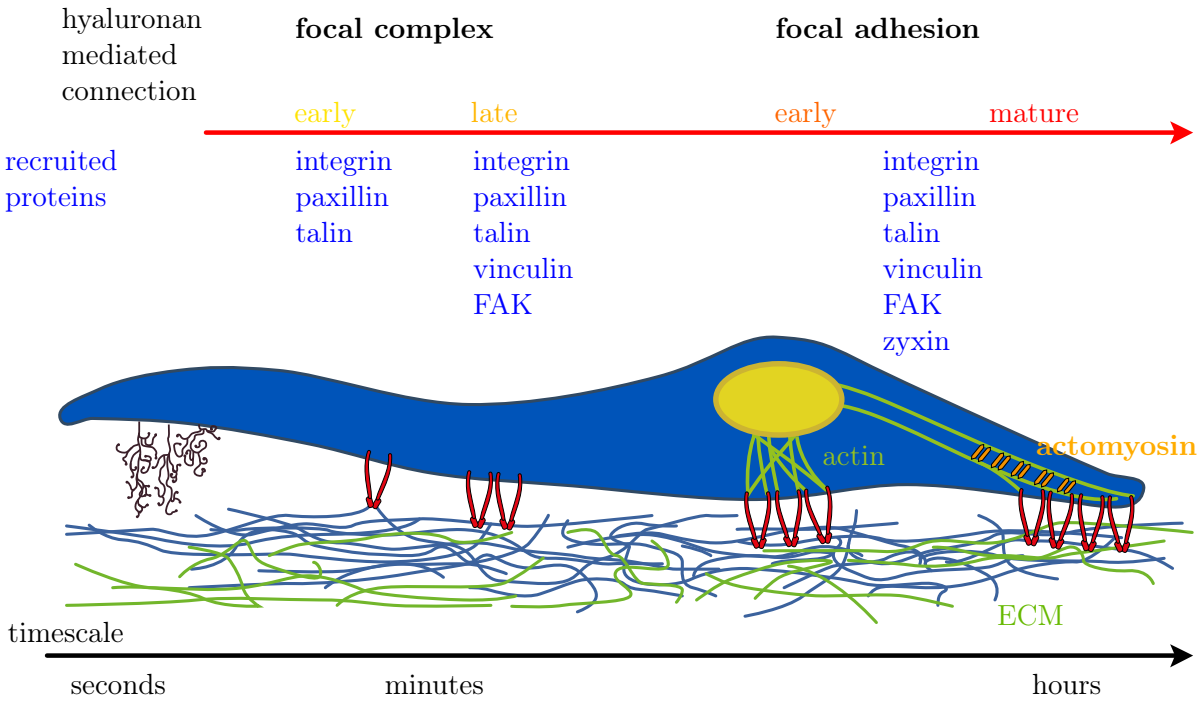

Figure 2.5: This figure illustrates the temporal development of a cellular adhesion (from left to right). First the cell touches the ECM via its hyaluronan mesh which can have a thickness of several µm, followed by the connection of single activated integrins to the ECM. The clustering of these integrins leads to a signaling cascade and the recruitment of several proteins listed above which induces the binding of more integrins and the formation of a focal complex. Further recruitment of more integrins and intracellular proteins establishes a connection to the actin cytoskeleton and its actomyosin complexes. The tension exerted by the actin cytoskeleton and the clustering of even more integrins and focal adhesion proteins lead to the maturation of the focal adhesion as a stable but highly dynamic link between the cell and the ECM.

2.3.2 Focal Adhesion Assembly

In an ideal case, focal adhesion assembly follows a linear process. Upon approach of a cell to the ECM, the first contact is mediated by its hyaluronan coat [17]. However, the onset of focal adhesion formation itself begins with the binding of single activated integrins to compatible binding sites at the ECM. With increasing number of bound integrins clustering takes place. This can happen, for example, due to a high availability of specific binding partners at the ECM. The clustering then initiates a signaling cascade within the cell, leading to a binding of proteins like paxillin and talin to the intracellular domains of the integrins, forming a so-called focal complex. A focal complex can then mature thereby recruiting, amongst others, vinculin and FAK. If the location is suitable for adhesion, the signaling initiates the connection of the focal complex to the actin cytoskeleton and the recruitment of zyxin and tensin. This step marks the transition of a focal complex to a focal adhesion. The early focal adhesion can then

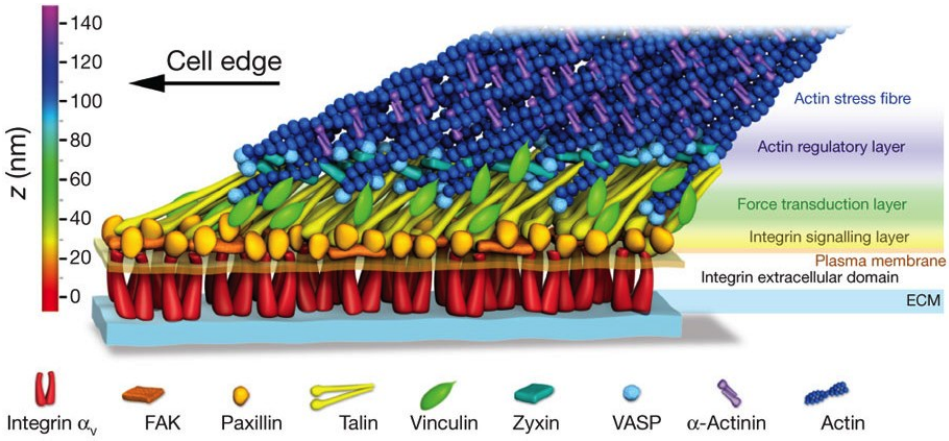

Figure 2.6: Scheme of the most prominent proteins and their assumed location within a focal adhesion [67].

mature and thereby tighten its connection to the actin cytoskeleton via actomyosin stress fibers. In this final stage the focal adhesion represents a stable connection between the ECM and the cytoskeleton, allowing force transductions from the cell to the ECM and vice versa.

A short overview of this process and the most prominent involved proteins is shown in Figure 2.5. The assumed locations of these proteins are depicted in Figure 2.6. As aforementioned there are much more proteins involved in the formation and maturation of adhesions than described above and shown in Figure 2.6 [174].

The main difference between focal complexes and mature focal adhesions are: the size (focal complexes are smaller), the protein composition (e.g. they lack zyxin and tensin) and the fact that they are not connected to the actin cytoskeleton [173, 176]. Besides chemical and ECM properties, also mechanical stimuli can trigger and accelerate the transition from focal complexes to focal adhesions [107, 130, 160].

Mature focal adhesions are despite their role as connection between the ECM and the cytoskeleton a highly dynamic system. This is also true for the integrins as the main connectors between ECM and the inner cell. These integrins are not immobile, but show distinct integrin-type dependent dynamic within focal adhesions [134].

2.3.3 Zyxin

Zyxin, as illustrated in Figure 2.6, is one of the many proteins involved the focal adhesome. It has a molecular weight of 82 kDa and is a member of the LIM domain protein family. Zyxin is also known to be highly involved in the regulation of focal adhesion, motility, mechanotrasduction and actin stress fiber formation [56, 57, 156]. However, zyxin does not interact with actin directly but has binding sites for actin binding proteins like α-actinin or Lasp-1 [81, 128]. As

aforementioned in subsection 2.3.2, zyxin is only present in mature focal adhesions and absent in focal complexes [173].

Moreover, the zyxin localization is correlated to acting forces or tension [79]. This behavior was observed in several experiments. M. Yoshigi et al., for example, exerted external forces on adherent cells either by stretching the substrate or by applying local forces with an atomic force microscope (AFM) cantilever [171]. They found a strong relation between the applied forces and the zyxin localizations. In another experiment, stress fibers within adherent cells were cut by a laser and the zyxin reaction was followed [19]. By comparing the zyxin localization with computer simulations of the tension distributions, a colocalization of zyxin and areas with high calculated tension was found. Both experiments show that zyxin protein clusters at focal adhesion sites or actin stress fibers are correlated with local intracellular tension.

2.3.4 Paxillin

Paxillin is an intracellular focal adhesion protein of 68 kDa molecular weight, which is recruited very early in the focal adhesion formation process. Due to its multi-domain nature, paxillin acts as a mediator between different protein types of the intracellular focal adhesion proteins. It interacts with structural proteins like vinculin or actopaxin, kinases such as FAK, and actin regulators like the Rho family of GTPases [23]. Because of these attributes paxillin is often seen as "scaffold" protein of the focal adhesion complexes.

2.3.5 Characteristics of $\alpha_v\beta_3$- and $\alpha_5\beta_1$-Integrins

One of the main investigations of this work was the analysis of the different adhesion and mechanotransduction properties of $\alpha_v\beta_3$- and $\alpha_5\beta_1$-integrins. As can be seen in Figure 2.4 both integrins bind to the RGD- and PHSRN-motif (Arg-Gly-Asp and Pro-His-Ser-Arg-Asn amino acid sequence) of fibronectin, an ECM protein. However, only $\alpha_v\beta_3$- but not $\alpha_5\beta_1$-integrins can bind to vitronectin [4, 60, 137].

Many different experiments were conducted to investigate the different roles and abilities of these two integrins. A selection of these experiments and their major findings are summarized in the following.

The experiments by P. Roca-Cusachs et al. showed that $\alpha_5\beta_1$-integrin clusters of mouse embryonic fibroblasts bound to fibronectin coated magnetic microbeads sustained high applied forces (in the nanonewton range) [131]. Furthermore, they found out that $\alpha_v\beta_3$-integrin together with talin, only mediated the connection between the $\alpha_5\beta_1$-integrin clusters and the actin cytoskeleton. Their observations suggested, that upon binding to fibronectin, $\alpha_v\beta_3$- and $\alpha_5\beta_1$-integrins have a distinct role in establishing adhesion. $\alpha_5\beta_1$-integrin mediates adhesion strength, while $\alpha_v\beta_3$-integrin is required for reinforcement and mechanotransduction.

O. Rossier et al. investigated with high temporal and spatial resolution the trajectories of

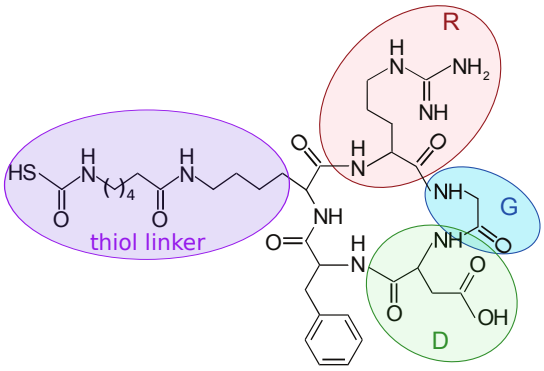

Figure 2.7: Chemical structure of the synthesized cyclic variant of the RGD molecule (cRGD). The three amino acids are arginine (R), glycine (G) and aspartate (D). To enable the binding of the molecule to gold a thiol linker with a length of approximately 2 nm was added to the cRGD.

the two integrin subunits β_1 and β_3 within focal adhesions in a variety of adhesion conditions [134]. They showed that in focal adhesions $\alpha_v\beta_3$-integrins form stationary connections to the ECM. In contrast, their experiments demonstrated a backwards movement of the $\alpha_5\beta_1$-integrins within the focal adhesions. This movement of the $\alpha_5\beta_1$-integrins could enhance the adhesion strength since it was reported that integrins show catch bond behavior [70] and mechanical stimuli can boost the binding strength of integrins [37]. Additionally, by using "chimeric"-integrins with different intra- and extracellular domain combinations, they discovered that only the extracellular domain determines the integrin behavior.

Besides these aforementioned force transduction and localization differences, M. R. Morgan reported that $\alpha_v\beta_3$- and $\alpha_5\beta_1$-integrin mediated adhesions also differ in their intracellular signaling behavior [100]. The change of integrin composition at the adhesion sites affects signaling and starts a feedback cascade regulating, amongst others, integrin recruitment at the adhesion site. For example, as soon as $\alpha_5\beta_1$-integrins start to bind to the ECM in normally $\alpha_v\beta_3$-integrin rich focal complexes, the Rac1-dominated signaling of focal complexes changes to RhoA-dominated GTPase signaling [22]. This causes a further recruitment of $\alpha_5\beta_1$-integrins, maturation to focal adhesions and the reinforcement of the cytoskeleton.

2.4 $\alpha_v\beta_3$- and $\alpha_5\beta_1$-Integrin Peptidomimetics

A large fraction of the integrin family can bind to the RGD motif of different ECM proteins, illustrated in Figure 2.4. The established and widely used chemically synthesized cyclic RGD (cRGD, see Figure 2.7) is specifically recognized by several integrin heterodimers [136, 137]. One way to investigate the impact of integrins *in vitro* is the use of so-called knockout cells. These cells are genetically modified to express only a part of their natural integrin selection.

$\alpha_v\beta_3$-selctive integrin ligand

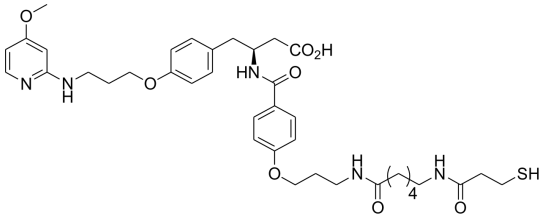

$IC_{50}(\alpha_v\beta_3) = 1.8 \pm 0.7\,\text{nM}$
$IC_{50}(\alpha_5\beta_1) = 130 \pm 19\,\text{nM}$

$\alpha_5\beta_1$-selctive integrin ligand

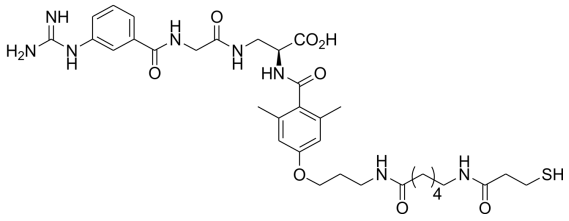

$IC_{50}(\alpha_v\beta_3) = 229 \pm 23\,\text{nM}$
$IC_{50}(\alpha_5\beta_1) = 1.5 \pm 0.09\,\text{nM}$

Figure 2.8: Chemical structure of the two highly selective ligands for $\alpha_v\beta_3$- and $\alpha_5\beta_1$-integrins. To both ligands a linker with a thiol group (lower right of the molecules, length $\approx$ 2 nm) was added to allow the binding of these ligands to gold. Their IC_{50} (half maximal inhibitory concentration) values shows the high selectivity of each of the two ligands for one integrin but not the other. Values and chemical structures from [127].

However, like all genetical modifications, this change also influences other parts of the cell, making the direct examination of the integrin influence very challenging. Another way is to use selected ECM proteins. By choosing for example vitronectin and allowing the binding of $\alpha_v\beta_3$-integrins but not $\alpha_5\beta_1$-integrins, some conclusions of experimental observations can be drawn. However, since other integrins can also bind to these proteins the conclusions cannot be appointed to one specific integrin.

To overcome these shortcomings and allow the investigations of discrete roles and features of the $\alpha_v\beta_3$- and $\alpha_5\beta_1$-integrins, highly selective ligands were developed and synthesized in the group of H. Kessler[1] and kindly provided for the experiments [127]. The design of these ligands to be selective for one but not the other integrin was a big challenge. While the synthesis for a $\alpha_5\beta_1$-integrin specific ligand was straight forward [55], it was demanding to synthesize a ligand for $\alpha_v\beta_3$-integrin with a low affinity to $\alpha_5\beta_1$-integrin [92, 168].

The chemical structure of these two ligands can be seen in Figure 2.8. To immobilize these ligands via gold coupling, a linker chain with a thiol group was added. F. Rechenmacher et al. showed that the addition of these linkers do not significantly affect their activity or selectivity to the integrins [127].

It could also be shown, that cells lacking one or the other integrin could only adhere to surfaces functionalized with the matching selective ligand [127]. Especially this last-mentioned experiment confirmed that the ligands were also functional under cell culture conditions. This an was essential property for the performed experiments described in subsection 4.1.3.

[1] Institute for Advanced Study at the Department of Chemistry, Technische Universität München

2.5 Biophysics of Cell Adhesion

In the year 1978 G. I. Bell came to the conclusion, that non specific electrostatic interactions could not be the only mechanisms leading to the strong interactions he could observe between two cell membranes [8]. To explain his findings he introduced specific biological bonds consisting mostly of van der Waals interactions and hydrogen bonds. The main explanation for the significantly higher stability of these bonds compared to unspecific interactions is the configuration of the binding partners which fit together and form, for example, multiple hydrogen bonds. Since these specific bonds are non covalent even the strongest known specific interaction between streptavidin and biotin (free energy $\approx 35\, k_\mathrm{B}T$) [96] is much weaker than covalent bonds (e.g. carbon-carbon bond with a free energy of $\approx 150\, k_\mathrm{B}T$).

The biophysical examination of cell adhesion can be divided into two essential types of interaction, specific and unspecific [138]. The unspecific interactions with their long range are essential for the first attachment and during motility at the edge of cell (lamellipodia) [173]. Specific short ranged interactions (e.g. between proteins and their correspondent counterpart) are formed for long lasting and more robust connections [61].

Due to their non covalent nature, specific bonds can be established and released relatively easy. This formation and deformation of bonds can be found in many biomolecular interactions like receptors, enzymes, hormones and between antigens and antibodies. In this thesis the main interaction of interest is the binding between integrin receptors and their binding partners or ligands.

2.5.1 Theoretical Considerations about Cell Adhesion

The interaction potential between two specific binding partners can be depicted in a simple one dimensional potential with the potential barrier ΔU (see Figure 2.9 a. H. A. Kramers' theory for the calculation of reaction rates holds also true for the persistence and thermally driven breakage of this simple model bond [72]. This breakage or dissociation rate k_0 meets the proportionality relation

$$k_0 \propto \frac{1}{t} e^{\Delta U / k_\mathrm{B}T}. \tag{2.23}$$

The time t represents the average transition time of a state across the potential barrier, ΔU is the potential barrier height, k_B the Boltzmann constant and T the equilibrium temperature.

If an external constant force is applied on the bond the potential is bent as can be seen in Figure 2.9 b. This results in a lower potential barrier ΔU and with it to a higher dissociation rate k_0. The force F dependent dissociation rate k_{off} can be calculated by

$$k_{off} = k_0 e^{F/F_b} \tag{2.24}$$

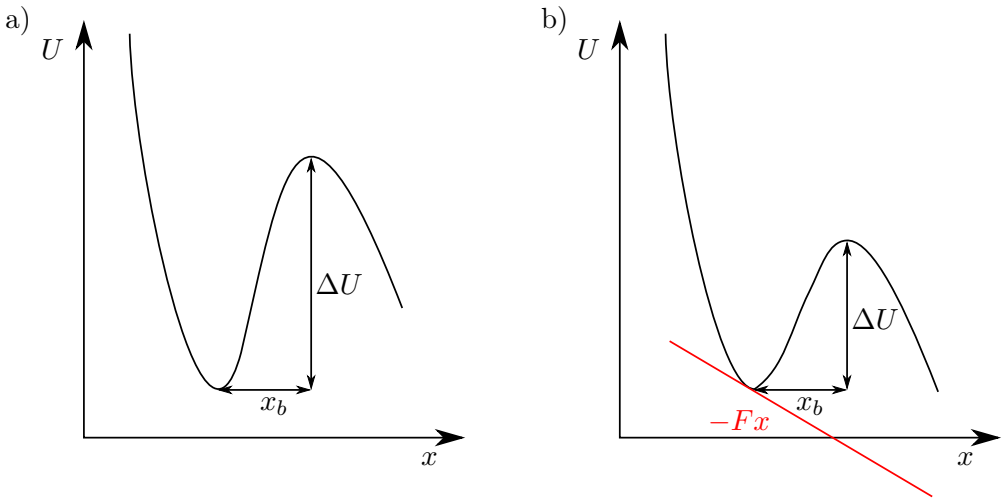

Figure 2.9: These schematic graphs show two one dimensional potentials with a barrier ΔU: a) undistorted case; b) potential barrier lowered under the influence of a constant force $-F$.

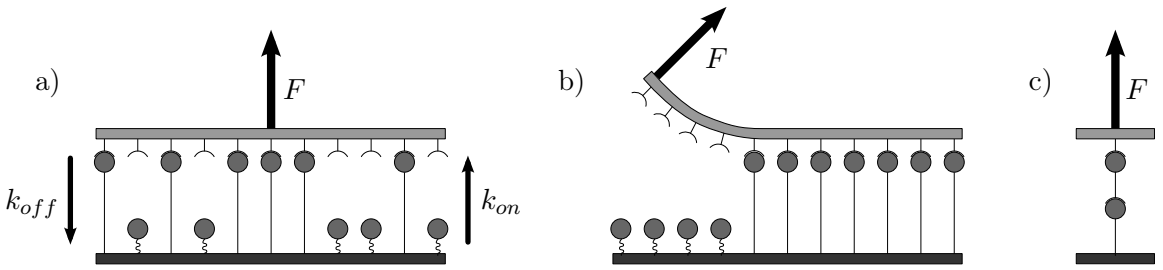

Figure 2.10: Schematic illustrations of three different adhesion clusters and their reaction on forces: a) parallel loading with a force F distributed over all closed bonds, k_{on} and k_{off} represent the closing and dissociation rate of the bonds; b) zipper configuration where the force F is breaking one bond after another; c) serial loading, all bonds experience the same force.

where k_0 is the rupture rate of a single bond (see equation 2.23), F is the applied force and $F_b = k_\mathrm{B}T/x_b$ is the internal force given by the thermal energy $k_\mathrm{B}T$ and the distance x_b between the potential minimum and the highest point of the potential barrier shown in Figure 2.9 [8, 33]. A typical value of F_b is in the single-digit piconewton regime (for $x_b \approx 1\,\mathrm{nm}$ and $T \approx 300\,\mathrm{K}$).

The behavior of single bonds only plays a role in short time or very specifically controlled and small environments. However, these single bonds are the building blocks of the (in nature much more frequently existing) multi-bond interactions, also described as clusters. A schematic overview of three possible organization of multi bond clusters and their reaction on applied forces is shown in Figure 2.10.

Theoretical models of focal adhesions assume that bonds are arranged parallel to each other as depicted in Figure 2.10 a and that forces exerted by actin fibers are homogeneously distributed

over the whole adhesion cluster [145]. This model postulates that bonds act like ideal springs and despite this simple model the maximum rupture forces can be very well estimated.

To get closer to the real biological system where bonds can form and break spontaneously under the influence of forces, more sophisticated models introduce the closing k_{on} and dissociation rate k_{off}. For the calculation of the rupture force F_r these on- and off- rates have to be taken into account as well as the so-called loading rate

$$r = \frac{\mathrm{d}F}{\mathrm{d}t} \tag{2.25}$$

being the temporal change of the applied force F. In most experiments this force is increased linearly over time so that $r = b \cdot t$ with $b =$ constant. This leads to a very complex function for the rupture force $F_r\left(r, k_{on}\left(r\right), k_{off}\left(r\right)\right)$ [146].

To describe the behavior of such an adhesion cluster under a constant force F, which is homogeneously distributed over all bonds, the disassociation rate k_{off} of a single bond in the cluster is described by equation 2.24 scaled by the number of closed bonds i. This leads to

$$k_{off} = k_0 e^{F/iF_b}. \tag{2.26}$$

Furthermore, the model introduces three dimensionless parameters: the number of binding pairs N_t, the total force $f = F/F_b$ and the rebinding rate $\gamma = k_{on}/k_{off}$ [30, 31]. To each time point $\tau = k_0 t$, i bonds are closed and $N_t - i$ are broken. The cluster is destabilized by the acting force and stabilized by the reformation of bonds. A stability analysis of this model shows that for a higher force than the critical force $F_c = f_c F_b$ with $f > f_c$ the bond rupturing is no longer balanced by the rebinding of open bonds. In the regime of $f < f_c$ two points of interest exist, an upper unstable one and a lower stable one. It is shown that in this small force case the cluster lifetime grows logarithmically with the number of bonds N_t for a weak rebinding rate ($\gamma < 1$) and grows exponentially for a strong rebinding rate ($\gamma > 1$). These findings underline the fact, that the reformation of bonds is a crucial mechanism to achieve typical biological cluster adhesion lifetimes. The special case of $f = f_c$ leads to a fusion of the two aforementioned points into a saddle-nod bifurcation. Under these conditions the, in most cases, exponential decay of the number of closed bonds i can dramatically rise by a small increase of the applied force. This effect could play a role in adhesion mechanosensing processes [143].

2.6 The Cytoskeleton and the Cellular Force Generation

In section 2.3 and subsection 2.5.1 the biological and biophysical basics of cell adhesions were discussed. As already pointed out in the aforementioned sections, one main role of focal adhe-

sions is the connection between the ECM and the actin cytoskeleton of the cell. Its three most important functions are the physical stability, regulation of the cell shape and the generation of forces for the cell motility or force transductions from its surrounding (e.g. the ECM) [38]. In the following two subsections the compounds of the cytoskeleton are briefly introduced and the main force generation processes in cells are outlined.

2.6.1 The Cytoskeleton

The central elements of the eukaryotic cell cytoskeleton can be subdivided into the following parts [1]:

- **Actin network:** This dynamic network consists of filamentous actin fibers (6 nm diameter) that are constantly polymerized and depolymerized from their globular monomer form to filamentous polymers and back, highly regulated by signaling mechanisms. Actin fibers can agglomerate to form actin bundles held together by proteins like α-actinin or filamin, cross-linked by fascin, branched by Arp2/3 and influenced by many other proteins [27]. One function of the actin network is to provide the scaffold for myosin V motor proteins to walk on them and transport cargo within the cell. Actin filament are polar which restricts the walking direction of motor proteins and allow a coordinated directed transport. Another feature is the formation of actomyosin complexes with myosin II, also called stress fibers. These complexes are able to generate forces acting intracellularly, to deform the cell shape, or extracellularly to exert forces through the focal adhesions to the ECM, either for cell motility or the deformation of the ECM. In the section 2.7 the properties of actin, its polymerization and possible myosin free force generation mechanisms are described in more detail.

- **Microtubules:** Two dimer monomers (α- and β-tubulin) polymerize to hollow cylinders (23 nm diameter), forming a network with a centromeric structure starting at the inner part of the cell (near the nucleus). Like actin filaments, also microtubules are dynamically polymerized and depolymerized but form a much less branched network. They do not form bundles and have a significantly higher rigidity than actin filaments (8 µm vs. 1.4 mm [161]). In eukaryotic cells microtubules provide the tracks for kinesin and dyneins motor proteins, which transport organelles within the cell. Similar to the actin filaments microtubules also show a polarity defining the possible walking directions of the motor proteins. Additionally, during mitosis mitotic spindles, consisting mainly of microtubules, are responsible for the chromosome separation.

- **Intermediate filaments:** Under this collective term several filaments are pooled together with a dimeter between the one of actin filaments and microtubules. All of them support the actin-network and microtubules in giving the cells their shape and holding

bigger parts like organelles at their position within the cytoplasm (e.g. vimentin and keratin). Furthermore, lamins support the nucleus and are also involved in the nucleus divison during mitosis. In contrast to actin filaments and microtubules the intermediate filaments are not polar.

2.6.2 Cellular Force Generation

The major force generation complexes in cells can be divided into two major branches: forces generated by the interplay between myosin II and actin filaments (c and d in Figure 2.11) and myosin free alternatives (a and b in Figure 2.11). Possible mechanisms behind the latter are further described in subsection 2.7.1.

One of the most prominent force generators in cells are the actin stress fibers. They consist of actin filaments held together by actin binding proteins (e.g. α-actinin) and contracted by myosin II motor filaments oriented parallel to the actin filaments [114]. Myosin II filaments are an agglomeration of myosin II monomers. Each monomer has a flexible head and tail domain the latter mediates the polymerization into myosin filaments. The "motor heads" are kinked at an angle of approximately 45-90° as to their tail domain depending on the state of the "power stroke"-cycle.

As for many biological processes this force generation also uses the energy stored in adenosine triphosphate (ATP) molecules. The transformation of this chemically stored energy into mechanical work is conducted by the myosin II motor proteins. Briefly summarized, the force generation cycle can be described in four steps [1]:

1. The myosin II head hydrolyzes an attached ATP molecule into ADP (adenosine diphosphate) and phosphate ion, without releasing the two molecules. This hydrolysis induces a bending of the myosin head, transforming the chemical energy into mechanical bending energy now stored in the molecular conformation of the myosin II.

2. The hydrolysis of the ADP at the myosin II increases the binding affinity of the head to actin, initializing a light binding of the head to the actin filament which triggers the release of the phosphate ion.

3. The release of the phosphate ion tightens the binding and initiates the so-called "power stroke", during which the bending energy and the ADP is released.

4. After releasing the whole stored bending energy, the myosin returns to its original rigor state, but is still coupled to the actin filament. The binding of a new ATP induces the detachment from the actin filament, bringing the cycle back to its beginning.

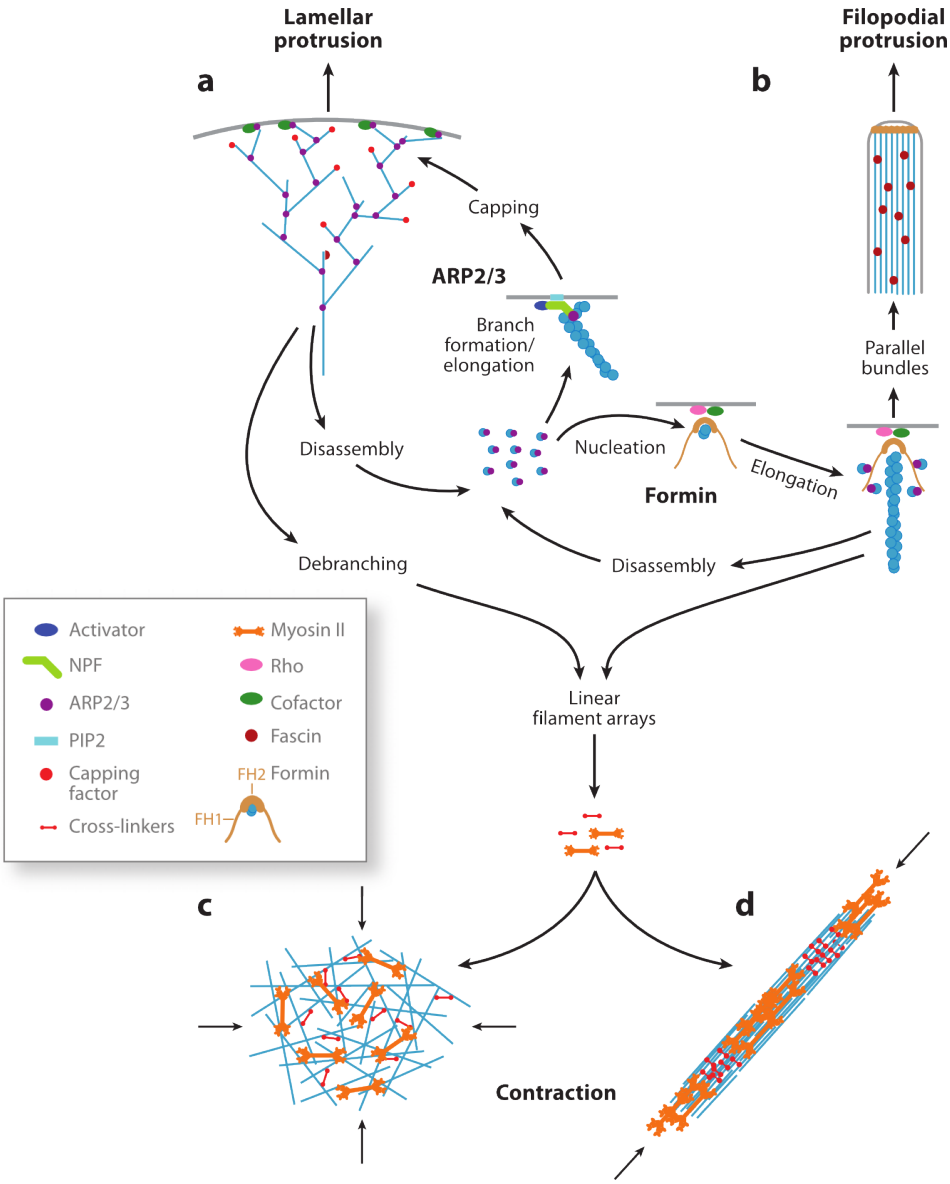

Figure 2.11: Illustration of the different actin assemblies and their role in force generation at different parts of the cell. a) Arp2/3 branched actin networks drive the advance of lamellar protrusions; b) filopodial protrusions are pushed forward by parallel bundles of actin fibers held together by fascin. In these two cases the force generation is mainly induced by the assembly and disassembly of the actin filaments. Linear actin filaments together with cross-linking proteins and myosin motor filaments can either form c) contractile 2D- or 3D-networks or d) stress fibers. Contractile networks can apply forces isotropically around them, while stress fibers generate linear forces. Abbreviations: Arp2/3, actin-related protein 2 and 3; FH, formin homology; NPF, nucleation-promoting factor; PIP2, phosphatidylinositol 4,5-bishosphate [76].

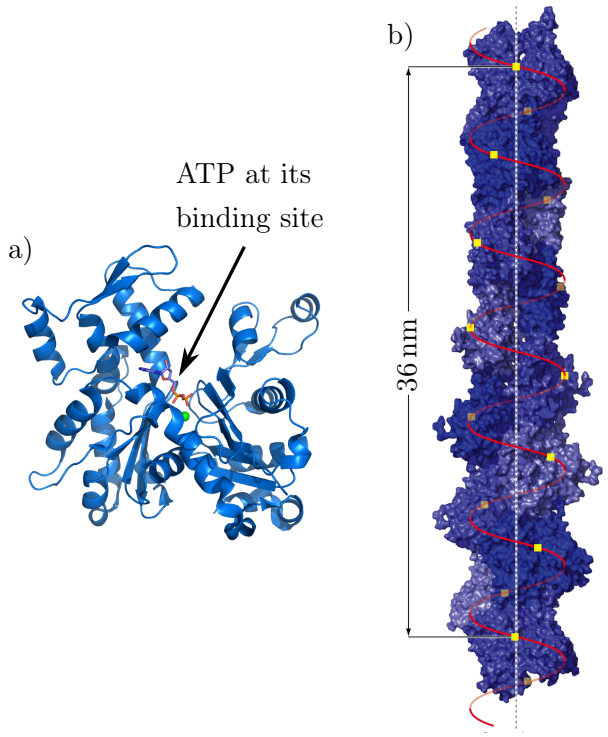

Figure 2.12: Atomic models of an actin monomer and filament. a) Structure of an actin monomer with an ATP molecule at its binding site. b) 13 actin monomers forming one rotation cycle of the helical structure of filamentous actin. This corresponds to a repeat length of 36 nm. Adapted from [26].

In general stress fibers can be split into three classes depending on their position and formation: ventral stress fibers, dorsal stress fibers and transverse arcs [150]. Ventral stress fibers are located along the bottom side of the cell and are connected to two focal adhesions at their ends. They represent the most common stress fibers. Dorsal stress fibers are only attached to one focal adhesion and bifurcate intracellularly to form the actin filament networks of the cytoskeleton [54]. Transversal arcs form behind and parallel to the edge of a protrusive lamella and are located under the upper membrane of a migrating cell [53]. Dorsal stress fibers can connect to these transversal arcs. The interplay of these different types of stress fibers are the main sources of cellular traction forces.

2.7 Actin

As shortly outlined in section 2.6 actin filaments are the polymerized form of globular actin (g-actin). These actin monomers are proteins of about 42 kDa, composed of 375 amino acids and prevalent in many living organism [65]. It is one of the most preserved proteins amongst these organisms, with only minor differences in the DNA sequences. The structure model of g-actin and filamentous actin (f-actin) can be seen in Figure 2.12. Polymerizing monomers connect to each other with a slight tilt leading to a helical f-actin polymer with a repeat length of 36 nm or 13 g-actin monomers. Actin monomers have an ATP-binding site in their middle

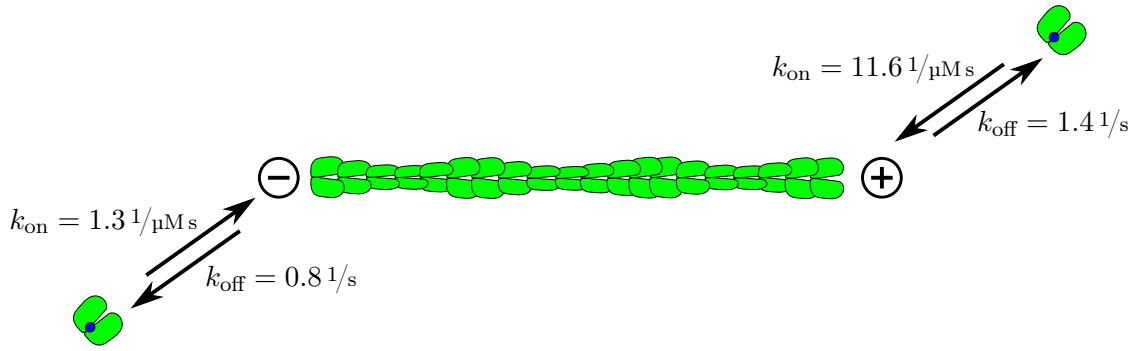

Figure 2.13: Polymerization of actin filaments in dependence of the monomer concentration. As can be seen by the on- and off-rates k_{on} and k_{off} rates, at concentration above $c_c^- = 0.62\,\mu M$, the filament is growing on both sides. For concentrations under $c_c^- = 0.62\,\mu M$, but above $c_c^+ = 0.12\,\mu M$, the filament grows on the plus-end faster than it is dissociating at its minus-end, leading to a "tredmilling" growth of the filament. At concentrations below $c_c^+ = 0.12\,\mu M$ the filament shrinks at both end. Adapted from [154].

that is usually occupied by a Mg^{2+} complexed ATP or ADP, both in its filamentous and its globular form. *In vivo* globular actins carry mostly ATP and filamentous actin ADP at their binding sites [85].

The polymerization process is induced, under physiological conditions, by increasing the g-actin concentration over the critical value of $c_c = 0.1\,\mu M$ [40] or by elevating the ionic strength in the solution [63, 153]. Three to four actin monomers form the starting filament which then, depending on the conditions, further polymerize or dissociate again. Since the actin monomers are asymmetric, the filaments are polar (called plus- and minus-end) with the two ends showing different polymerization kinetics [121]. T. Pollard showed the existence of three actin polymerizing regimes divided by two critical concentrations $c_c^+ = 0.12\,\mu M$ and $c_c^- = 0.62\,\mu M$. With a concentration lower than c_c^+, no elongation of the filaments is possible. At concentrations between c_c^+ and c_c^- the filament is growing at the plus-end but shortening at the minus-end, if both happens at the same rate (equilibrium) the length of the filament does not change, but monomers are passed through the filament from the plus- to the minus-end. This condition is also referred as "treadmilling". For concentrations above c_c^- the filament is growing at both ends, but significantly faster (about 10x) at the plus-end than at the minus-end [122].

Many parameters influence the actin polymerization kinetics, e.g. the fact if ATP or ADP is located at the binding site of the actin monomer, the ionic strength of the solution or the presence of actin binding or capping proteins like formins [32, 71, 123]. The above-mentioned critical concentrations c_c^+ and c_c^- were obtained with Mg^{2+} and ATP bound to the monomers. A polymerization can also take place without ATP but it accelerates the process significantly. Furthermore, proteins or drugs can have different effects on the polymerization and the physical properties of the actin filaments. Phalloidin, known as a toxin, for example, inhibits the depoly-

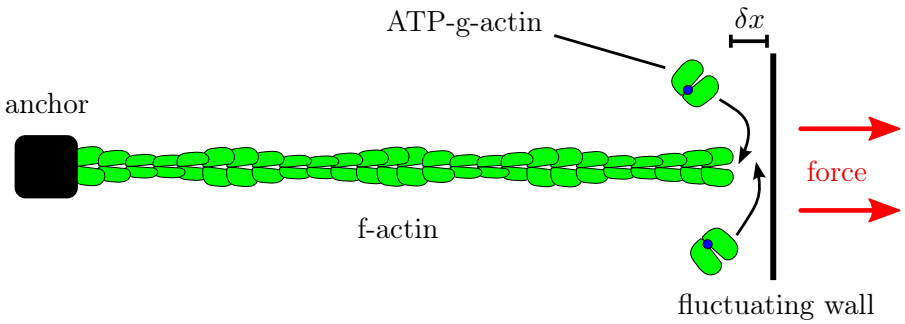

Figure 2.14: Schematic illustration showing the actin polymerization motor and its mode of operation. An actin filament is anchored at its minus-end pointing with the plus-end against a wall which is undergoing thermal fluctuations. If the fluctuation offers a gap δx between the end of the filament and the wall that is equal or bigger in size than one actin monomer, an actin monomer can bind to the filament end. This elongated actin filament blocks the wall from going back to its initial position and thereby pushing it forward. By repetition of this process a net force acts on the wall pushing it further to the right. Adapted from [154].

merization by a factor of about 30 [21, 34]. Additionally, these actin filaments are more rigid than actin filaments without phalloidin stabilization. The persistence length is approximately doubled from about 8 to 16 µm [9, 10, 16, 63, 84, 93, 110]. For the actin experiments we exploit this effect in two ways, first the actin filaments are considerably longer than without phalloidin and second a fluorescent marker at the phalloidin molecule allows the visualization of the actin by fluorescence microscopy.

2.7.1 Myosin-independent Actin Force Generation

The highest forces in cells are produced by the cooperation of actin and myosin II, but as illustrated in Figure 2.11 not all force generation processes involve myosin. Two of the most known examples are the formations of lamellar or filopodial protrusions neither involve myosin II nor the dissociation of ATP [122]. To describe the possible physical mechanisms driving these two models have been commonly consulted: the polymerization motor and forces generated by bundle formation.

Based on the "Brownian ratchet" thought experiments of M. Smoluchowsky 1912 and R. Feynman 1962 the polymerization motor model was developed as possible driving force of filopodial protrusions [118]. The basic model of its operation is the following. An actin filament is fixed at its slower growing minus-end and in front of the plus-end a flexible obstacle under Brownian motion (e.g. the cell membrane) is hindering the growth of the actin filament. Since the obstacle is fluctuating, the gap between obstacle and the actin filament plus-end can be large enough to allow the binding of a further actin monomer and thus to an elongation of the filament. This monomer inhibits the return of the obstacle to its original position and by reiterating this process the obstacle is pushed further forward. This way, the polymerization of the actin filament

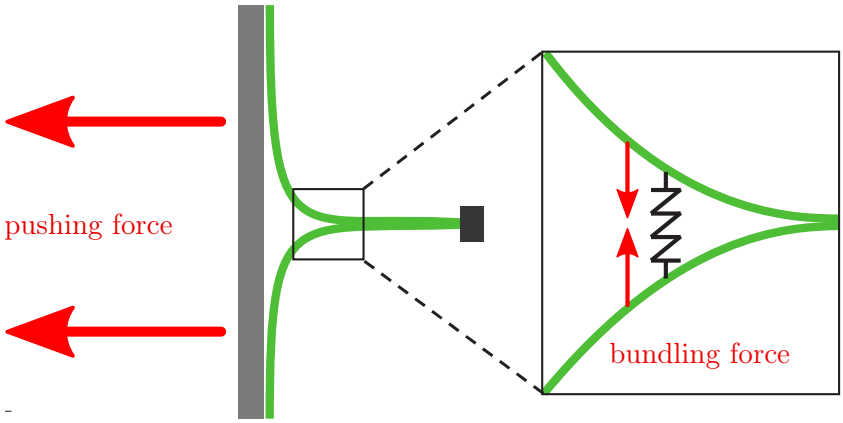

Figure 2.15: Force generated by the bundling of two actin filaments. Both actin filaments (green) are anchored on one side and bent in opposite directions an rest friction free against a wall. Bundling of the filaments induced by an attractive interaction and indicated by the spring (right) pulls the filaments together and thereby bends the filaments further. Due to the semiflexibility of the actin the bent filaments exert part of the bending forces towards the wall and thereby pushing it to the left. Adapted from [154].

is exerting a force on the obstacle and performing work. Different theoretical approaches on this topic, which either use this basic model or a model with even more parameters, like the filament rigidity [97] are able to calculate the maximum force of this polymerization motor of a single actin filament to 0.8 pN. This theoretical value was experimentally confirmed by Footer et al. [35]. They placed a microsphere trapped with an optical tweezer in front of a wall. On the microsphere an acrosomal actin bundle was attached and grown towards the wall. The actin bundle thereby pushed against the microsphere in the optical trap which allowed, for known trap stiffness and deflection, the calculation of the acting force. Their evaluations revealed a polymerization force of 0.76 ± 0.22 pN per actin filament. This model could describe the force generation processes in a cellular filopodium consisting of tightly bundled parallel actin fibers (see Figure 2.11 b).

In filopodia actin filaments are held together by fascin a protein of 55 kDa leading to a spacing of just 12 nm between the bundled actin filaments. The bundling of actin filaments is also suggested to contribute to the force generation with the so-called "zipping" forces. This process could be involved in the initial formation of filopodial protrusions [73, 98, 163].

For the generation of these "zipping" forces the simplest model consists of two actin filaments bundled at one end, and their other ends bent in opposite directions (see Figure 2.15). At the bundled end the fibers are fixed, while on the split end a wall is hindering the bundling of the filaments. This bundling could be initiated by many agents like actin binding proteins [95], depletion forces or divalent ions [2]. These bundling agents induce the attractive interaction between the filaments causing the movement of the "zipping point" towards the wall and thereby

bending the two filaments. Since actin filaments are semiflexible, the bending causes a force acting against the wall, thus pushing it away from the "zipping point".

An experimental approach by M. Streichfuss et al. investigated the dependence of these bundling forces induced by divalent ions as a function of the ion density [155]. They determined the maximum possible force generated by this configuration to approximately 0.2 pN per filament pair.

2.7.2 Actin Bundling by Divalent Ions

Actin filaments carry eleven negative charges per monomer resulting in a natural repulsion between them. For the formation of bundles not only this repulsion has to be overcome, but also an attractive force must be introduced.

A theoretical concept of the effects of counterions on like charged polymer strings has been described by G. S. Manning 1978 [90]. The repulsion for like charged polymers was found to be reduced by

$$\theta = 1 - \frac{1}{N\frac{\lambda_B}{b}} \tag{2.27}$$

with N being the valency of the ions, λ_B the Bjerrum length (see below) and b the linear charge spacing along the polymer. The Bjerrum length λ_B is given by

$$\lambda_B = \frac{e^2}{4\pi\epsilon_0\epsilon k_B T} \tag{2.28}$$

with e being the elementary charge and ϵ the dielectric constant. This Bjerrum length is defined as the distance between two elementary charges having an interaction energy equal to the thermal energy $k_B T$. In water at 20 °C ($\epsilon = 80$) the Bjerrum length λ_B is 7.1 Å. By using the fact of eleven negative charges per actin monomer the linear charge spacing b of an actin filament can be calculated to about 2.5 Å. Together with the Bjerrum length λ_B of water the shielding effect of an ion solution on actin filaments can be calculated for monovalent ions ($N = 1$) to 65 % and for divalent ions ($N = 2$) to 82 % of shielded charges. This effect describes a significant decrease of the repulsion between two actin filaments, but even in the case of divalent ions, the repulsion is only lowered but not compensated or even overcompensated as it would be needed to explain the attractive interaction.

Different theoretical models try to resolve the physical interactions causing this filament bundling by counterions, but so far no explanation is totally convincing. One model describes the interactions between two identical rodlike polygons carrying equidistant monovalent charges. Like actin filaments these polyions would normally repel each other. But in a counterion solution, and in the case that the distance between the polyions is smaller than the Debye length, an attractive interaction appears. This model explains this effect by an overlapping

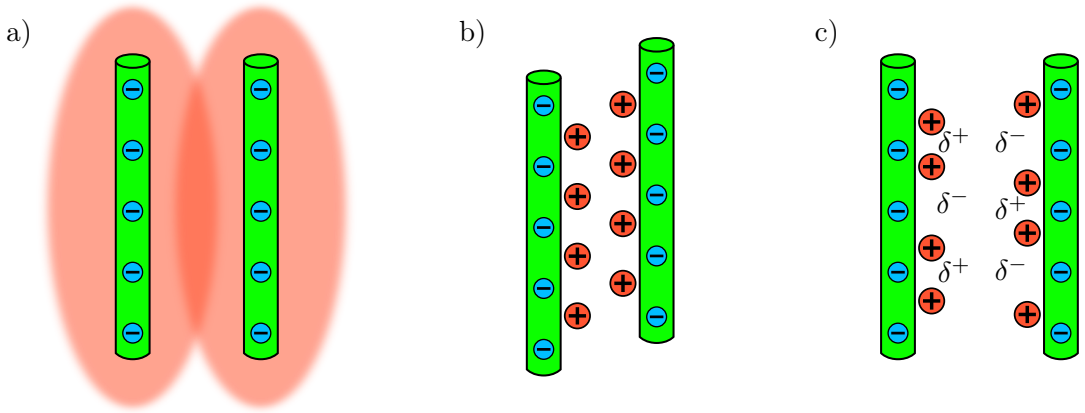

Figure 2.16: These schemes illustrate the three assumed possible causes of the attractive interaction of two identical charged rods. a) If the two rods or filaments come close enough together, the counterion regions (red) around the rods overlap, so counterions are shared between them. b) Based on the electronic repulsion acting among the positively charged counterions, they form periodic agglomerations of ions along the rod. By shifting the second rod one half of the periodicity length their "toothed" periodic structures lead to a mineralization of the repulsion. c) Under the assumption that the counterion agglomerations can fluctuate along the rod, positive and negative local charges generate a van der Waals like attractive interaction. Adapted from [154].

of counterion accumulations allowing the two polyions to share the counterions leading to an amplified translation entropy and thus to and attractive interaction [126].

Another model explains the attractive interaction between two charged rods with equidistant charges and mobile counterions by using Brownian-dynamics simulations [49]. According to this model the counterions on the two rods form toothed or zipper like configurations (see Figure 2.16 c), at low temperatures. This configuration then leads to an attractive force persistent even at higher temperatures.

Other models are based on the same initial situation as the afore mentioned example but go a step further by taking the possibility of fluctuations into account [75, 109]. Comparable to the van der Waals interaction fluctuations of the counterion agglomerations, induced by thermal motion, cause the formation of electrical dipoles. The interaction between these dipoles could then result in an attractive force between the filaments.

All previously discussed models for the explanation of the bundle formation of actin filaments did not take the special form of the actin monomers and its filamentous configuration into account. Exactly these shortcomings are removed by the model of Yu et al. [172]. One result of this model was the calculated threshold for the attractive interaction between two actin filaments, being at an ion concentration of 10 mM. Experimentally, clues for bundling at even lower concentrations of approximately 5 mM were observed [132].

How these bundling processes by divalent ions play a role in the *in vitro* bundling process

is a matter of discussion, since the physiological ion concentration is significantly lower than the calculated 10 mM or observed 5 mM [1]. One possibility is a local accumulation of ions increasing the concentration and thus induce the bundling.

Chapter 3

Materials and Methods

In this chapter the required instruments as well as materials and methods necessary for the execution of the presented experiments, their preparation and evaluation are introduced and described. This includes standard techniques like: the microscopy systems used, block copolymer micelle nano lithography (BCML), silanization of glass surfaces, actin purification and handling, soft lithography and cell culture, fixing and immunofluorescence staining procedures. Furthermore, the fabrication of PEG pillars functionalized with gold nanoparticles (GPPPs) or surface coated microbeads is outlined, followed by the description of their calibration process. At the end, a short overview of the software used for pillar tracking, data evaluation and the thereby achieved tracking accuracy is provided.

3.1 Microscopy Systems

Four microscopy types were used for the performed experiments, the examination and observations of micron- and submicron-sized objects, namely: confocal-, brightfield-, fluorescence- and scanning electron microscopy (SEM). Furthermore, the GPPP illumination process outlined in subsection 3.8.1 was executed on a fluorescence microscope. The microscopes used throughout this thesis were the following:

- **Optical microscopes:**
  - **Zeiss Pascal 5 Laser Scanning Microscope (LSM):** This microscope offers a fluorescence and a confocal operation mode. The fluorescence settings were exploited for the illumination process of the GPPPs described in subsection 3.8.1. Its software controlled motor stage and shutter allowed a semi-automated illumination process. Confocal images of actin networks formed on the bead functionalized PEG pillars were recorded and are shown in section 4.2.

  - **Zeiss Axio Observer:** A standard fluorescence microscope with motorized stage and incubation chamber for life cell experiments. Time lapse recordings of life rat embryonic fibroblasts (REF) on the GPPPs functionalized with the two integrin selective ligands were acquired on this microscope (see subsection 3.6.2). Additionally, the fluorescence images of fixed and stained cells were also taken on this machine.
  - **Zeiss Axiovert 200 with PI-piezo stage and cantilever micromanipulator:** Based on a Zeiss Axiovert 200, this microscope was modified by the addition of a high precision piezoelectric driven stage[1] and a custom built atomic force microscopy (AFM) cantilever micromanipulator. This setup provided the experimental requirements for the calibration process of the GPPP spring constants described in section 3.5.

- **Scanning electron microscope:**
  - **Field Emission Scanning Electron Microscope LEO 1530 VP:** This SEM was used to image the gold nano particle structures produced by BCML and to control the transfer of the gold nanoparticles to the GPPPs.

3.2 Block Copolymer Micelle Nanolithography Structures and their Transfer to Poly(ethylene glycol) Hydrogels

In oder to construct (quasi) hexagonal gold nanoparticle patterns on the top of the PEG pillars, these patterns were first self-assembled on glass coverslips using the diblock copolymer micellar nanolihography (BCML) method. This method is based on polymer solutions containing micelles loaded with gold nanoparticle cores surrounded by diblock copolymer shells produced and stored in toluene. A whole variety of different possible polymer lengths control the thickness of the shell and with it the final interparticle spacing. By dipping the glass surfaces in the micelle solution or spin coating it on the glass surfaces, the micelles form a quasi hexagonal two dimensional pattern. Afterwards, plasma treatment removes the polymer shell leaving only the gold nanoparticles on the glass surface (see Figure 3.1). The precise procedure can be found in [86] or many theses of the Spatz group, e.g. [87, 116, 144]. Under optimal conditions spacing down to 30 nm with particle sizes of 5 nm are possible. As first utilized by S. V. Graeter et al. in [47] and described by T. Lohmüller et al. [86] the transfer of the gold nanoparticles to PEG hydrogels of varying stiffnesses is well established and can be achieved by the application of N,N'-bis(acryloyl)cystamine as a linker molecule.

To enable the coupling of the linker to the gold nanoparticles, the surfaces were activated in oxygen plasma[2] (10 min, 150 W, 0.4 mbar), incubated for one hour in an N,N'-bis(acryloyl)-

[1] P-541.2SL, PI, Germany
[2] TePla 100-E radio frequency plasma generator

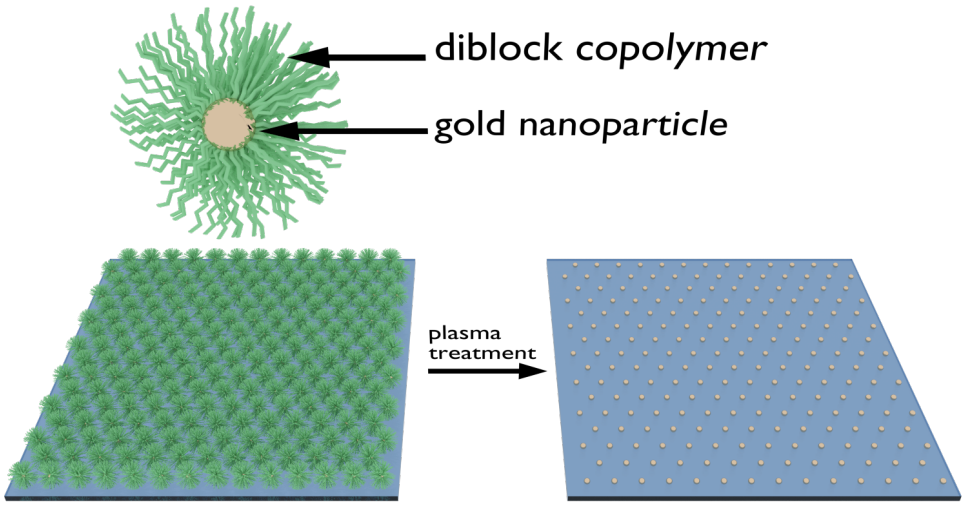

Figure 3.1: The gold nanoparticle diblock copolymer micelles self assemble to (quasi) hexagonal monolayers on the substrates deposited via dip or spin coating. After formation of the structure defined by the polymer length and the dipping or spinning speed, the polymer is removed by a 45 min hydrogen plasma treatment leaving only the gold nanoparticles on the substrate.

cystamine[3] solution ($c = 2\,^{mmol}/_{l}$) in ethanol[4] (pa), rinsed in pure ethanol three times for 15 min and kept under ethanol until usage. The N,N'-bis(acryloyl)cystamine is divided symmetrically at its sulfur-sulfur bond, due to the high affinity of the sulfur group to gold. The linkers attached to the gold nanoparticles also present a carbon-carbon double bond, to which the polymerizing poly(ethylene glycol) diacrylate (PEG-DA) (see Figure 3.5) can bind covalently, thus the N,N'-bis(acryloyl)cystamine acts as a linker between the PEG and the gold particles (see Figure 3.2).

For the presented cell experiments, gold nanoparticle spacing of 55 ± 5 nm were used. These distances are known to provide an appropriate ligand spacing to stimulate the adhesion of rat embryonic fibroblasts (REF) on glass surfaces [15].

3.3 Surface Silanization via Self Assembled Monolayer

The base glass coverslip for the GPPP fabrication was silanized to provide a covalent binding site to the poly(ethylene glycol) diacrylate (PEG-DA) during polymerization. Therefore, a monolayer of allyl-triethoxysilane was applied on the glass surface of the coverslip. Self assembly

[3] Fluka, Switzerland
[4] Roth, Germany

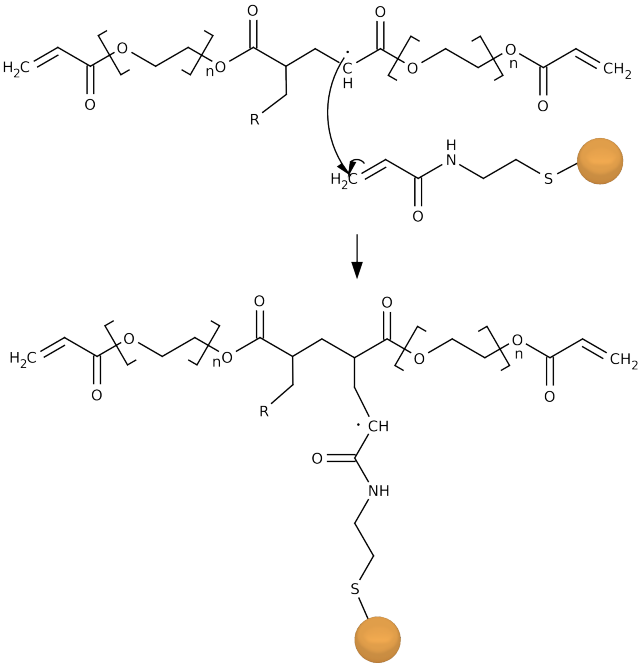

Figure 3.2: One half of the N,N'-bis(acryloyl)cystamine binds to the gold nanoparticle and presents a carbon-carbon double bond. This double bond is opened by a polymerized PEG-DA radical (see also Figure 3.5) resulting in covalent binding of the PEG to the gold nanoparticle. Additionally, the reaction leads to a radical that can further react with PEG-DA molecules or other PEG-DA radicals.

of molecular monolayers is a common process used to modify the surface properties or reactivity of silicon oxide based substrates like glass or quartz [91].

For the preparation the glass coverslips[5] (24 x 50 mm) were cleaned for 15 min in an ultrasonic bath containing a 30 % aqueous extran solution[6], followed by two 15 min washing steps with Milli-Q water[7] and sonication. Afterwards, the glass slides were dried at 65 °C. To enhance the reactivity of the surface, the coverslips were exposed to an oxygen plasma[8] (10 min, 150 W, 0.4 mbar). This led to readily available free hydroxyl groups for the silane to couple to. After the plasma activation the coverslips were placed in a desiccator with a petri dish containing 100 µl of allyl-triethoxysilane[9]. Then the desiccator was evacuated over the boiling pressure of the silane (approx. 1 min) and the coverslips were left within the silane atmosphere for at least two hours. The allyl-triethoxysilane reacted with the hydroxyl groups offered by the activated glass surface via nucleophilic substitution (see Figure 3.3). It bound covalently to it and formed a monolayer presenting a carbon-carbon double bond on the surface. To this presented double bond PEG-DA could covalently bind during the radical polymerization induced by the illumination process described in subsection 3.4.1. The silanized coverslips were then stored at room temperature and used within two weeks.

[5] Roth, Germany
[6] Merck KgaA, Germany
[7] Millipore, USA
[8] TePla 100-E radio frequency plasma generator
[9] Sigma-Aldrich, USA

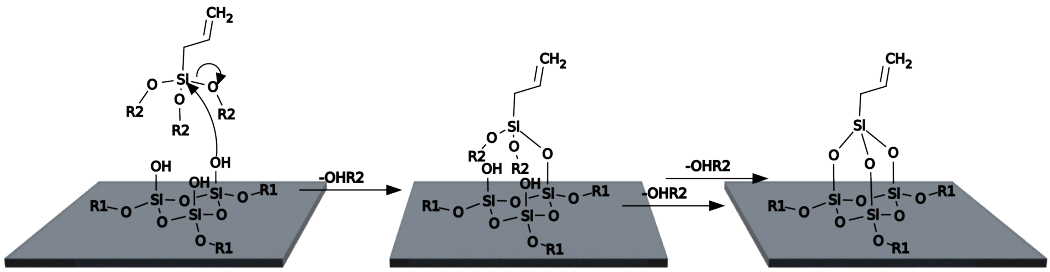

Figure 3.3: Schematic illustration of the glass coverslip silanization process with allyl-triethoxysilane ($R2 = C_2H_5$). The oxygen plasma activated glass surface presents hydroxyl groups on the surface ($R1 = x \cdot SiO_2$). By nucleophilic substitution the silane binds covalently to the silicon dioxide and offers a carbon-carbon double bond. This reaction takes place on the whole glass surface leading to a monolayer of allyl-triethoxysilane. The polymerizing PEG-DA radicals generated by the polymerization process shown in Figure 3.5 break one bond of the carbon-carbon double bond and bind covalently to the surface similar to the reaction of the gold nanoparticle linker to the PEG radicals shown in Figure 3.2.

3.4 Fabrication of Functionalized Poly(ethylene glycol) Micropillars

Inspired by the microscope projection photolithography introduced by Love et al. [88] and the work of Revzin et al. [129] B. Rühle and A. Lindner established a simple and fast and direct way to produce PEG pillars. They achieved pillar geometries of approximately 7 µm diameter, 30 µm spacing and a aspect ratio of 1 : 10. Their functionalization method was based on the immobilization of microbeads with the desired functionalization on the PEG pillar tops. This straightforward method was used to create highly sensitive PEG pillars (spring constants $\approx 0.5\,{}^{\mathrm{nN}}/_{\mu\mathrm{m}}$) for the investigation of the contractile forces of bundling actin networks (see section 4.2).

The fabrication of the GPPPs was realized by combining the PEG pillar construction and the transfer of gold nanoparticle structures. These gold nanoparticle structures were received by block copolymer micelle lithography (BCML) and transferred to poly(ethylene glycol) diacrylate (PEG-DA) surfaces, briefly described in section 3.2. Functionalization of the gold nanoparticles can be achieved by binding thiolated chemical or biologically active compounds to them. For the presented studies two integrin selective peptidomimetics were used (see section 2.4) to analyze their impact on cellular adhesion and force generation (see section 4.1).

The following sections describe the fabrication methods of these two different types of PEG pillars, which share most of the production steps and differ only in the composition of the "sample sandwich". Their upper coverslip was either covered by gold nanoparticles or a monolayer of surface coated microbeads, illustrated in Figure 3.4 and Figure 3.7.

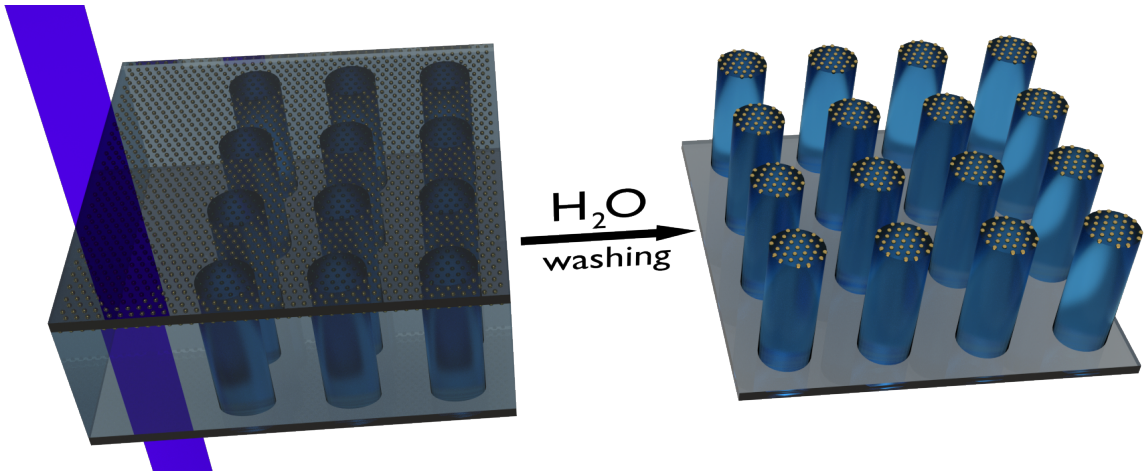

Figure 3.4: Schematic illustration of the "sample sandwich" consisting of a gold nanoparticle structured coverslip with attached linker on top (see Figure 3.2), a silanized coverslip at the bottom and a fluid PEG pre-polymer solution in between (left). This sample is illuminated by a collimated UV-light ray ($\lambda = 360\,\text{nm}$) leading to polymerization of the PEG pre-polymer at the illuminated position. During the polymerization of the PEG it simultaneously binds covalently to the silanized bottom coverslip and to the linker bound to the gold nanoparticles on the top end. After dissolving the unpolymerized PEG and removing the upper coverslip the GPPPs are left on the bottom coverslip (right).

3.4.1 Gold Nanoparticle Poly(ethylene glycol) Micropillar Microscope Photolithography

To fabricate the PEG micropillars, used in the presented experiments, a pre-polymer solution containing 1 ml poly(ethylene glycol) diacrylate (PEG-DA, n = 700 or 400)[10] and 5 mg 2-hydroxy-4'-(2-hydroxyethoxy)-2-methylpropiophenone[11] as photo initiator was prepared in an argon atmosphere and used immediately after preparation.

To fabricate GPPPs, a layering approach was used (see Figure 3.4). In this regard, the following components were stacked in a sandwich-like structure: (i) an allyl-triethoxysilane-silanized glass slide as base (see section 3.3), (ii) 3-15 µl of the pre-polymer PEG solution (the volume depending on the desired length of the pillars to be constructed on the glass slide), and (iii) a coverslip with the gold nanoparticle pattern obtained by BCML and functionalized with the diacrylate linker on top (see section 3.2). This arrangement was then placed on the specimen platform of the LSM Pascal 5 microscope. The samples were illuminated by UV light ($\lambda = 360\,\text{nm}$) through the DAPI-filter of the fluorescence pathway using a 100 W HBO mercury lamp[12] light source and a 40x/1.2 water objective (440052)[12]. As an illumination

[10] Polysciences, USA
[11] Irgacure 2959, HHEMPP, Sigma-Aldrich, USA
[12] Zeiss, Germany

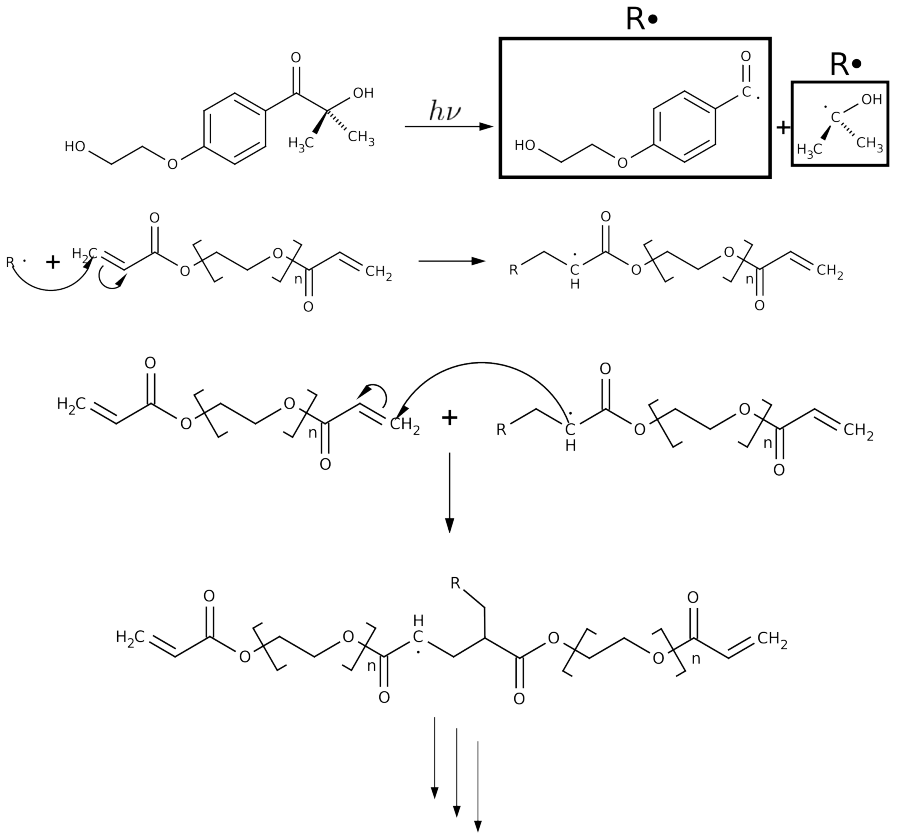

Figure 3.5: Illustration of the PEG-DA polymerisation process. The photo activated initiator is homolytically cleaved into two radicals ($R\cdot$) by UV light (360 nm). Each of this radicals can react with a PEG-DA molecule leading to a new (PEG) radical, which then can couple to the next PEG-DA molecule and so forth, resulting in a PEG network structure.

mask, a 100 µm pinhole[13] was placed at the field-stop position within the fluorescence light path. Platform position and shutter control offered an illuminated spot accuracy of $\Delta t = 0.1\,\mathrm{s}$ and $\Delta x = 1\,\mu\mathrm{m}$, respectively. The platform position and shutter control was operated by a self-written *.net* program (by B. Rühle [135]).

Polymerization is initiated by UV light ($\lambda = 360\,\mathrm{nm}$) illumination, cleaving the photo initiator homolytically into two radicals. Each of these radicals can react with the PEG-DAs double bond at one of its acrylate groups resulting in the formation of a new carbon-carbon bond and a new (PEG) radical that can react with the next PEG-DA molecule. Due to the fact, that the PEG-DA has two functional groups it consequently forms a 3D network structure. At the silanized glass surface (see section 3.3) the PEG radicals reacted with the presented carbon-

[13] Owis, Germany

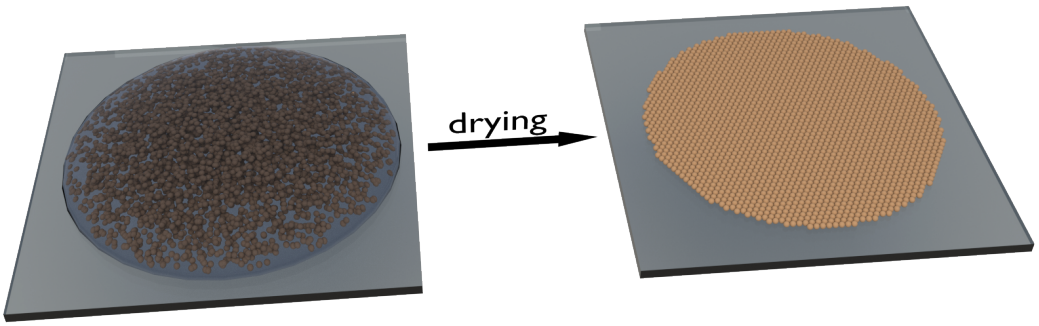

Figure 3.6: A drop of diluted functionalized bead stock solution is placed on an extran cleaned coverslip and dried. Gravity and the evaporating liquid lead to the formation of a monolayer of beads. This image shows the ideal case, where a perfect monolayer is formed.

carbon double bonds on the glass surface and of the N,N'-bis(acryloyl)cystamine linker bound to the gold nanoparticles (see Figure 3.2), leading to a covalent connection to the glass surface on the one side and to the gold nanoparticles on the other.

After the illumination process the complete "sandwich" was put in a petri dish filled with Milli-Q water. The non-polymerized PEG dissolved in the water and after removing the upper coverslip carefully, the gold nanoparticle structured PEG pillar fields remained on the silanized bottom coverslip. For storage the GPPPs were transferred into a petri dish with sterile water and stored at 4 ℃ and used within 4 weeks.

The standard GPPP arrays for the cell studies were made out of PEG-700, each pillar had a diameter of 3.5 ± 0.5 µm a length of 13 ± 1µm and a spring constant of 15 ± 2 $^{\mathrm{nN}}/_{\mu\mathrm{m}}$. With these properties of the single pillars, pillar fields of $50\,\mathrm{x}\,(a \cdot 50)$ pillars $(1 < a < 10)$ with a center to center spacing of 8 ± 1 µm were produced. Initially, big quadratic pillar fields ($200\,\mathrm{x}\,200$ and more) were illuminated, but they had the issue that if the fabrication process was disturbed (e.g. focus or stage drift) it had a much bigger impact on the homogeneity of the pillar field than in the $50\,\mathrm{x}\,(a \cdot 50)$ illumination process. If, in the latter case, an error occurred only a few lines with unusable pillars were illuminated until the error was corrected. These areas were than simply neglected in the time lapse experiments.

3.4.2 Microbeads Functionalized PEG Pillars

The second functionalization method for the PEG micropillars was realized by embedding surface coated microbeads (e.g. streptavidin coated polystyrene beads) on top of the pillars. These bead functionalized PEG micropillars were used for the contractility studies of actin networks (see section 4.2).

The fabrication of these pillars was identical to the GPPP production described in the subsec-

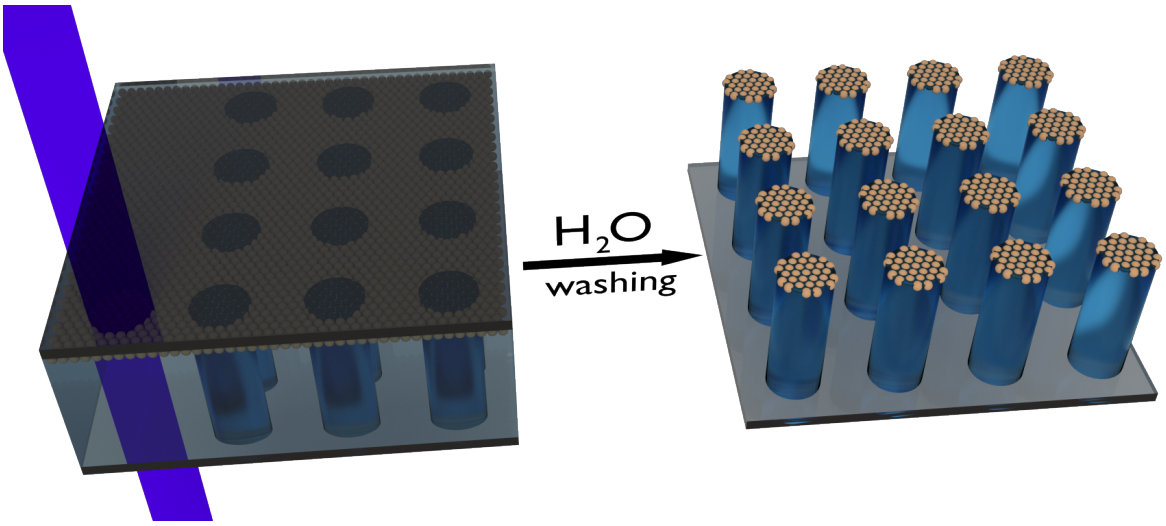

Figure 3.7: The figure shows schematically the illumination process of the bead functionalized PEG pillar. This method is basically the same shown and described in Figure 3.4, however, the upper coverslip on the left side was covered by a monolayer of functionalized micro beads obtained by drying a drop of bead solution on a coverslip (see Figure 3.6) instead of a gold nanoparticle structure.

tion 3.4.1, however, the gold nanoparticle structured coverslip on top of the "sample sandwich" (see Figure 3.4) was replaced by a coverslip covered with a monolayer of functionalized microbeads. This upper coverslip was produced by drying a bead solution on it. A carefully chosen bead density allowed the formation of a bead monolayer on the coverslip.

For the performed actin experiments streptavidin coated micro beads[14] with a diameter of 1,84 µm were used. Before drying on a coverslip the stock bead solution was diluted in a ratio of 1 : 10 in Milli-Q water. A drop of 300 µl of this solution was placed on an extran cleaned 24 x 24 mm coverslip (see subsection 3.4.1) and dried at room temperature. Under ideal evaporation conditions this would lead to a perfect monolayer of beads as shown in Figure 3.6. Since this ideal conditions are never met there were always areas with double or even multilayers of beads. Due to the fact, that the area covered by the bead layer was much larger (about 1 cm^2) than the resulting pillar arrays (up to 3 mm^2) the monolayer regions were chosen for the illumination process as described in subsection 3.4.1. These bead functionalized pillars were then stored in a sterile phosphate buffered saline (PBS) solution[15] at 4°C for up to 4 weeks.

[14] Kisker-Biotech, Germany
[15] PAA, Austria

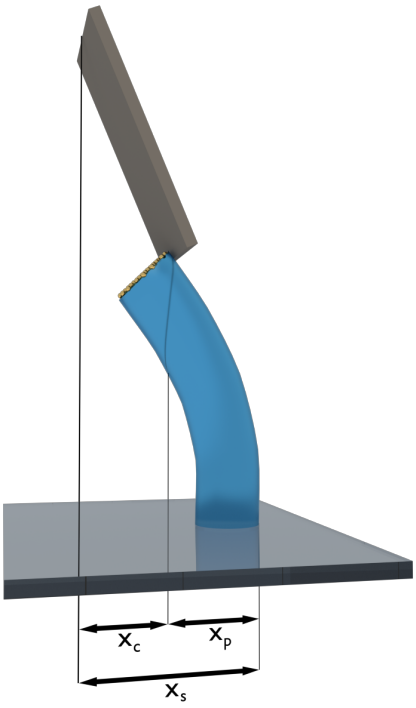

Figure 3.8: This illustration shows schematically the calibration process of a PEG micro pillar. The AFM cantilever (grey box on top) is fixed and a PEG pillar is moved with a constant velocity against it, leading to a bending of both parts. The values needed for the derivation of the equation 3.10 used for the calculation of the spring constant are the deflections of the cantilever x_c, the pillar x_p and the distance the stage moved x_s since the contact of cantilever and pillar.

3.5 Calibration of the PEG Pillars

Due to the many parameters (e.g. the burning time of the HBO lamp, exact opening of the aperture, age of the PEG and initiator) influencing the Young's modulus and thus the spring constant of the PEG pillars they had to be calibrated. To do so, either the involved pillars were calibrated directly or a calibration pillar field was created right beside the force mapping pillar field, assuming that they exhibit the same spring constants. A direct calibration of the pillars was only possible for the hexagonal pillar "islands" used for the contractile actin network experiments (see subsection 4.2.2). The calibration pillars had a center to center spacing of 40 µm and the same illumination conditions (pinhole, illumination time, aperture opening) as for the force mapping pillar fields were applied. The calibration pillar fields were necessary to allow the 32.5 µm wide cantilever tip to approach and bend only single pillars. That was not possible for the standard cell experiment GPPP array spacing of 8 µm.

The spring constant of the micropillars was determined using an atomic force microscopy (AFM) cantilever[16] as a reference. Prior to the PEG pillar calibration, the cantilever spring constant was measured using the built in tools of a JPK NanoWizard I[17]. To calibrate the micropillars, the AFM cantilever was vertically fixed in a custom made micromanipulator such

[16] CSC38 no AI µmasch, Switzerland
[17] JPK Instruments AG, Germany

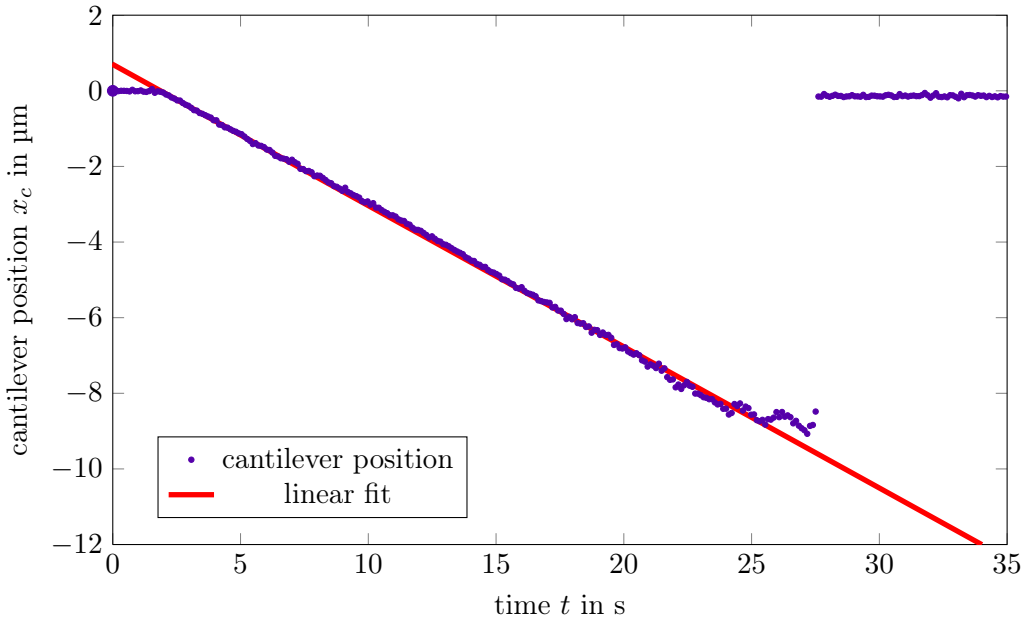

Figure 3.9: This graph presents a typical calibration curve. It shows the deflection of the AFM cantilever over time. The cantilever was bent by the PEG pillar moving with a constant velocity against it. Up until approximately 3 s there was no contact between pillar an cantilever (no deflection) then they get in contact and are both bent (linear bending part). At approximately 27 s they lost contact and the cantilever snapped back to its initial position. The linear relation is clearly visible and expected for small deflections ($< 5\,°$) described by the Euler-Bernoulli beam theory discussed in subsection 2.1.1. For the calculation of the spring constant by equation 3.10 the slope m was determined by a linear fit to the initial bending part of the calibration curve.

that its tip was situated approximately 1 - 4 µm (Δl, estimated by equation 3.12 and illustrated in Figure 3.11) below the top of the PEG pillar. For the controlled movement and observation the piezo stage[18] equipped Axiovert 200 microscope[19] and the 60xW/1.1 objective[20] were used. By moving the pillar via the piezo stage at a predefined constant velocity towards the cantilever they collided and both, cantilever and pillar, were bent. This procedure was monitored with an ORCA camera[21] at a fixed frame rate. The position of the cantilever in the acquired images was determined using the ICARUS [45] video tracking software. With knowledge of the cantilever spring constant, the movement speed of the stage and the frame rate of the camera the spring constant of the pillar could be calculated. This was achieved by determining the slope of the bending part of the cantilever tracking curve (see Figure 3.9).

[18] P-541.2SL, PI, Germany
[19] Zeiss, Germany
[20] LUMFLN 60xW, Olympus, Japan
[21] Hamamatsu, Japan

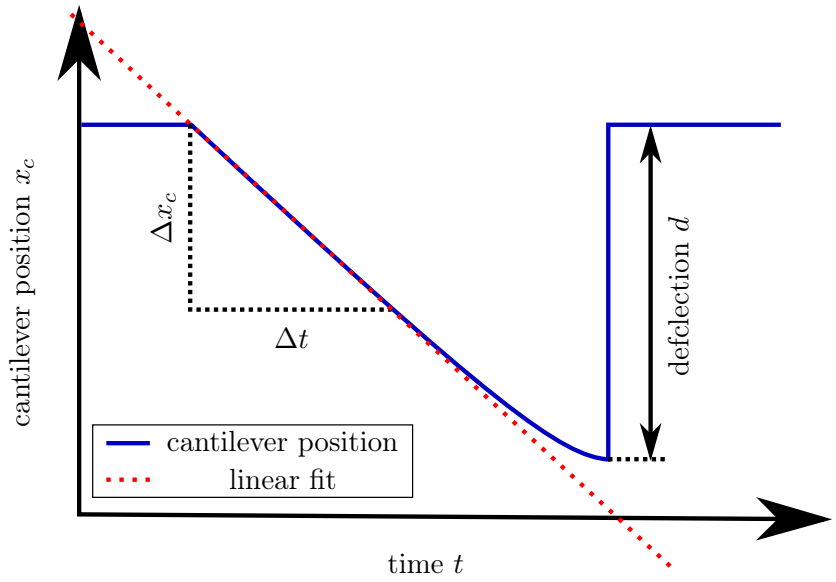

Figure 3.10: Schematic evolution of a actual calibration curve (Figure 3.9) is depicted. The relevant entities for the derivation of the pillar spring constant equation 3.10 are Δx_c, which is the deflection of the cantilever in the time frame Δt, and the slope m of the bending part of the curve (red dashed line). Additionally, the full deflection d of the cantilever at the point where the cantilever and pillar loose contact is plotted.

Mathematically the slope of the bending part is described by

$$m = \frac{\Delta x_c}{\Delta t} \tag{3.1}$$

with Δx_c being the cantilever deflection in the time frame Δt (see Figure 3.10). Figure 3.8 shows that

$$x_s = x_c + x_p \tag{3.2}$$

with x_s being the way the stage moved since the contact of the cantilever and the pillar consisting of the overall cantilever deflection x_c and the overall pillar deflection x_p at the time t. Within a time frame Δt the stage moves the way

$$\Delta x_s = \Delta x_c + \Delta x_p \,. \tag{3.3}$$

Due to the constant velocity v of the stage movement the distance the stage moved at the time t is $x_s = vt$ or for the time frame Δt it is $\Delta x_s = v\Delta t$. With that equation 3.3 can be converted to

$$\Delta t = \frac{\Delta x_c + \Delta x_p}{v} \,. \tag{3.4}$$

This equation can be inserted into the expression 3.1 which leading to

$$\frac{\Delta x_c}{\Delta x_p} = \frac{m}{m - v}\,. \tag{3.5}$$

For all times t during the bending process the bending forces of the cantilever F_c and the pillar F_p are balanced, or mathematically formulated

$$F_p = F_c\,. \tag{3.6}$$

As discussed in subsection 2.1.1 for small deflections the correlation between the bending forces is assumed to be linear (Hook's law). With the spring constants of the cantilever k_c and the pillar k_p this leads to

$$x_p k_p = x_c k_c \tag{3.7}$$

or due to the fact, that the balance of forces must hold true for all times

$$\Delta x_p k_p = \Delta x_c k_c\,, \tag{3.8}$$

which leads to the equation for the pillar spring constant

$$k_p = \frac{\Delta x_c}{\Delta x_p} k_c\,. \tag{3.9}$$

Combined with the derived equation 3.5 a term for the pillar spring constant in dependence of the slope of the bending part of the calibration curve m, the velocity of the stage v and the spring constant of the cantilever k_c, is obtained.

$$k_p = \frac{m}{m - v} k_c \tag{3.10}$$

At the beginning of the calibration process the cantilever touches the pillar below the absolute length l of the pillar as can be seen in Figure 3.8. During the calibration it slid to the edge and the pillar snapped back to its original position. This means, that in fact the calibration process averages over a pillar length between the first contact at a height of l' and the real pillar length l at the point where they loose contact. To take into account this matter one can derive with the equation 2.15 and $l' = l - \Delta l$ the corrected spring constant

$$k_p = \underbrace{\left(\frac{l - \Delta l}{l}\right)^3}_{\text{correction factor}} k_p'\,. \tag{3.11}$$

Here k_p' represents the uncorrected spring constant calculated using equation 3.10. Strictly

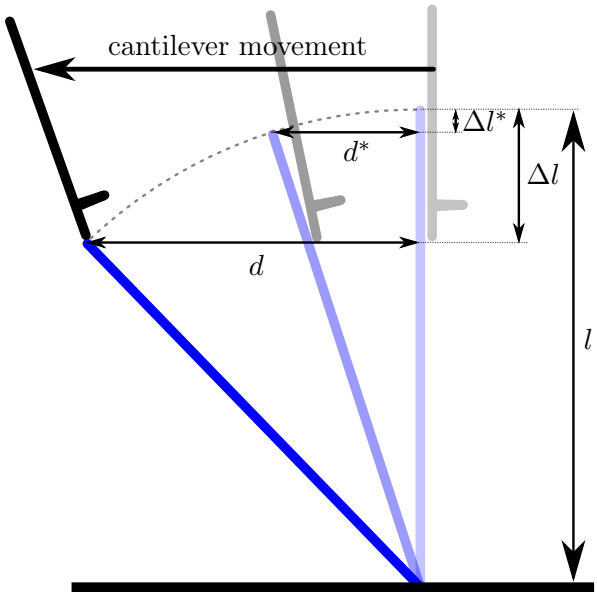

Figure 3.11: This illustration shows the geometrical data needed for the approximation of the pillar length correction value Δl and Δl^*. Here, the blue line represents the pillar with the length l as a stiff rod. It is deflected the distances d and d^* from its original state by the cantilever. The deflection d represents the full deflection of the pillar during the calibration process and d^* the deflection corresponding to the linear fitted part of the calibration curve at the beginning of the calibration process (see Figure 3.10).

speaking, the difference Δl between the real length of the pillar l and the point of contact l' is a function of time. At the initial contact between the cantilever and the pillar, Δl can be geometrically estimated to

$$\Delta l = l - \sqrt{l^2 - d^2} \tag{3.12}$$

with d being the maximum deflection of the pillar seen as a stiff rod at the moment when cantilever and pillar lose contact (see Figure 3.11). Since the pillar is not a stiff rod this rough geometrical approximation underestimates the real length of Δl due to the bending of the pillar. Despite this fact, this estimation was sufficient for our purposes.

In an actual experiment the pillars are bent less than in the calibration process, because of that the linear fitting region to determine the slope m was always chosen to be at the start of the deflection curve. That meant, the movement of the contact point and with it the variation of the pillar length correction Δl did change from the initial value of Δl to approximately $\Delta l' = \Delta l - \Delta l^*$ at the deflection d^*, which corresponded to the linear fitting range. The value for Δl^* could also be estimated by the equation 3.12 using the deflection d^*. Δl^* was always lower than 10 % of the length correction Δl meaning for typical pillar geometries, that the spring constant correction factor in equation 3.11 varies less than 1 %. Compared to other sources of error, this had only very minor influence on the calculated spring constants, that's why we neglected it.

Due to this fact, we used the directly calculated estimation of Δl as length correction to calculate the spring constant correction factor in equation 3.11.

Four frames of an actual calibration process are shown in Figure 3.12. Following the deflec-

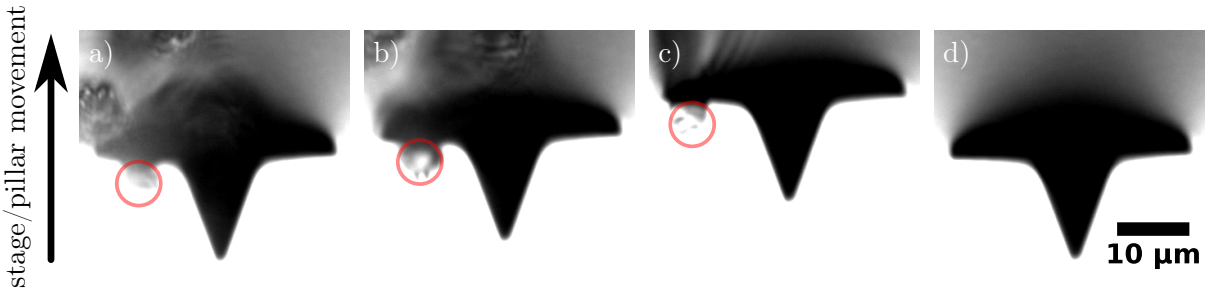

Figure 3.12: Four micrograph frames of a pillar calibration process. The pillar (red circle) is moved by the stage, in this case upwards, towards the fixed cantilever (see also Figure 3.8). From a) the contact between cantilever and over b) the linear deflection of the cantilever and pillar and c) the maximum deflection frame to d) the loose of contact between them and the snap back of the cantilever to its original position. With known pixel to micrometer conversion, stage velocity and the tracked cantilever position, calibration curves, as the one shown in Figure 3.9, were plotted and the pillar spring constant was determined.

tion of the cantilever with the ICARUS feature tracking software allowed the plotting of the calibration curve Figure 3.9. As mentioned at the beginning of this section, pillars were either directly calibrated, or a calibration field was created besides the force mapping pillar field. In the second case, ten or more pillars of the calibration fields, with comparable geometries to the pillars in the force mapping field, were calibrated. Afterwards, the corrected spring constant was determined by equation 3.10 and equation 3.11. The deviation was then used as error of the spring constants for the force measurements.

3.6 Cells

Life cell experiments were performed using rat embryonic fibroblasts (REF), which were stably transfected to express yellow fluorescent proteins (YFP) fused to their paxillin protein. These cells were kindly provided by B. Geiger[22]. Experiments showed, that the cells have the exact same proliferation, spreading and motility behavior as wild type REFs [15]. They were chosen, due to the fact that they express both integrins ($\alpha_5\beta_1$ and $\alpha_v\beta_3$) of interest, are adherent, motile and have an experimentally utile cell size.

3.6.1 Cell Culture

The REFs were cultured in DMEM medium[23] with 10 % fetal bovine serum[23] (FBS), 0.5 % penicillin streptomycin[23] (PS) and 1 % l-glutamine[23]. A 5 % CO_2 atmosphere at constant humidity and temperature of 37 °C was provided for cell culturing and during the experiments.

[22] Weizmann Institute of Science, Rehovot, Israel
[23] Gibco, Life Technologies, USA

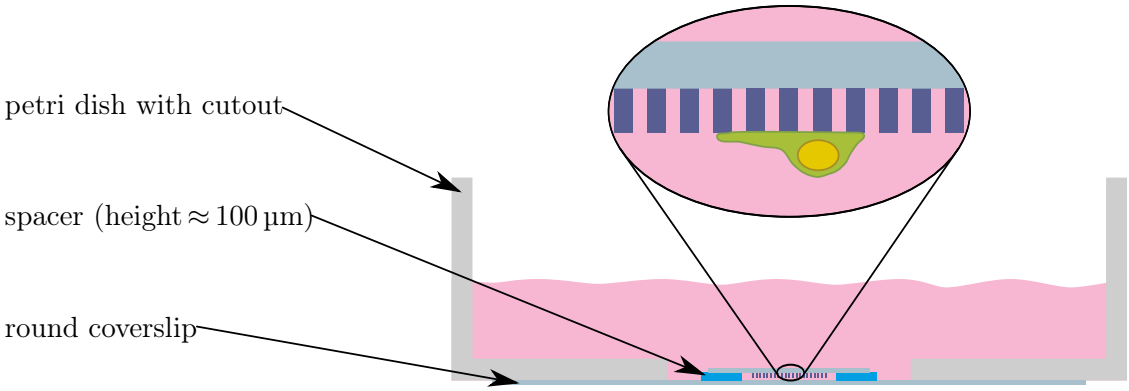

Figure 3.13: Schematic cross-section of the upside down configuration for the time lapse observation of cells on GPPPs. It is composed of: a 5 cm plastic petri dish with a round 3 - 4 cm diameter cutout, a round coverslip with 5 cm diameter glued to the bottom, two approximately 100 µm thick spacers glued on the bottom side to the round coverslip and on the top side to the upside down GPPP field coverslip with adherent cells. This configuration was then monitored on an inverted microscope.

3.6.2 Cells on GPPP Fields

To achieve an efficient functionalization of the gold nanoparticles, the GPPP fields were incubated over at least three hours in an 0.25 µM solution of the integrin selective peptidomimetics (with thiol linker, see Figure 2.8) or cRGD-thiol (Figure 2.7) in Milli-Q water. The molecules then covalently bound to the gold nanoparticles, forming a sulfur-gold bond similar to the linker reaction described in section 3.2 and visualized in Figure 3.2. These GPPPs were rinsed with sterile water three times for 10 min to get rid of unbound ligands, before seeding the cells.

The REFs used for the experiments had a passage count between 5 and 15. They were detached from the culture flask by accutase[24] and seeded on the functionalized GPPPs in standard medium. For one hour they were put in the incubator at 37 °C and 5 % CO_2 atmosphere. This initial attachment time was necessary to allow the upside down flipping of the GPPPs with still adherent cells. These steps enabled the monitoring of the cells and the GPPPs with the Axio Observer[25] inverted microscope. To prevent a sample drift during the long term experiments and to fix the upside down coverslip it was glued with two component silicone glue[26] on two approx. 100 µm thick spacers, which were also glued to the bottom of a custom made petri dish (see Figure 3.13). Since common petri dishes have a bottom with a thickness of around 1 mm, most microscope objectives can not focus on objects through them due to their working distance of below 1 mm. To overcome this, custom made petri dishes were produced by cutting

[24] StemPro, Life Technologies, USA
[25] Zeiss, Germany
[26] Twinseal, Picodent, Germany

out the bottom of a standard plastic petri dish and replacing it with a round glass coverslip[27] having a standard thickness of 0.17 mm.

For a standard experiment brightfield and fluorescence (YFP) images were acquired every 10 min over at least 8 h. To be able to monitor the whole pillar array with the 40x/0.75 objective[28], the built in "mosaic"-function of the microscope came into use. The software controlled the microscope which then scanned the whole region of interest while taking single images with a predefined overlap. Furthermore, the software allowed a stitching of these images into one single big overview image.

3.6.3 Fixing and Immunostaining

To study the influence of the two different integrin selective ligands on the adhesion and actin bundle formation of the REFs on GPPPs, the cells were fixed with paraformaldehyde and stained for actin, paxillin (to enhance the weak YFP fluorescence) and zyxin 5 h after seeding.

The actual fixing and staining procedure was the following:

- washing in phosphate buffered saline (PBS)[29]
- fixing with 3,7 % paraformaldehyde[30] (20 min)
- perforation of the cell membrane with 0.1 % Triton X-100[30] (5 min)
- blocking with 1 % bovine serum albumin[30] (BSA) solution (1 h)
- incubation with primary antibodies for zyxin (Z4751)[30] and paxillin (610569)[31], both at 5 µg/ml (2 h)
- three washing steps in 1 % BSA (15 min each)
- incubation with two secondary antibodies Alexa647 (MP02764)[32], Alexa488 (MP00852)[32], both at 10 µg/ml and palloidin-TRITC[30] at 50 µg/ml (1 h)
- washing three times in PBS (15 min each)

All antibodies and staining reagents were dissolved in the 1 % BSA in PBS solution. For storage the samples were kept in a 1 % PS in PBS solution at 4 °C. To monitor the cells on the inverted microscopes, the same "flipping and fixing" steps described in 3.6.2 were necessary.

[27] Metzel-Gläser, Germany
[28] 440351, Zeiss, Germany
[29] PAA, Austria
[30] Sigma-Aldrich, USA
[31] BD Biosciences, USA
[32] Life Technologies, USA

3.7 Actin

For the conducted actin experiment the professional purification, storage and handling of globular and filamentous actin was crucial. The following sections will shortly outline these points.

3.7.1 Actin Purification and Storage

In spite of many commercial providers of globular actin, we preferred to purify the actin in house to achieve a better quality. The most important quality was a high percentage of biological active actin monomers which leads to actin filaments with a high contour length. Regardless of the in most cases precise molecular weight of the commercially available actin of 42 kDa the bioactivity was significantly lower than the actin purified by C. Mollenhauer[33] in our laboratories. One factor influencing the polymerization properties is the storage temperature of the globular actin [169]. C. Mollenhauer performed the purification following the standard protocols [89, 112, 152] at least once every 6 months to prevent the usage of actin stored too long.

chemicals	**mol. weight [g/mol]**	**concentration [mmol/l]**	**mass per 1 [mg/l]**
TRIS-HCL	121	2	242
$CaCl_2 \cdot 2H_2O$	147	0.2	29
DTT	154	0.2	31
NaN_3 (20%)	65	3	1 ml
Ma_2-ATP	551	0.2	110

Table 3.1: Chemical composition of the g-buffer with a pH of 8.0.

To dilute and handle the purified globular actin it was suspended in g-buffer (g from globular). Its composition is listed in Table 3.1. Usually the concentration of globular actin in g-buffer after the purification process was between 0.2 and 0.3 mg/ml. This was measured by UV-Vis spectroscopy[34] in a 50 µl cuvette[35] by applying the extinction coefficient of 0.63 mg/ml at a wavelength of 290 nm [58] for the concentration calculation.

To achieve a strong binding between the streptavidin coated microbeads embedded on the PEG pillar tops (see subsection 3.4.2) and the actin filaments, biotinylated globular actin was used. Commercially acquired lyophilized biotinylated globular actin[36] was reconstituted in Milli-Q water and then added to the purified actin solution in molar ratios of 1:25, 1:50 and 1:100 of the biotinylated actin to purified actin. For the presented experiments the ratio of 1:50 was chosen. It had the right balance between affinity to the streptavidin coated beads and achievable filament length. At this ratio the average distance of to biotinylated actin

[33] Max Planck Institute for Intelligent Systems, Stuttgart
[34] Plate Reader M200, Tecan, Switzerland
[35] 105.202-QS, 10 mm light path, Hellma, Germany
[36] AB07, Cytoskeleton, USA

monomers was around 150 nm. To prohibit the denaturation of the actin, the produced mixtures of biotinylated and normal globular actin were dripped into liquid nitrogen leading to frozen drops of 25 ± 5 µl, which were stored at -80 °C and used for up to 6 months.

3.7.2 Actin Polymerization, Fluorescence Labeling and Experimental Handling

The polymerization of the globular actin was initiated by exposing the actin monomers to a buffer solution of higher ionic strength [36, 112, 153]. This buffer solution was called f-buffer (f for filamentous) and its chemical composition is listed in Table 3.2. Addition of fluorescently labeled phalloidin to the polymerizing actin resulted in a stabilization and fluorescence labeling of the filamentous actin. This stabilization led to an inhibition of the filament depolymerization. In consequence, the filament length was significantly enhanced and its rigidity increased, indicated by the elevation of the persistence length from 8 to 16 ± 1 µm [9, 10, 16, 63, 84, 93, 110].

chemicals	**mol. weight** [g/mol]	**concentration c** [mmol/l]	**mass per 100 ml** [mg/100 ml]
TRIS-HCL	121	2	24.2
$CaCl_2 \cdot 2H_2O$	147	0.2	2.9
DTT	154	0.2	3.1
$MgCl_2 \cdot 6H_2O$	203	2	40.6
Mg-ATP	507	0.5	25.3
KCl	75	100	750

Table 3.2: Chemical composition of the f-buffer with a pH of 7.4 and a high ionic strength to initiate the polymerization of the globular actin.

Experimentally, the polymerization was induced by mixing 12.5 µl of the globular actin solution, 82.5 µl f-buffer and 5 µl of phalloidin-TRITC[37] (dissolved in methanol to 0.1 µM) leading to a fluorescently labeled approximately 5 µM filamentous actin stock solution, which was used for up to two weeks and stored at 4 °C. The obtained actin filaments had a contour length of 10 - 30 µm. For the experiments this stock solution was then diluted in the t-buffer (t for test) with the composition specified in Table 3.3. Usually, ratios of 1 : 20 filamentous actin solution to t-buffer were used.

The bundling agents used for the experiments described in section 4.2 were also diluted in t-buffer. The 50 mM Mg^{2+} solution, as the most frequently used bundling buffer, was produced by adding 50 µl of a prepared 1 M $MgCl_2$ solution in Milli-Q water to 1 ml of f-buffer.

[37] Sigma-Aldrich, USA

chemicals	mol. weight [g/mol]	concentration c [mmol/l]	mass per 100 ml [mg/100 ml]
Imidazol	69	25	172.5
$MgCl_2 \cdot 6H_2O$	203	4	81.2
EGTA	380	1	38
KCl	75	25	187.5

Table 3.3: Chemical composition of the t-buffer with a pH of 7.4.

3.8 Microfluidics

Microfluidics in general is used to handle small volumes of liquids for chemical, biological or physical experiments, where either the compounds are expensive, time consuming to produce or, as in our case, the objects of interest themselves are in the size range of microns [50, 64, 162]. To give the actin experiments a controlled and reproducible environment some basic microfluidic techniques were employed.

In this section the required steps for the production of the experimental chamber made out of poly(dimethylsiloxane) (PDMS) are described. PDMS is a silicon-based organic polymer which is transparent for visible light and used in a wide variety of medical or scientific devices and even in industrial products [11, 104, 151]. The process of producing PDMS structures with micrometer small features covering areas up to square centimeter or even more is called soft lithography and was established by Whitesides et al. [29, 166]. It usually consists of three steps: cast master production by photolithography, effusion of the PDMS structure and construction of the microfluidic chamber.

The received microfluidic chambers where used for the actin bundling experiments. They allowed the necessary controlled exchange of liquids e.g. the buffer and bundling solution. The following section depicts the fabrication procedure.

3.8.1 Photolithography

The dimensions of the needed PDMS chambers were in the range of 50 µm in the xy-plane, which is far from the possible feature sizes of below 1 µm [44]. This fact simplified the photo lithography process by allowing direct printing of the needed illumination masks, with the desired channel structure, on a transparent polymer foil[38]. For structures under 10 µm more time consuming laser illumination methods are necessary.

To produce the negative casting mold for the PDMS channels, the negative SU-8 photoresist[39] was used. SU-8 consists of EPON epoxy resin and γ-butyrolactone or cyclopentanone as a solvent. It is available in many different viscosities to allow the variation of the film thick-

[38] JD Photo-Tools, United Kingdom
[39] MicroChem, USA

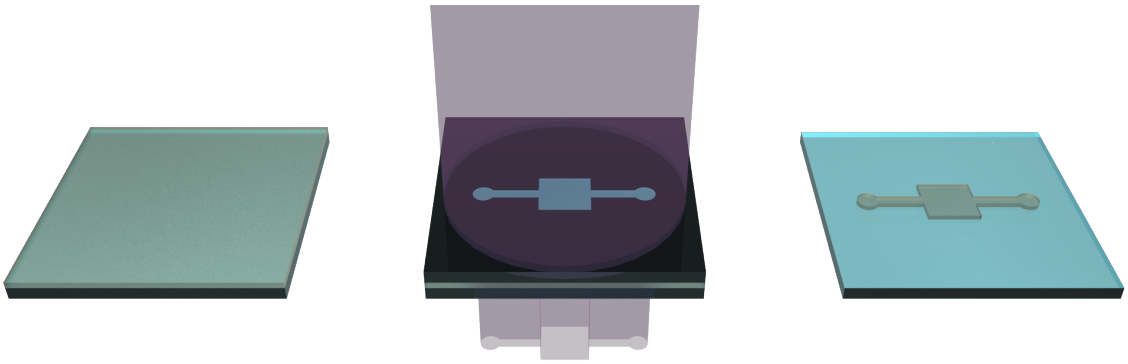

Figure 3.14: From left to the right this schematic shows the crucial steps of the SU-8 illumination process. First the SU-8 is spin coated on the glass substrate (left), then the SU-8 is illuminated through the mask (middle) and finally the not illuminated and thus not-polymerized SU-8 is washed away leaving the PDMS effusion negative on the glass (right).

nesses when spin coated on a glass slide or silicon wafer. Additionally, the SU-8 resist contains triarylsulfonium hexafluoroantimonate as photo initiator of the polymerization process which has a maximum absorption at a wavelength of 365 nm. The epoxy and the solvent themselves have a high transparency in the UV wavelengths. These properties of the SU-8 photoresist together with the spin coating possibilities allow structure thicknesses of under 1 and up to 300 µm [13, 108].

We used 2 x 2 inch sized glass slides[40] which were cleaned using a 20 % extran solution for 10 min in an ultrasonic bath, rinsed with Milli-Q water and dried for 30 min at 200 °C. To achieve a desired thickness of 70-150 µm the SU-8-2075 was used. It features the needed viscosity to acquire these desired heights when spin coated on the glass slides. The exact photolithography working steps performed in a clean room were the following:

- the extran cleaned and dried glass slides were spin coated with 2 ml of SU-8-2075 for 5 s at 500 rpm followed by 32 s at 1900 - 2200 rpm
- "pre-baking" for 3 min at 65 °C and 7 min at 95 °C on a hot plate
- fixation of the foil negative mask on a 2 x 2 inch glass slide by adding a drop of water between the glass and the foil
- mounting the illumination mask into the mask aligning and illumination machine[41]
- illumination with the 400 W HBO lamp connected to the mask aligner for 14 - 15 s
- "post exposure baking" for 1 min at 65 °C and 5 min at 95°C

[40] Krankenhaus- und Laborbedarf Manfred Fremdling, Germany
[41] MJB3; SÜSS MicroTec, Germany

- rinsing for 3 min in SU-8 developer[42]
- dry blowing with nitrogen

After these steps a negative of the desired PDMS channel structure consisting of the photo resist remained on the glass slide. To simplify the detachment of the PDMS after the effusion and curing process described in subsection 3.8.2, the casting negatives were silanized with 1H,1H,2H,2H-perfluorooctyltrichlorosilane[43]. For at least 4 hours the structures were put into an evacuated desiccator with a small petri dish containing 300 µl of the silane. The chemical reaction of the surface silanization is described in section 3.3 and visualized in Figure 3.3.

3.8.2 Microfluidic PDMS Chamber Construction

After obtaining the effusion negative via the SU-8 illumination process explained in subsection 3.8.1, the PDMS microfluidic chamber was constructed. First, the fluid pre-cured PDMS was mixed by stirring the curing agent and the PDMS[44] in a ratio of 1 : 10 followed by a devolatilization in a desiccator. Air bubbles, generated by the stirring of the viscous fluid, bursted thereby. Afterwards, 1 ml of the pre-cured PDMS was deposited with a 5 ml syringe on the SU-8 structure and a 24 x 60 mm coverslip pressed flat on top of it to achieve a thin PDMS layer between the upper coverslip and the SU-8 glass substrate (see Figure 3.15). This structure was then cured at 65 °C for at least 3 hours. Due to the silanization of the effusion form, the PDMS could not attach to it and prefers to stick to the upper not silanized thin coverslip. With the help of a razor blade and ethanol (70 %) the coverslip could be removed from the effusion negative. This way, the microfluidic channel and chamber out of PDMS on a coverslip were obtained.

As described in subsection 3.4.2 the produced PEG pillars are covalently bound to a glass coverslip. In this coverslip two holes of 1 to 2 mm in diameter, the same distance as the end to end length of the microfluidic PDMS channels, were drilled. Through these holes two PTFE-tubings[45] (40 cm) were inserted and fixed with epoxy[46] to the coverslip on the opposite side of the PEG pillar structures. These tubes had an outer diameter of 0.6 mm and a inner diameter of 0.3 mm. After the epoxy curing (15 min at room temperature) and cutting the overlaying tubing, the coverslip with the PEG pillar structures and tubing was aligned to exactly fit on the microfluidic PDMS channel and gently pressed on it (see Figure 3.15). To control the leak tightness a 1 ml syringe with a 0.4 mm thick syringe needle[47] was inserted into one end of the PTFE-tubing and the other end was doused into a t-buffer reservoir. By gently pulling on the

[42] mrDev 600; MicroChem, USA
[43] ABCR, Germany
[44] Sylgard 184 Silicone Elastomer Kit; Dow Corning, USA
[45] # S 1810-04; Bohlender, Germany
[46] Araldite, Roth, Germany
[47] BD Microlance, BD, USA

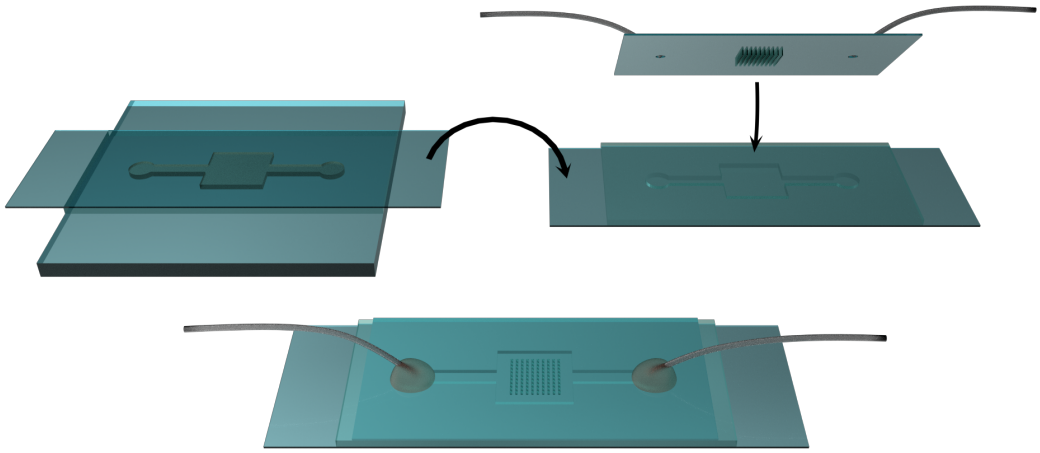

Figure 3.15: This illustration depicts the construction of the microfluidic chamber used for the actin experiments. The thin PDMS layer between the upper thin coverslip and the SU-8 effusion negative on the lower thick glass substrate is shown (upper left). After careful detachment of the PDMS structure the PDMS sticks to the thin coverslip. The coverslip with PEG pillars two drilled holes and PTFE-tubings fixed by epoxy is pressed on top of the PDMS chamber leading to a sealed microfluidic experimental chamber (bottom middle). The microfluidic chamber had a base area of 6 mm x 6 mm and a height of 70 - 150 µm

syringe, the t-buffer was sucked in and led, due to the slight underpressure, to an additional tightening of the chamber. This experimental chamber was then stored at 4 °C to prevent the growth of fungi or other contaminations until used in the experiments described in section 4.2.

3.9 Image Processing, Tracking and Data Analysis

All images taken during the experiments were acquired in the highest possible bit depth of the used cameras which was usually 12 bit for the Orca cameras and handled as 16 bit TIFF files. Basic processing and evaluation steps were done using the open source software Fiji (Fiji is just ImageJ) [141] and several included and added plugins as well as self-written macros. The microscopy images shown in this work were processed using Fiji including steps to adjust settings like contrast and brightness as well as the composition of overlay images and the output of compressed images and videos.

Tracking objects in time series acquisitions was one main challenge tackled by the utilization of three different software tools:

- **Algorithms by John C. Crocker and David G. Grier:** These algorithms are intended to track micron sized spherical particles with a very high precision of down to

10 nm in the focal plane. This is achieved in five steps described in [20] and in subsection 2.1.2 of theoretical background chapter. To be able to use the algorithms in a convenient manner a Matlab compatible version of the algorithms was written and kindly provided by the group of M. Kilfoil[48]. These Matlab[49] scripts were used to track the position of the microsphere particles embedded on the pillar tops for the investigation of the contractile actin networks described in section 4.2.

- **ICARUS:** To be able to track objects without a clear shape like microspheres the software called ICARUS came into use. The software was developed by S. Gibson et al. [45] and later bought and commercialized by the company "The Pixel Farm"[50], fortunately they still provide a free version for non commercial use[51]. With this software it is possible to track contrast rich objects of variable size with a sub pixel precision. It mainly came into use for tracking the cantilever position during the calibration process described in section 3.5.

- **Mosaic plugin:** This tracking software was developed by I. F. Sbalzarini and P. Koumoutsakos [140] and provided as Fiji plugin[52]. It is also based on the algorithm of J. C. Crocker and D. G. Grier with some computational optimizations. The plugin allows the tracking of particles in image sequences over time in two dimensions. It is possible to follow the movement of a variety of particle sizes and intensities. Due to the fact, that for small deflections and by using a well selected focal plane during the experiments the acquired bright field images of the GPPPs showed a high intensity at their center which moves with the deflection of the pillar. The plugin was able to track these high intensity regions as the GPPPs were bent by the REFs during the time lapse experiments described in subsection 3.6.2.

The obtained tracking data from the above mentioned methods were then processed using Matlab. Self-written scripts were used for three purposes:

- **Drift elimination:** These scripts were applied to eliminate xy-drifts occurring over the time laps acquisitions. They were mainly caused by the stage movement during the "mosaic recordings" of the cell experiments. To achieve this, several ($n > 6$) pillars which had no cell contact during the whole time frame of interest were chosen and the mean of their combined trajectories was calculated. This drift correction trajectory was then subtracted from all pillar trajectories. Since every pillar without cell contact still showed

[48] Department of Physics, University of Massachusetts at Amherst, `http://people.umass.edu/kilfoil/downloads.html`
[49] MathWorks, USA
[50] `http://www.thepixelfarm.co.uk/`
[51] `http://www.colinlevy.com/tuts/IcarusTutorials/Icarus.php`
[52] `http://www.mosaic.ethz.ch/Downloads/ParticleTracker`

a finite nonzero displacement, the mean displacements of at least 6 of these pillars was used to determine the tracking accuracy (subsection 3.9.1).

- **Determination of the no force position:** As described in subsection 3.6.2 the cells were already spreading on the GPPPs at the beginning of the time laps recordings. This fact, and the approximately 1 µm uncertainty of the motor stage during the illumination process, led to the necessity to estimate the no force positions of the pillars beneath the cells. Under the hypothesis, that the position with the longest length of stay is the no force position the following algorithm was generated and applied. A rectangular area with side lengths 0.3 pixel longer than the tracking accuracy (see subsection 3.9.1) was defined at all tracking positions for each pillar. Then the rectangles enclosing most tracking positions over the observed time frame were identified for each pillar trajectory. These rectangles and the tracking coordinates in them were determined and saved. Thereby each pillar trajectory had one correlated rectangle with the maximum number of tracking points in it. For all these rectangles the mean of the inclosed positions were calculated. These mean positions were then defined as the no force positions for each pillar.

- **Determination of pillar deflection and forces:** The main data processing task was the conversion of the raw tracking data to deflections and forces. After the previous two methods of data tracking and handling the next step was to gain the real force data. This was achieved by multiplying the determined pillar spring constants (see section 3.5) and the pillar deflections converted from pixel values to micrometer. Therefore, the pixel to micrometer ratio was obtained by taking images of a micro scale bar with all used objectives and microscope settings.

Furthermore, Matlab was used for some other tasks including the plotting of all graphs shown in this work and the comparison between the different fluorescence images of fixed and stained REFs on the GPPPs (see subsection 3.6.2 and subsection 4.1.5).

3.9.1 Tracking Accuracy

How accurate the deflection of a pillar is trackable defines, together with the spring constant (and errors), the force resolution.

To determine the tracking accuracy the pillars were tracked under no (additional) force influences. In the case of the GPPPs the brightfield image of the whole pillar was tracked, which showed a bright spot at the pillar center if the focus was set right (see Figure 4.5). In the case microbead functionalized PEG pillars the embedded beads on the pillar tops were used instead.

To appoint the tracking accuracies, the different experimental time frames and configurations had to be taken into account. To do so, the tracking accuracy for the GPPPs were determined by

tracking the displacement of 6 (or more) pillars without cell contact during the cell experiments. Then their drift was calculated and subtracted (section 3.9). The tracking accuracy was then defined as the standard deviations of these pillars displacements.

For the bead functionalized pillars employed in the actin experiments drift was negligible, due to the much shorter experimental time frames (less than 5 min). Therefore, the tracking accuracy was determined by recording and tracking the pillars without attached actin filaments or buffer exchange for 5 min, followed by the same calculations as for the GPPPs.

These accuracy determinations led to an overall mean pixel accuracy of 0.29 ± 0.04 pixel for the GPPPs and 0.11 ± 0.02 pixel for the bead PEG pillars. By taking the corresponding pixel factors of $6.38\,{}^{\text{pixel}}/_{\mu\text{m}}$ (cell experiments) and $5.11\,{}^{\text{pixel}}/_{\mu\text{m}}$ (actin experiments) into account this led to 45 ± 6 nm (GPPPs) and 22 ± 4 nm (microbead PEG pillars). In the following the accuracies were approximated to 50 nm for the GPPPs and 25 nm for the bead functionalized PEG pillars.

Chapter 4

Experiments

This chapter summarizes the experiments performed for this work. It is divided into two sections. The first section addresses the characterization of the GPPPs and the conducted experiments on integrin dependent traction forces of fibroblasts. The second section explains the adaption of the PEG pillars, functionalized with surface coated microspheres, for the formation of actin networks on top of them. Upon bundling these actin networks with Mg^{2+}-ions they contracted and thereby exerted forces. PEG pillars with a high sensitivity (spring constant $k < 0.5\,^{\mathrm{nN}}/_{\mu\mathrm{m}}$) were used to determine these forces.

4.1 Studies on Cell Forces in Dependence of $\alpha_v\beta_3$- and $\alpha_5\beta_1$-Integrin Selective Adhesion

The following sections describe the most important steps in the development and the application of the GPPPs as force sensors. Afterwards, differences in the behavior and the force development of REFs seeded on these GPPPs functionalized with $\alpha_v\beta_3$- or $\alpha_5\beta_1$-integrin selective peptidomimetics were determined and analyzed.

4.1.1 Characterization of the Gold Nanoparticle Patterned PEG Pillars

The fabrication process described in subsection 3.4.1 was based on two established techniques, the transfer of gold nanoparticle structures to hydrogels and the polymerization of PEG pillars. However, the combination of these two techniques was not trivial. To prove the concept it was important to show that the gold nanoparticles were transferred efficiently and that they retained their quasi hexagonal order on the PEG pillar tops.

Since the gold nanoparticles have a diameter of approximately 5 - 8 nm, the GPPPs could be examined only with an SEM. For that, the GPPPs were dried at room temperature and coated

with a thin carbon layer to prevent charging effects during the observation[1]. In the SEM the PEG, being a soft polymer, showed a fast degradation caused by the exposure to the electron beam. This made the acquisition of the gold nanoparticle structures on the PEG pillars a challenging task. As few as five scanning runs were sufficient to cause a wave-like deformation of the pillar top surface and to influence the order of the gold nanoparticles (see Figure 4.1 c). To reduce this effect and improve the image quality all recoding settings were done by focusing on one pillar, despite the negative effects on it. With these settings the stage was moved to a neighboring pillar and since the pillar tops are at the same height only one or two scans were necessary to get an image with just minimal wrinkling as can be seen in Figure 4.1 a.

Using gold nanoparticle structures with different spacing resulted in changes of particle spacing on the GPPPs. Two examples can be seen in Figure 4.1 b and d corresponding to nanoparticle spacing of 55 ± 5 nm and 100 ± 6 nm on the glass substrate obtained by BCML as well as on the pillar tops.

To control the influence on the order and distances of the transferred gold nanoparticle structures, the so-called order parameter Φ and the average distances between the particles were determined on the glass surfaces as well as on the PEG pillar tops. Originally the order parameter Φ was introduced for the description of two dimensional melting processes [103]. The order parameter Φ equals one for a perfectly hexagonal ordered lattice and decreases together with the order of the structure. For the determination of the order parameter Φ and the particle distance a Fiji plugin kindly provided by P. Girard was used. The evaluations showed that for the order parameter Φ the variation between the nanoparticle patterns on the glass surfaces and on the PEG pillars was $< 10\,\%$. Additionally, the particle distances revealed approximately $10\,\%$ smaller spacing on the PEG pillar compared to the glass surfaces. This effect was due to the drying process prior to the SEM image acquisitions, leading to a shrinkage of the pillars which results in a smaller particle distance. If this shrinkage was taken into account, also the particle distances only varied under $10\,\%$ between the glass surfaces and the PEG pillar tops.

These preliminary tests only considered the transfer of the gold particles, but did not take the pillar geometry or spring constant into account. The main task was to achieve GPPPs with surfaces to which a REF can adhere, spread and migrate on. Additionally, they had to have rigidities allowing the cells to bend them and thereby enabling the measurement of traction forces. Mature focal adhesions of REFs have a long axis of approximately 3 µm. To allow the formation of these mature focal adhesions on the GPPPs we defined 3.5 ± 0.5 µm as desired diameter range of the pillars. Furthermore, it is known that REFs prefer to adhere to hard substrates [113, 170]. Therefore, the spring constant for the cell experiments was chosen to be around $15\,^{\mathrm{nN}}/_{\mu\mathrm{m}}$ being much stiffer than the possible spring constants of < 0.5 nanonewton (used for the *in vitro* actin experiments described in section 4.2). According to these demands

[1] MED 020 Coating System, Bal-Tec, Liechtenstein

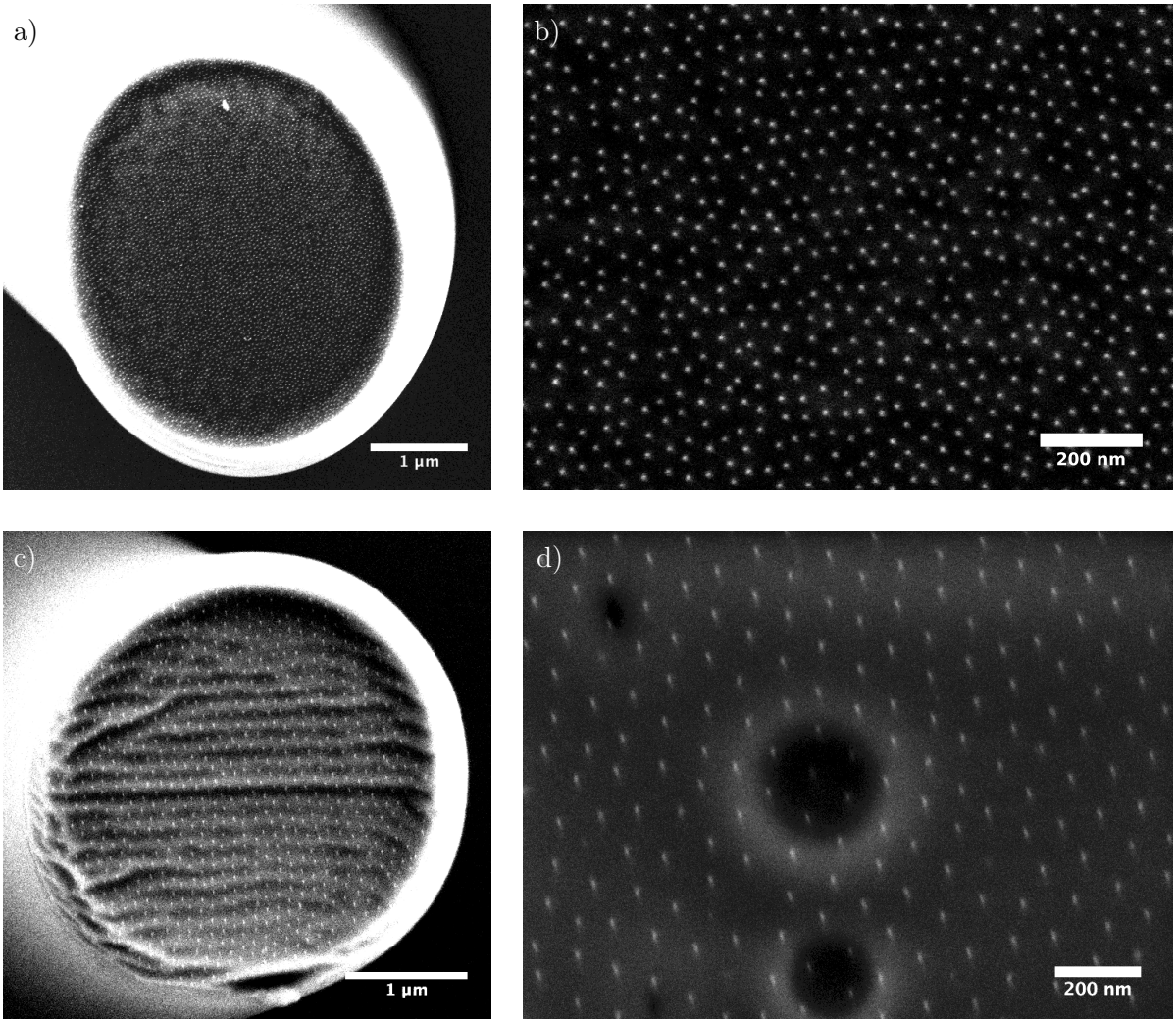

Figure 4.1: SEM images of two GPPPs with 55 ± 5 nm and 100 ± 6 nm gold nanoparticle spacing. The two overviews a) and c) show the top surface of a GPPP, demonstrating that the complete top side of the pillars is covered by the quasi hexagonal gold nanoparticle structure. The higher magnification of the pillar tops in b) and d) clearly displays that, even after the transfer of the gold nanoparticles to the PEG, the spacing is preserved. In the images c) and d) the damage done by the electron beam can be seen as wrinkling in c) or dark spots in d).

the GPPP fabrication process was optimized. The standard pillar used for the cell experiments was made of PEG-700, had a diameter of $3.5 \pm 0.5\,\mu m$, a length of $13 \pm 1\,\mu m$ and a spring constant of $15 \pm 2\,^{nN}/_{\mu m}$. By taking equation 2.15 and solve it to the Young's modulus

$$E = \frac{4kl^3}{3\pi r^4}, \tag{4.1}$$

it was estimated to approximately 1.5 MPa. This value is much lower than the expected bulk elasticity of about 8 MPa [87]. A possible reason could be the short illumination times of $\leq 1\,s$. Thereby, the polymerization is not completed, meaning that not all possible mesh connections of the radical network polymerization, seen in Figure 3.5, are formed. Less cross connections within the network mean a larger mesh size, higher flexibility and lower Young's modulus. In fact, to test this, pillars with the same geometry, but for over 5 s or longer had a significantly higher spring constant k and therefore a higher Young's modulus E. The production of pillars with spring constants of about $15\,^{nN}/_{\mu m}$ and the desired geometries were reproducible.

Alternatively, if a fully polymerized PEG network had been desired, longer PEG chains would have been used. However, these longer PEG chains would require much longer illumination times ($t > 10\,s$ per pillar) for full polymerization, rendering the pillar illumination process for larger pillar fields impractically long.

4.1.2 Rat Embryonic Fibroblasts on Functionalized GPPP Fields

The SEM analyses demonstrated that the fabrication of the GPPPs indeed was achieved by combining two established fabrication techniques. However, for the application as traction force sensors, the functionalization of the gold nanoparticles was crucial. One concern regarded the possibility that the gold particles would be completely embedded into the top surfaces and covered by PEG making them inaccessible for the functional molecules. Therefore, the next step was to check whether the gold nanoparticles were accessible for functionalization. Furthermore, it had to be tested if the chosen geometry and spring constant offered a suitable stiffness and enough ligands to mediate cell adhesion.

In the first functionalization experiments thiolated cRGD (Figure 2.7) was incubated onto the GPPPs. After the washing steps, REFs were seeded on these GPPPs and monitored for 5 h. As shown in Figure 4.2, the cells were able to adhere and spread on the cRGD functionalized GPPPs with a gold nanoparticle spacing of $55 \pm 5\,nm$. Monitoring paxillin (labeled by YFP) and thereby the focal adhesions (identified as brighter spots) these structures could be observed at the pillar positions. The brightfield images showed a bending of the pillars, demonstrating that the basic idea of the GPPPs as traction force sensors was functional. Unfortunately, in this preliminary experiment the focus plane during the image acquisition was not optimal, which impeded a proper tracking of the pillar deflections.

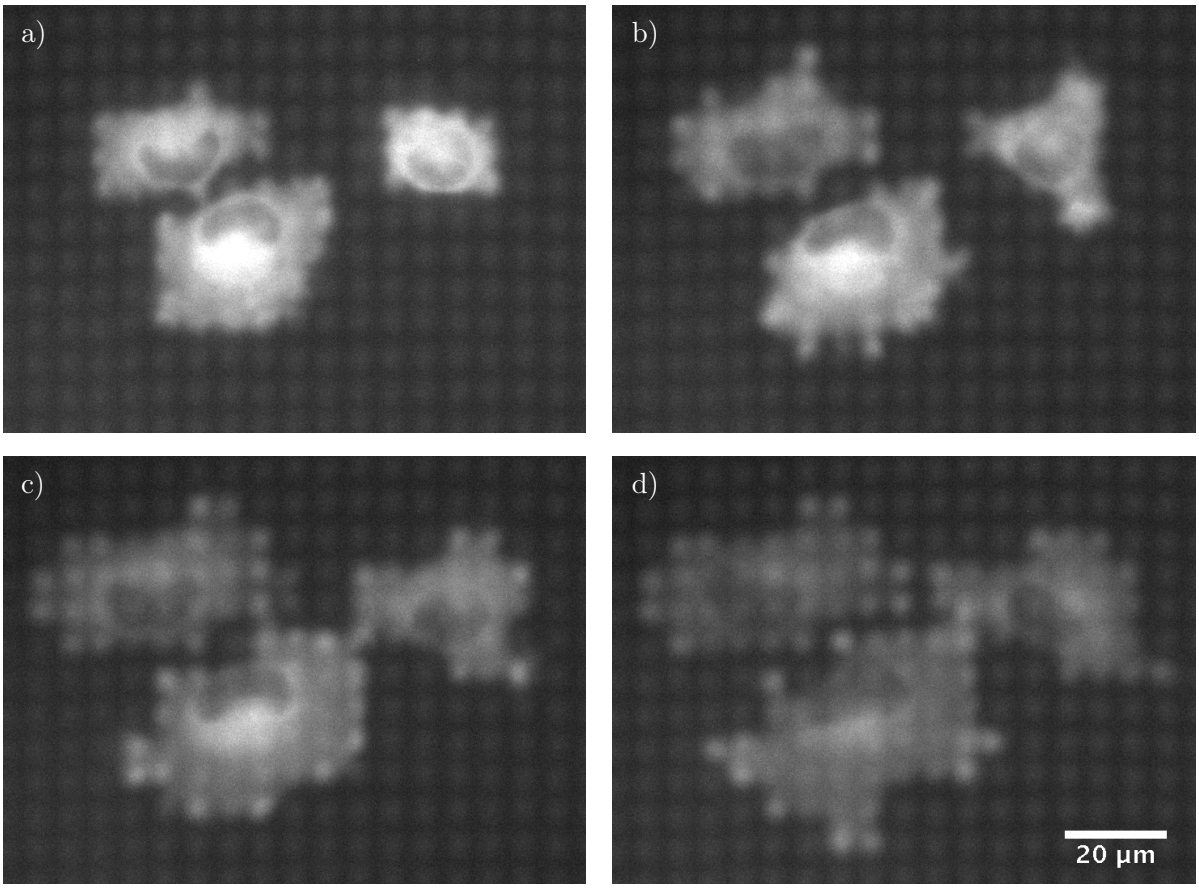

Figure 4.2: Fluorescence (YFP) images of REF cells spreading on GPPPs with a gold nanoparticle spacing of 55 ± 5nm and an cRGD functionalization. The chimeric YFP-paxillin fusion protein was stably expressed by the used REFs. Image a) was taken 30 min after seeding, b), c), and d) successively after additional 30 min each. The brighter spots, mostly located at the periphery of the cells, are paxillin clusters indicating the formation of focal adhesions. Note the weak auto fluorescence of the PEG pillars.

Due to their small size, the observation of the gold nanoparticles was not possible by conventional light microscopy. To show that the cells only adhere to the nanostructured and functionalized pillar tops they were seeded on cRGD functionalized GPPPs for 5 h, fixed, dried (at room temperature) and coated with a thin carbon layer. In the SEM both the cells and the gold particles were observed. The created micrographs, shown in Figure 4.3, revealed that the cells only bind to the pillar tops, more precisely to the functionalized gold nanoparticles. Because of the fixation and the drying process, the cells shrink and thereby the pillars are notably more bent than in a live cell experiment.

These preliminary experiments demonstrated the general applicability of the GPPPs as force sensors for cell adhesion and traction force studies. However, the availability of the two $\alpha_v\beta_3$- and $\alpha_5\beta_1$-integrin selective ligands made it possible to go about the question, if differences in

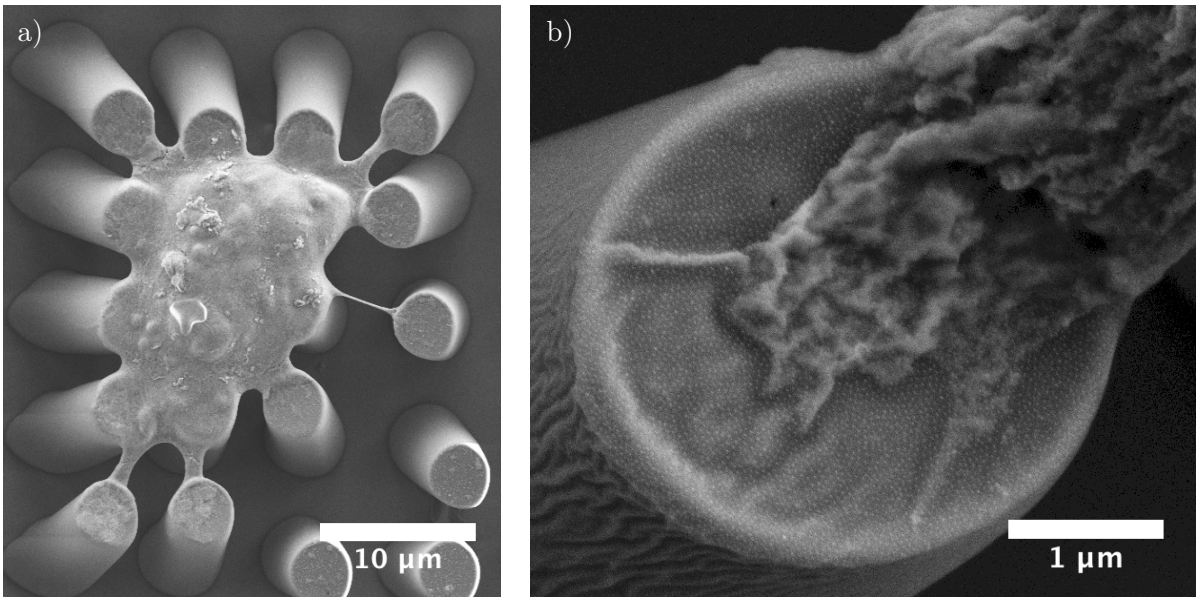

Figure 4.3: SEM micrographs of a) a whole REF and b) one cellular protrusion on a cRGD functionalized GPPP. As can be seen in a) the cell only adhered to the pillar tops and had bent the pillars. However, the pillars are significantly more bent than in a life cell experiment. Due to the fixation and drying process, the cell shrank and thereby bent the pillars. The closer look on one pillar top b) reveals that the gold particles are on the pillar surface and cell protrusion bound to the offered binding molecules.

the traction force and protein recruitment of the cells can be directly measured and observed by the GPPP arrays. Therefore, the GPPP fields were incubated with one of the two ligands, similar to the cRGD experiments, followed by a washing step and the seeding of the REFs. On both ligands adhesion, spreading and migration of the cells was observed.

As negative controls both PEG pillars without gold nanoparticles but with incubated ligands, as well as not functionalized GPPPs were tested by seeding REFs on them. In both cases the cells adhered after 12 h only to the glass surface surrounding the pillars and penetrated the regions between the pillars, but could not adhere on them.

4.1.3 Time Lapse Experiments of Rat Embryonic Fibroblasts on Integrin Selective Functionalized GPPPs

After demonstrating the general applicability of GPPP fields for cell studies time lapse experiments were designed and conducted. As described in subsection 3.6.2, a standard experiment started 1 h after seeding. A fluorescence (YFP-paxillin) and brightfield image was recorded every 10 min for at least 8 h.

The initial idea of directly monitoring the formation of the focal adhesions on the GPPP functionalized with either the $\alpha_v\beta_3$- or $\alpha_5\beta_1$-integrin selective ligand over longer time (>1 h),

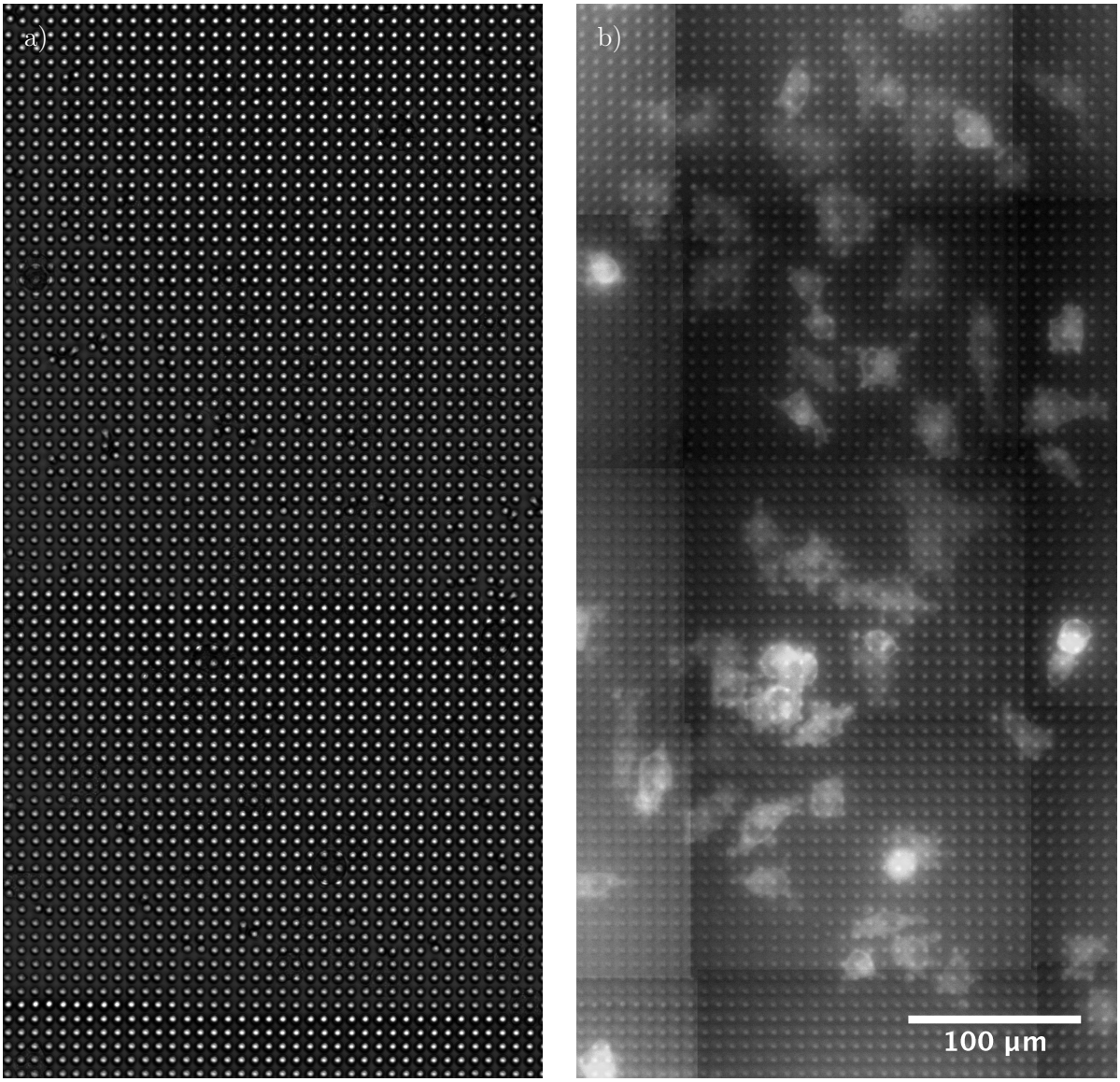

Figure 4.4: An overview of a typical GPPP field functionalized with the $\alpha_v\beta_3$-integrin selective ligand and spreading and migrating REFs. In the brightfield image a) the adherent REFs are barely visible. The image b) shows an overlay image of REFs and the pillar field composed of the brightfield image a) and fluorescence (YFP) channel. The images were taken approximately 2 h after seeding.

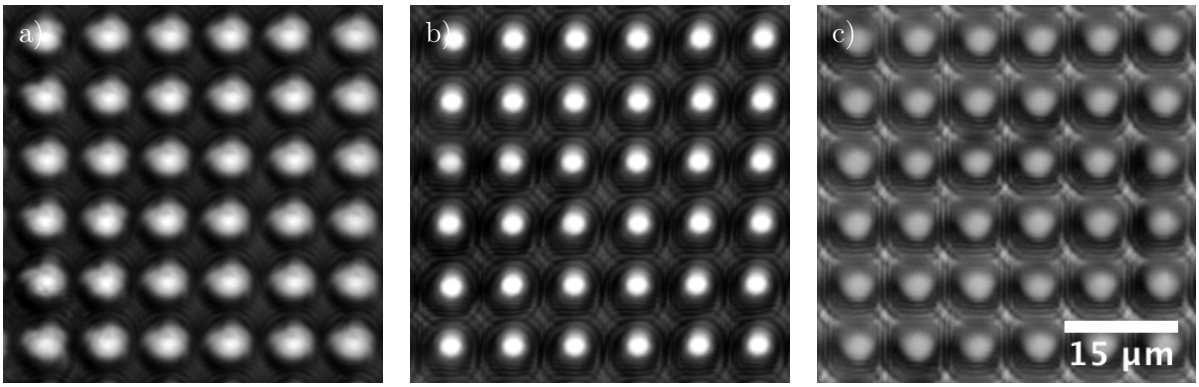

Figure 4.5: Micrographs showing different focus planes of the same pillar field area. For too low a) and to high c) focus setting the tracking algorithm was not reliable. Furthermore, for these settings the bending of a pillar only causes a distortion in the image and not a trackable movement. Was the focus chosen properly, as shown in b), the pillars could be tracked and the bright spots followed the pillar bending. A tracking precision of approximately 50 nm was achieved.

had to be reconsidered. It turned out that the fluorescence of the YFP labeled paxillin was weak, making long illumination times (>1 s) necessary. This, in turn, led to the death of the cells after just 1 - 2 h and 6 - 12 images. Due to this fact, the fluorescence illumination time was drastically reduced allowing only cell localization. The REFs were barely visible in the brightfield images, but since the brightfield images were taken to track the pillar deflection, this fact was an advantage rather than a disadvantage. The less the cells disturbed the images of the pillars, the better for the tracking process.

In the actual experiments pillar fields with a center to center distance of 8 µm and usual sizes of 50 x $(a \cdot 50)$ pillars were used (with $1 < a < 10$; see subsection 3.4.1 for the fabrication process). Figure 4.4 a shows a cut-out composite image of such a pillar field 2 h after cell seeding. To facilitate the recognition of the REFs on the GPPP field the YFP image is overlaid in Figure 4.4 b (in this example, 60 cells were imaged).

The most important setting during the experiments was the adjustment of the right focus plane. It had to be such, that the pillars appeared as dark rings with a bright middle area, otherwise the tracking algorithms could not be applied. In long term experiments the objectives or the specimen tend to drift either in the x-y-plane, which can be easily corrected afterwards, or in the z-direction, that can only be tolerated to a very small extent. Figure 4.5 illustrates the right/usable and wrong/unusable focus planes of some pillars.

After a successful experiment the cells were detached from the GPPPs to calibrate the pillars described in section 3.5.

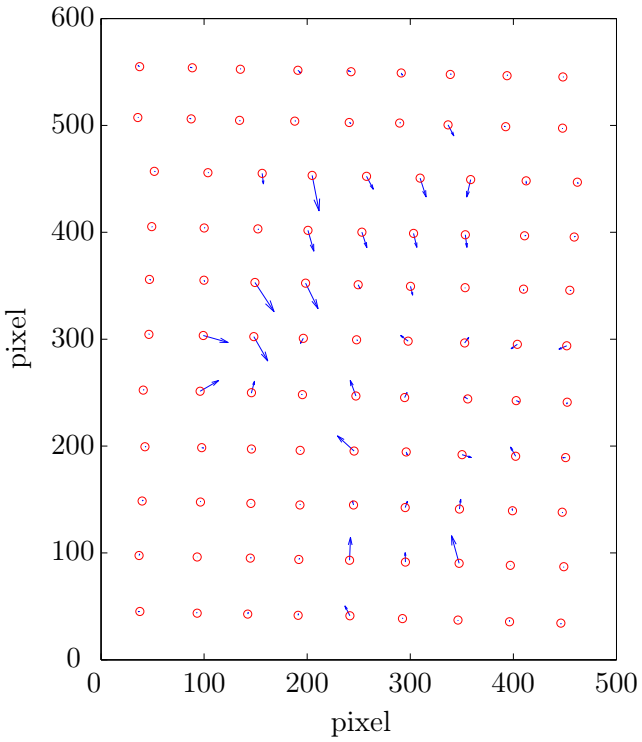

Figure 4.6: An example snapshot of the deflection pattern caused by one adherent cell on GPPPs. Is shows the "no force" positions of the pillars (red circles) and the deflection indicated as scaled up blue vectors. The imprecision in the pillar array was given by the used motor stage. Additionally, the shift of the upper two rows was caused by an external unexpected disturbance during the illumination process.

4.1.4 Pillar Tracking and Force Evaluation

The obtained brightfield image sequences of the cells were analyzed for their quality (e.g. correct focus plane) and then the software tracking of the pillars over the whole time frame was applied. Afterwards, different software algorithms were applied to correct for drifts and to obtain the "no force" position of each pillar (see section 3.9). With the drift corrected pillar positions and the determined "no force" coordinates the deflection for each pillar was evaluated. These deflections could then be visualized as vectors as shown in Figure 4.6. To assign forces to these pixel values, the spring constants of the pillars were measured and thus the active forces were calculated.

One main interest of these experiments and evaluations was to find out whether there is a difference in force generation of cells adhering to $\alpha_v\beta_3$- or $\alpha_5\beta_1$-integrin selective ligands. Therefore, the maximum force on each pillar, within the 5 h time frame after seeding, was identified. The obtained data is visualized in the histogram of Figure 4.7 a. It represents all maximum forces of approximately 6000 deflected pillars per ligand. Only pillars which experienced a force over 1 nN were included. For the normalization each histogram bar was divided by the total number of the bent pillars. To estimate the error two error sources were taken into account: the tracking error given by the tracking "fluctuations" of not bent pillars (see section 3.9) and the deviation in the calibrated spring constant (see section 3.5) . By adding and subtracting these errors to and from each maximum pillar force, an "upper-" and "lower-"

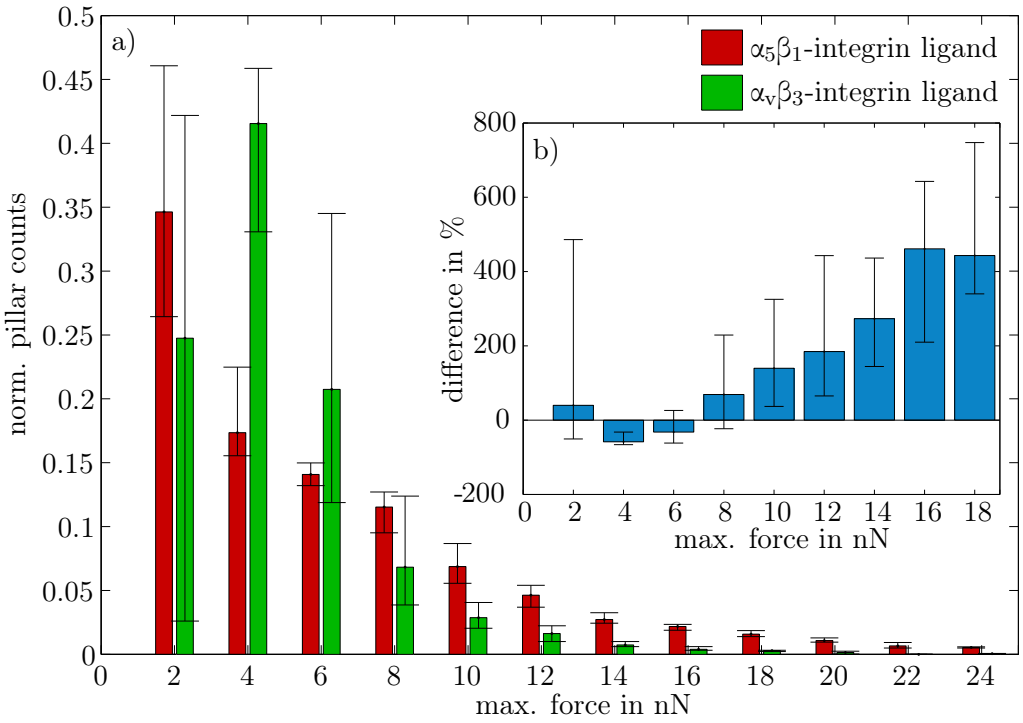

Figure 4.7: a) Normalized frequency histogram of the maximum cell traction forces observed on each pillar. The normalization was obtained by dividing each histogram bar by the total number of pillars analyzed for this diagram. b) Plot of differences between $\alpha_5\beta_1$- and $\alpha_v\beta_3$-integrin data sets shown in a) in percent. Both histograms demonstrate the trend, that cells adherent to GPPPs with the $\alpha_5\beta_1$-integrin selective ligand have a tendency to exert higher maximum forces on the pillars.

error histogram was plotted, which are included in Figure 4.7 a as the error bars. Additionally, Figure 4.7 b shows the relative difference between the data sets in percent, further highlighting the trends between the histograms observed in Figure 4.7 a.

A second method for the normalization of this histogram was the division by the cell number exerting these forces on the GPPPs. This normalization varied the force distributions only slightly ($< 5\%$), indicating that the histogram is not highly correlated with the number of cells which generated the forces.

An examination of the histograms quickly reveals a clear trend. At maximum forces under 7 nN there are considerably more counts on the $\alpha_v\beta_3$-integrin selectively functionalized GPPPs than on the $\alpha_5\beta_1$-integrin counterparts. But as soon as this maximum force value of 7 nN is exceeded there are much more counts for the $\alpha_5\beta_1$-integrin functionalized GPPPs. This means the cells seeded on the $\alpha_5\beta_1$-integrin selective ligand have a tendency and ability to exert higher maximum forces on the GPPPs than cells seeded on the $\alpha_v\beta_3$-integrin selective ligand.

The success of these long-term life cell experiments proved the capabilities of this newly established tool. With a tracking accuracy of approximately 50 nm, a force resolution of 0.75 nN

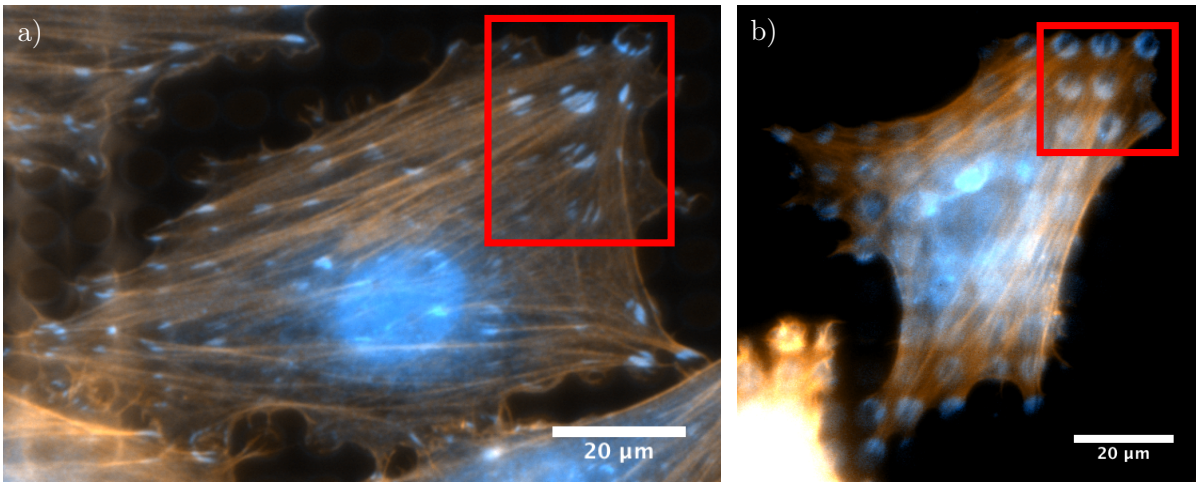

Figure 4.8: Fluorescence overlay images of two REFs on GPPP fields functionalized with a) $\alpha_5\beta_1$- and b) $\alpha_v\beta_3$-integrin selective peptidomimetics. The actin stress fibers (orange), as well as the zyxin (blue) were stained and visualized. Figure 4.9 shows a closer view on the areas in the red rectangles.

was achieved. Furthermore, a clear difference in the behavior of cells seeded on two different integrin selective ligands was also shown, which demonstrates the active functionalization and the applicability of the GPPPs for long term cell experiments ($> 5\,\mathrm{h}$).

A further discussion about possible biological explanations for the observed force differences, in context of the current literature, can be found in subsection 5.1.2 in the results and discussion chapter.

4.1.5 Zyxin, Actin and Paxillin Fluorescence Stainings

In the aforementioned force measurement experiments and evaluation, a significant shortcoming was the lack of conclusive information about differences in the cell behavior at the protein level. This was mainly due to the poor fluorescence of the YFP fused to the paxillin protein of the cells. To overcome this, and to analyze further the cell reactions on GPPPs functionalized with the $\alpha_v\beta_3$- or $\alpha_5\beta_1$-integrin selective ligand, fixation and fluorescence staining experiments were conducted.

Therefore, REFs were seeded for 5 h on GPPPs functionalized with either ligand, followed by the fixation and staining procedure specified in subsection 3.6.3. Thereby zyxin, actin and paxillin were fluorescently labeled. A second labeling of the paxillin was performed to enhance the poor fluorescence of the YFP.

Images of all three labeled proteins were acquired, merged and evaluated. Two example overlay pictures of one cell on GPPPs functionalized with either ligand can be seen in Figure 4.8. Closer views on the paxillin and zyxin distribution is shown in Figure 4.9.

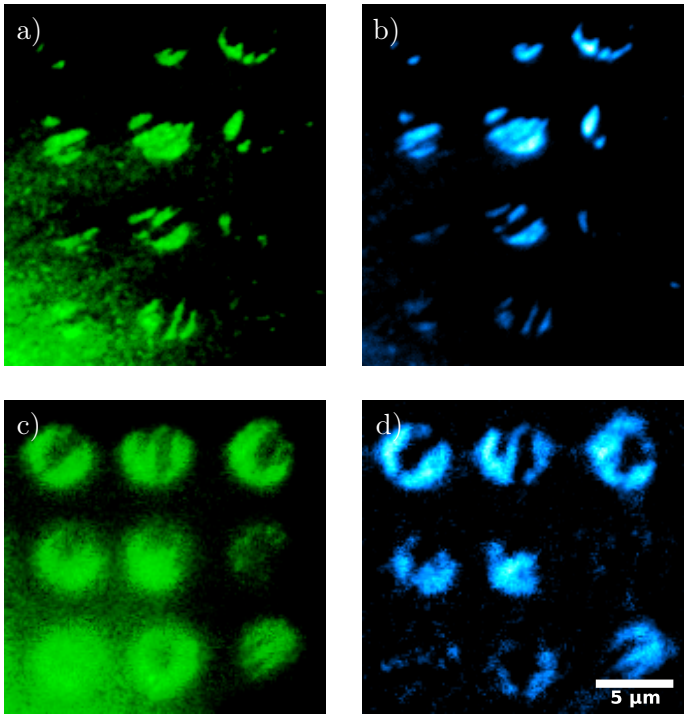

Figure 4.9: Magnified view on the paxillin a), c) and zyxin b), d) distributions of the red boxes in Figure 4.8. The images a) and b) show focal adhesions on the $\alpha_5\beta_1$-integrin ligand, in c) and d) they are binding to $\alpha_v\beta_3$-integrin selective ligands. All images clearly show focal adhesions only on the pillar tops.

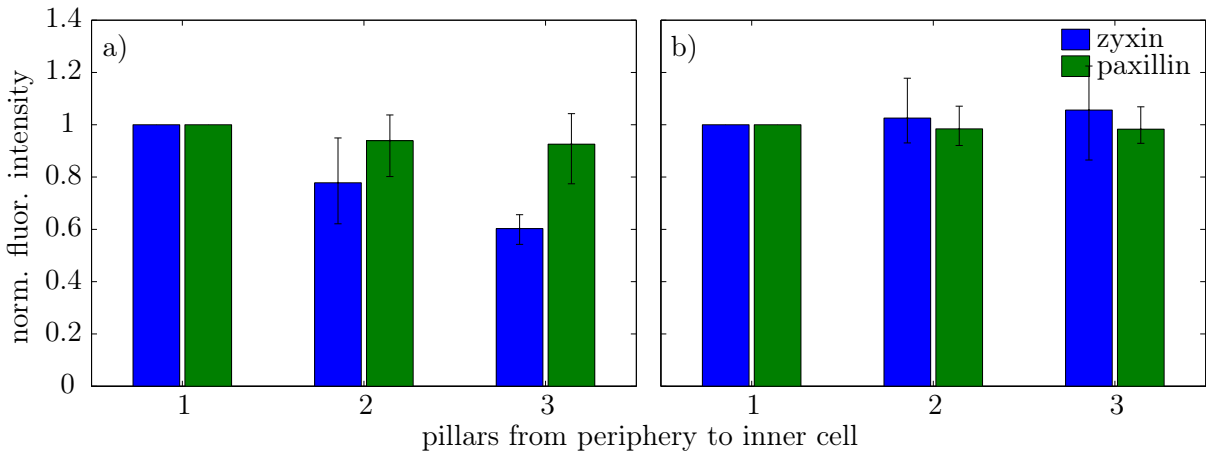

Figure 4.10: Normalized maximum zyxin and paxillin fluorescence intensity on three neighboring pillars. On the $\alpha_5\beta_1$-integrin selective ligand a) and the $\alpha_v\beta_3$-integrin selective ligand b). Pillars with contact to the outer cell boundary (1), to the inner cell region (3), or to the area in-between (2) were analyzed. The paxillin fluorescence on both ligands is constant within the errors. For zyxin there is a clear drop in the fluorescence intensity in the cells seeded on the $\alpha_5\beta_1$-integrin selective ligand a), compared to the cells on the $\alpha_v\beta_3$-integrin selective ligand b). In the latter the zyxin intensity is constant throughout the entire cell area.

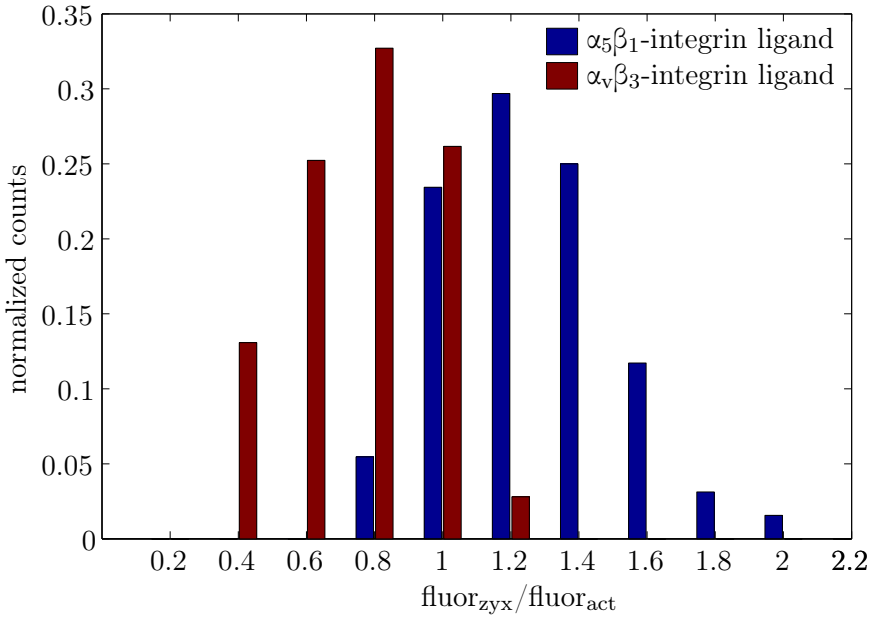

Figure 4.11: Normalized histogram of the zyxin : actin fluorescence intensity ratio on ligand-bearing pillars at the cell periphery. In cells attached to the $\alpha_5\beta_1$-integrin selective ligand the zyxin by actin fluorescence intensity ratio is higher than in cells bound to $\alpha_v\beta_3$-integrin ligand. This indicates that on the $\alpha_5\beta_1$-integrin coupled cells there was a higher zyxin per actin localization on peripheral focal adhesion sites. A two-tailed student's t-test revealed a significant difference between the two normal distributions with $p < 0.001$.

Observing the paxillin clusters immediately highlighted that the cells indeed formed focal adhesions just on the pillar tops. For comparison, the fluorescence intensities within the pillar areas were determined. This values correlate to the number of fluorophores and with it to the number of proteins of interest.

The maximum paxillin and zyxin intensity values (averaged over the 10 brightest pixels) on three neighboring pillars, from the periphery to the inner part of the cell, were compared and visualized in Figure 4.10. This intensity corresponds to the maximum local protein density on the pillar regions. They were normalized by setting the pillar intensity at the periphery as reference intensity to 1. The error bars represent the standard deviation of the normalized intensities. These normalized histograms show, on the one hand, that the paxillin intensity was unchanged (within the errors) on all three pillars and on both ligands. The zyxin intensity, on the other hand, drops from the outer to the inner part of the cells on the GPPPs functionalized with the $\alpha_5\beta_1$-integrin ligand, whereas it stays constant on the $\alpha_v\beta_3$-integrin ligand. That indicates a more homogenous distribution of zyxin at focal adhesions over the cell on the $\alpha_v\beta_3$-integrin ligand, and a higher peripheral localization of it on the $\alpha_5\beta_1$-integrin ligand.

The second comparison investigated the zyxin to actin fluorescence ratio. Therefore, the averaged fluorescence values on the pillar areas were evaluated, but this time only pillars at the

direct periphery of the cells were taken into account. After calculating the ratios for approx. 140 pillars on both ligands, the histogram seen in Figure 4.11 was plotted. It shows that the cells binding to the $\alpha_5\beta_1$-integrin ligand show a higher zyxin per actin density than cells on the $\alpha_v\beta_3$-integrin ligand. A two-tailed student's t-test revealed a significant difference between the two normal distributions ($p < 0.001$).

The evaluation of the fixation and staining experiments demonstrated that a different behavior of the REFs seeded on GPPP fields, functionalized with the integrin selective ligands, were not only observable in the force generation of the cells (shown in subsection 4.1.4), but also in their protein recruitment and clustering behavior. How these results can be brought into a biological and biophysical picture together with the force evaluations is discussed in the results and discussion chapter subsection 5.1.2.

4.2 Contractile Actin Network Experiments on PEG Pillars

For the investigation of the force generation caused by *in vitro* actin networks bundled with Mg^{2+}-ions, the established microbead functionalized PEG pillars had to be adapted to the requirements of the actin fibers and the expected forces in the sub-100 pN range. Theoretically, also GPPPs functionalized with streptavidin would allow the binding of biotinylated actin filament. However, even at the lowest possible gold nanoparticle spacing of 30 nm the streptavidin density and thus the available binding sites for the biotinylated actin filaments are significantly lower than on streptavidin coated microbeads. That made the GPPPs unfavorable for these actin experiments. The following sections outline the most important steps and experiments for these studies.

4.2.1 *In Vitro* Actin Network Formation on Microbead Functionalized PEG Pillars

The initial task was the construction of an environment that was closed, to minimize external influences and still offered the ability to control and exchange aqueous buffer solutions. Therefore, the microbead functionalized PEG pillars were implemented into microfluidic chambers composed of glass and PDMS. How this was achieved can be seen in Figure 3.15 and is described in subsection 3.8.2. A photo of such a chamber is shown in Figure 4.12.

First experiments were done to establish a preparation protocol for actin networks on PEG pillars. So far, *in vitro* actin networks on pillar substrates were formed on PDMS pillar structures functionalized with N-ethylmaleimide-modified heavy meromyosin (NEM-HMM) [94, 99]. This special myosin type has the ability to strongly bind to actin.

As described in subsection 3.8.2, at one end of the two tubings a 1 ml syringe was attached. To allow an exact control over the flow speeds, this syringe was integrated into a syringe

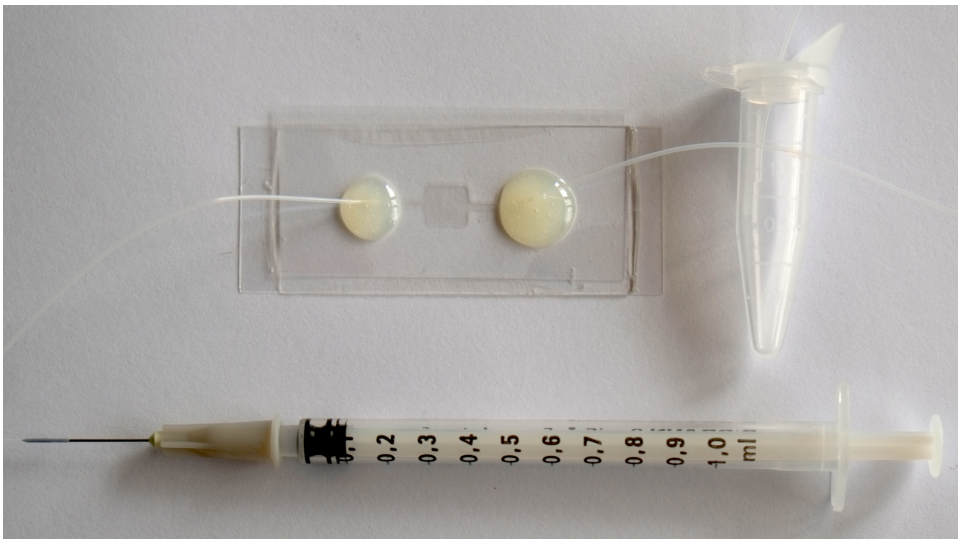

Figure 4.12: Photo of the microfluidic chamber with attached tubings. The microfluidic chamber had a base area of 6 mm x 6 mm and a height of 70 - 150 µm. At the one end the tubing is connected to a 1 ml syringe and the other is inserted into a reservoir of the experimentally needed buffer solution.

pump[2]. After the placement of the microfluidic chamber on the confocal microscope (LSM) it was checked for any fluid leakage by flushing it with t-buffer (see subsection 3.7.2) for 10 min at 10 µl/min. Then a dense filamentous actin solution (1 : 20 of the 5 µM stock filamentous actin solution to t-buffer) was drawn into the chamber at a flow rate of 2 µl/min until the bright fluorescence of the filaments was visible at the outlet of the microfluidic channels. In this state the whole chamber was flooded with a high density of actin filaments undergoing Brownian motion. For at least one hour the solution was incubated in the chamber. During this time, the biotinylated actin filaments bound to the streptavidin coated beads on the pillar tops. Following this incubation step a t-buffer solution was flushed into the chamber at a slow flow rate of 0.5 µl/min to prevent a rupturing of the coupled actin filaments and to get rid of unbound actin filaments. It took at least 2 h until most of the not coupled actin filaments were removed from the chamber. Figure 4.13 a shows a bead PEG pillar field after the actin filament incubation. Due to the slow illumination intervals of the confocal microscope and the Brownian motion of the actin filament, they appear blurry. Afterwards, the chamber was flooded with a 50 mM Mg^{2+} containing bundling t-buffer solution at a flow rate of 0.5 µl/min. As soon as the bundling solution reaches the actin filaments on the pillar field, they form a bundled network. Due to the attractive interactions between the filaments they form strained actin filament bundles. In this network configuration their Brownian motion is highly damped. This can be seen in Figure 4.13 b, where the formed actin bundles are clearly visible in contrast

[2]Pump 11 Pico Plus, Harvard Apparatus, USA

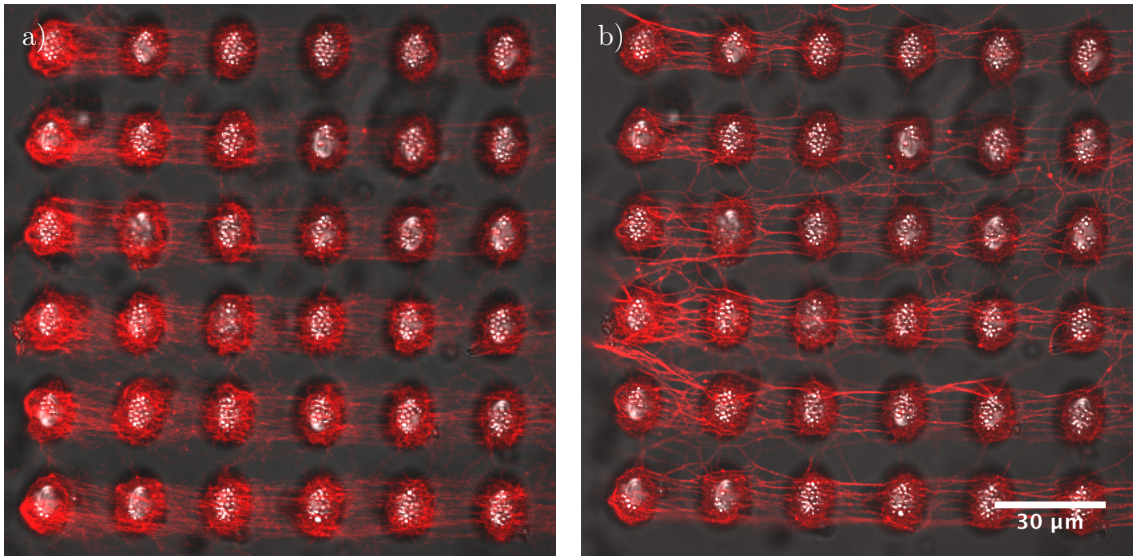

Figure 4.13: Two micrographs of biotinylated actin filaments (red) on a PEG pillar field functionalized with streptavidin coated beads. In a) the actin filaments are not bundled and due to their negative charge, the Brownian motion and the slow recording speed of the confocal microscope, the actin filaments repel each other and appear blurry. After flushing the microfluidic chamber with the 50 mM Mg^{2+}-ions containing t-buffer solution, the actin filaments bundle and form a network of multi-filament actin bundles b). In both cases an orientation of the filaments, due to the flow direction during the buffer exchange, is visible.

to the blurry uncoupled filaments in Figure 4.13 a. In both cases a preferential alignment of the actin fibers parallel to the flow direction is observable.

Since the purpose of these first experiments was to test the coupling of the actin network to the bead functionalized PEG pillars, and to facilitate the pillar fabrication, these pillars had diameters of up to 10 µm, a length of approximately 50 µm and a center to center spacing of 20 µm and more. Their spring constant was 10 $^{nN}/_{µm}$ and higher. The expected forces were in the piconewton range, that's why no bending was detectable in these experiments. Nevertheless, they proved to bind actin filaments to the PEG pillars and exchange the buffer solutions under controlled conditions.

4.2.2 *In Vitro* Actin Network Bundling by Mg^{2+} on Hexagonal Pillar Island Fields

All requirements for the application of the bead functionalized PEG pillars as force sensors in the actin network system were: a controllable environment, a strong binding of the actin filaments to the pillars, pillar array with a suitable spring constant of the pillars. The first two needs were already shown by the successful initial experiments described in subsection 4.2.1.

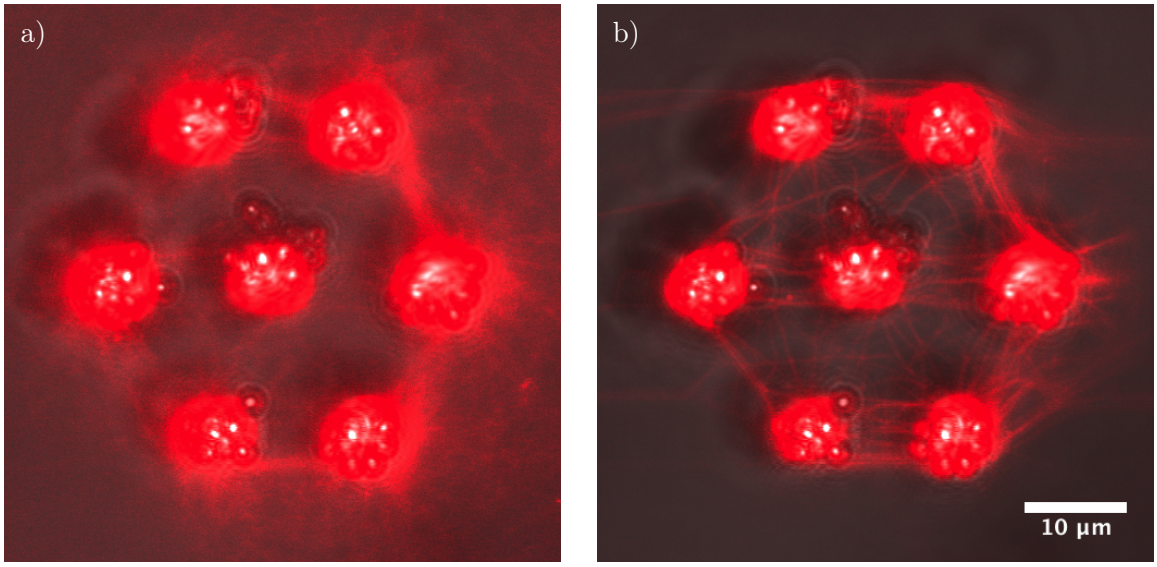

Figure 4.14: A hexagonal streptavidin bead functionalized PEG pillar array with attached biotinylated actin filaments (red) a) before and b) after Mg^{2+}-ion bundling buffer flush in. The forces generated by the bundling of the actin filaments did, for the outer pillars, not cancel each other out, as it was the case in a bigger array seen for example in Figure 4.13.

But they could not yet detect forces due to the disadvantageous pillar array and their too high spring constant.

Under the assumption of a perfect isotropic homogeneous actin network on a large pillar field, a contractile force would always be canceled out and only the pillars at the edge of the pillar field would experience a directed nonzero force. To overcome this fact, the concept of small pillar islands consisting of seven pillars in a hexagonal order was developed. They had a center to center distance of $15 \pm 1\,\mu m$, a length of $45 \pm 2\mu m$ and a diameter of $6 \pm 1.5\,\mu m$.

Following the same experimental procedure described in subsection 4.2.1 actin filament networks were formed on these hexagonal pillar configurations. To decrease the alignment of the actin filaments in flow direction a lower flow speed of 0.2 $\mu l/min$, for the flushing out process of the unbound actin filaments, was chosen. An example of such a hexagonal pillar island can be seen in Figure 4.14.

For the experiments pillar field consisting of 25 or more of this hexagonal PEG pillar islands were illuminated. Due to the configuration all six outer pillars could be directly calibrated as described in section 3.5.

The first experiments on the hexagonal PEG pillar islands revealed an additional difficulty. Even without any actin filaments on the pillars, the exchange of the different buffers (e.g. t-buffer to t-buffer with Mg^{2+}-ions) a movement of the pillar tops of up to $0.5\,\mu m$ was detectable. This movement happened due to the different ion concentrations of the buffers and the random

orientation of the PEG molecule chains within the PEG hydrogel pillars leading to anisotropic expansion or contraction reactions within the PEG pillars. This effect was reproducible and by following the work flow described in the next section, the tension forces could be calculated despite this pillar bending effects.

4.2.3 Tracking and Force Evaluation

The actual actin network bundling experiments had the following cycle and were all monitored at 8 fps on a standard brightfield microscope configuration:

1. Binding of unbundled actin fibers to the pillar tops as described in subsection 4.2.2.

2. Flush in of t-buffer with 50 mM Mg^{2+}-ion concentration leading to a bundling and contraction of the actin networks and to a bending of the pillars. Additionally, the pillars bent due to the change in ion concentration of the surrounding buffer.

3. Flush in of Milli-Q water, which destroys the actin filaments within seconds after the water diluted the t-buffer to a critical value. This sudden release of the tension caused by the bundled actin filaments is observable in a sudden jump of the pillar positions to the outer direction of the hexagons (see Figure 4.15). Again, the changing ion concentration also resulted in a bending of the pillars as can be seen in Figure 4.16.

4. Flush in of t-buffer, to restore the original ionic- and experimental state within the microfluidic chamber.

The whole process was then repeated with no actin filaments on the pillars.

As described before even without actin filaments on the pillars a bending and with it a movement of the beads on the pillars was observed induced by the buffer exchange. This fact made it impossible to distinguish between the pillar bending caused by the bundling actin filaments and the bending generated by the change in ion concentration, during the influx of the bundling buffer into the chamber (step 2. of the experimental cycle). The quick release (within seconds) of the built up forces due to the destruction of the contracted actin network (step 3.), however, was monitored independently of the bending effects happening in longer time frames (several minutes). This jump is illustrated in Figure 4.15 where on each pillar at least one bead was tracked over the whole time of the Milli-Q water influx. The tracking curves only show the jump time frame of approximately 10 s. All pillars, except the middle one, moved outwards, as expected.

Since no fluorescence images could be made during these experiments, the rupturing of the bundled actin was not monitored directly. To prove that the observed jump of the bead positions was indeed due to the destruction of the bundled actin filaments and not an effect caused by

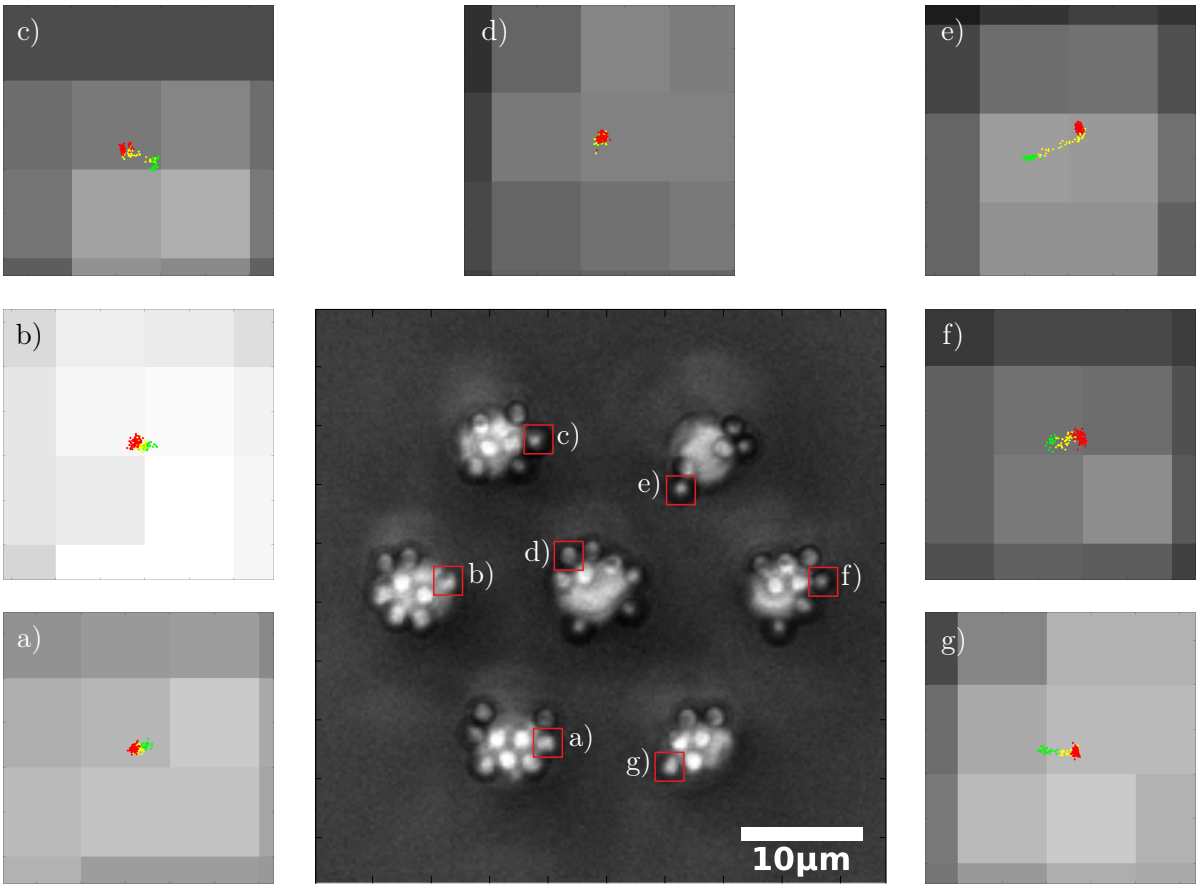

Figure 4.15: Microscopy image of a bead functionalized PEG pillar hexagon, during the actin network "destruction" step (200 frames $\widehat{=}$ 25 s). The bundled and thus contracted actin network on the pillars is degraded by the exchange of the t-buffer with Milli-Q water. At a critical dilution of the t-buffer the actin filaments break and tension of the network is released. This jump is illustrated by the tracking coordinates of the marked (red squares) beads on the pillars. All six outer pillars showed an outwards movement (from green over yellow to red), but different magnitudes.

the buffer exchange, the pillar trajectories of both experimental cycles (with and without actin) were directly compared. An example for such a trajectory comparison with (green) and without (red) actin filaments during the influx of the Milli-Q water (step 3.) is visualized in Figure 4.16. It shows the position of the bead in the red square e) in Figure 4.15. The first parts of the trajectories were almost identical, then the influence of the bundled actin network tension forced the pillar on another trajectory (green) than without actin filaments (red). At a certain dilution of the buffer solution the actin filaments rupture and release the tension, observable in a jump in the trajectory (yellow arrow). Both trajectories ended, as expected, at the same position. This effect was observed on all six pillars of this hexagon and also in other separate experiments.

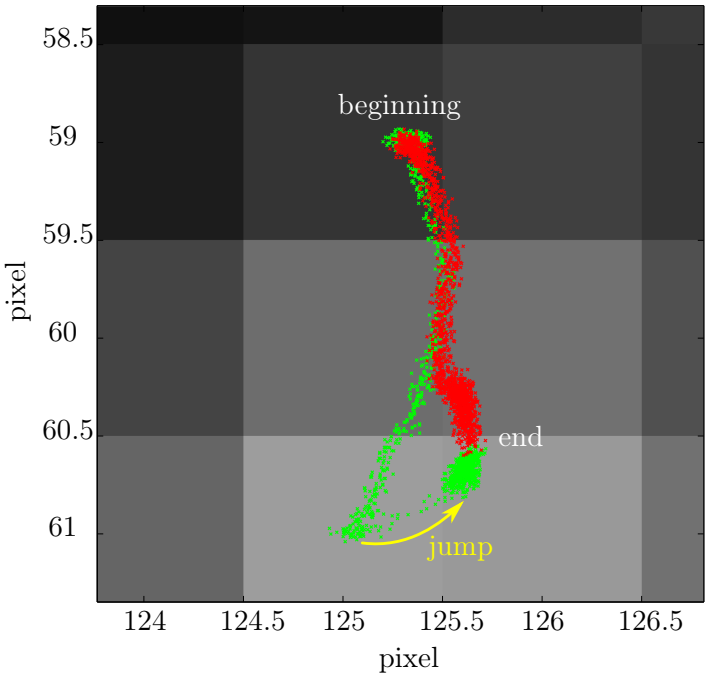

Figure 4.16: Zoomed in view on two trajectories of the bead e) of Figure 4.15. The red trajectory follows the bead movement caused by the pillar bending induced by the buffer solution change from the bundling t-buffer, with 50 mM Mg^{2+}-ions, to Milli-Q water without attached actin filaments (time frame $\approx$ 3 min). In green the trajectory shows the path of the same bead under the same buffer conditions, but with an attached and bundled actin network on the pillars. First both trajectories are almost the same, but then the influence of the bundled actin network is clearly visible. At a certain point, the critical dilution of the t-buffer is met, and the actin filaments degraded within seconds leading to a release of the tension and a jump (yellow arrow) in the bead position to approximately the same end position as the red trajectory.

The forces or the tension caused by the bundled actin filaments on each pillar could then be calculated by multiplying the deflection (jump) with the spring-constant of each pillar. But, as can be seen in the example of Figure 4.15 the jumps had very different magnitudes, despite the pillars having approximately the same spring constants. Regardless of this behavior, 60 pillars were tracked, calibrated and the release forces during the jump were calculated and plotted in a histogram shown in Figure 4.17. The resulted forces were between 10 and 130 pN and randomly distributed, with no distinguishable mean peak value.

This random distribution can be explained by two experimental factors. Due to the self assembly process used in both the construction of the particle arrays on the PEG pillars and the actin networks, the end networks had an inhomogeneous, random structure. But, to receive reproducible force data it would be necessary to have homogeneously and isotropically organized actin filaments on the pillars.

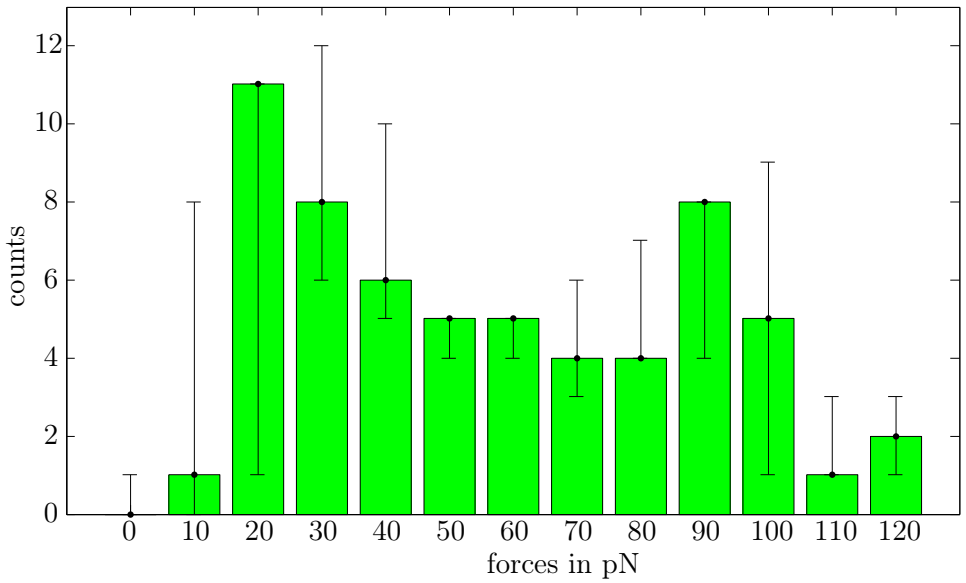

Figure 4.17: A histogram of the force data obtained by the analysis of the tension release jumps on the PEG pillar hexagons. 60 pillars were evaluated, showing a random distribution with no clear mean peak. The errors were calculated by adding and subtracting the tracking and spring constant error to and from the calculated force data. These values were then plotted with the same histogram bins, the differences between these error histograms and the force histogram then yield the error bars shown here.

To test whether the Mg^{2+}-ion concentration has a significant impact on the observable forces, experiments with a ion concentration of 25 mM instead of the usual 50 mM were performed. Here just 24 pillars were evaluated, showing a similar random distribution between 10 and 100 pN. This suggested, that the actin distribution has a bigger influence on the forces than the ion concentration in the buffer solution. These facts made further investigations of the ion concentration dependence of the contractile forces unfeasible.

However, the high sensitivity pillars were suitable for the measurement of forces below 100 pN with a resolution of up to 9 ± 2 pN. The results of the actin filament bundling experiments on PEG pillar functionalized with surface coated microspheres are summarized and discussed in section 5.2 of the results and discussion chapter.

Chapter 5

Results and Discussion

In this chapter, all the main findings of the successfully performed and evaluated experiments described in chapter 4 are presented, discussed and brought into context with the current literature.

5.1 Integrin Selective Cellular Traction Forces on GPPP Fields

The aim of these experiments was the development and application of a new type of traction force measurement tool based on gold nanoparticle decorated PEG pillars. Both the development and the application were successfully demonstrated in section 4.1.

5.1.1 General Properties of the GPPPs

The performed fabrication, calibration and characterization experiments described in section 4.1 showed the efficient combination of the PEG pillar fabrication and the transfer of gold nanoparticles to hydrogels. One of the most beneficial feature of this approach was the flexibility to tune several parameters, which allow the adjustment of the pillars to the experimentally favorable dimension an offered the control over their stiffness and gold nanoparticle spacing. Summarized, the experimentally shown characteristics of the GPPPs are the following:

- **Geometry:** The pillars were cylindric with a diameter of 2 µm or more and had an aspect ratio of up to 1 : 10. The closest achieved center to center inter-pillar spacing was 5 µm.
- **Spring constants:** Dependent on the chain length of the used PEG and the geometry of the pillars, spring constants between 0.35 and 100 $^{\mathrm{nN}}/_{\mu\mathrm{m}}$ were produced and calibrated. Combined with a tracking accuracy of 50 nm (see subsection 3.9.1) they allow force resolutions between 18 pN and 5 nN.

- **Gold nanoparticle structures:** All obtainable spacing by BCML between 30 and 300 nm were also transferable to the PEG pillars without significant changes in their order parameter or spacing.
- **Functionalization:** Analog to gold nanoparticle structured glass surfaces also the gold nanoparticles on the PEG pillars could be functionalized by coupling bioactive compounds via a thiol linker to the gold nanoparticles. This was shown for cRGD, and $\alpha_v\beta_3$- and $\alpha_5\beta_1$-integrin selective peptidomimetics.

As outlined in the introduction (chapter 1) the most commonly used traction force evaluation tools are micropillar fields made out of PDMS [28, 139, 157]. They offer by far not the same versatility than the GPPPs. Their main shortcoming is the non covalently bound ligand applied by microcontact printing or simple incubation, offering just little control over the ligand density. It was also shown, that these physisorption based functionalizations are dependent on the PDMS rigidity [148]. Furthermore, the gold nano particles allow to control inter-ligand spacing, which other coating techniques cannot provide. These spacing are known to have dramatic influence on cellular adhesion formation [5, 15, 59, 147].

There are more sophisticated fabrication methods using direct laser writing techniques, allowing the construction of 3D PEG structures [48, 68, 69]. However, they require highly specialized and complex machinery for their production and do not provide the same functionalization potentials offered by the GPPPs.

New tools have to prove their applicability. Therefore, the characterization of the GPPPs alone was the first step, the next was the application in cell adhesion and traction force experiments. To do so, the GPPPs were tuned to the desired geometrical and physical properties for the formation of mature focal adhesions on the pillar tops to allow the spreading and motility of REFs. These properties were:

diameter	**length**	**spacing (ctc)**	**spring constant**	**nanoparticle spacing**
$3.5 \pm 0.5\,\mu m$	$13 \pm 1\,\mu m$	$8 \pm 1\,\mu m$	$15 \pm 2\,^{nN}/_{\mu m}$	$55 \pm 5\,nm$

The functionalization with thiolated cRGD and the spreading of REFs on GPPPs with these properties showed their applicability as substrate for cellular adhesion studies. Deflection of the pillars, allowing conclusions on the forces applied by cells, were also observed. These results paved the way for the next experiments, the determination of the differences in adhesion and force generation capabilities of REFs adhering to $\alpha_v\beta_3$- or $\alpha_5\beta_1$-integrin selective ligands.

5.1.2 Cellular Adhesion and Traction Force Generation in Dependence on $\alpha_v\beta_3$- and $\alpha_5\beta_1$-Integrin Selective Ligands

The functionalization of the GPPPs with specific integrin selective peptidomimetics [127] offered the possibility to investigate the adhesion and force generation behavior of REFs seeded on

them. Time lapse, as well as fixing and staining experiments gave new insights in the highly discussed field of cell adhesion and the contribution of the two different integrins.

The evaluation of the time lapse traction force experiments of REFs cells either seeded on the $\alpha_v\beta_3$- or $\alpha_5\beta_1$-integrin selective ligand revealed a clear difference in the force generation capabilities. As shown in the histograms of Figure 4.7, the cells on the $\alpha_5\beta_1$-integrin ligand have the tendency and capability to exert higher maximum forces than cells on the $\alpha_v\beta_3$-integrin ligand.

This result corresponds very well to the experimental findings of P. Roca-Cusachs et al. [131]. They measured the interaction of mouse embryonic fibroblasts (MEFs) with either vitronectin or fibronectin-coated beads by pulling on them with magnetic tweezers. Since $\alpha_5\beta_1$-integrin cannot bind to vitronectin, they could distinguish the differences in adhesion strength of MEFs attached to the beads via the $\alpha_v\beta_3$- or $\alpha_5\beta_1$-integrins. The adhesion strength of $\alpha_5\beta_1$-integrins was significantly higher than of $\alpha_v\beta_3$-integrins. Furthermore, very recent work of G. L. Lin [82] showed that the activation of β_1 but not β_3-integrins led to an increase of traction forces. They seeded wild type MEFs and β_1-integrin knockout MEFs on PDMS pillar fields coated with fibronectin. In both cases they activated the integrins by the addition of manganese-ions (Mn^{2+}) and saw an increase in the traction forces for the wild type MEFs but not for the β_1-integrin knockout MEFs. In the here presented experiments only $\alpha_v\beta_3$- or the $\alpha_5\beta_1$-integrins were able to form adhesions on the GPPPs, which meant that only the activated integrins of these subtypes mainly contributed to the observed adhesion and traction forces. These facts imply that the findings of G. L. Lin et al. are also in agreement with the here depicted integrin selective traction force results on the GPPP fields.

However, the overall maximum forces measured on both ligands showed similarities to the maximum forces observed by L. Trichet et al. [158]. In their experiments of REFs on fibronectin coated PDMS pillar fields they found a correlation between the maximum forces the REFs could apply on a pillar and its stiffness. Independent of the pillar spring constant they observed a maximum deflection of $0.84 \pm 0.03\,\mu m$. This meant the expected total maximum forces for the experiments on the GPPP arrays should be in the range of 13 to 17 nN. As can be seen in Figure 4.7 most maximum forces were below this force region, but in very few instances there were also higher forces of up to 27 nN measured. These forces correspond to deflections of approximately 1.8 µm, which is significantly higher than the 0.84 µm L. Trichet et al. have observed. One reason for that could be the fact, that the PDMS pillars used by them had a diameter of 2 µm or less which is smaller than the average size of a mature focal adhesion, whereas the GPPPs had a diameter of $3.5 \pm 0.5\,\mu m$ and thus offered more area for the focal adhesions to interact with the surface. The means of all measured maximum deflections on the GPPP fields were $0.43 \pm 0.15\,\mu m$ on the $\alpha_5\beta_1$-integrin ligand and $0.31 \pm 0.14\,\mu m$, which is comparable to the $0.84 \pm 0.03\,\mu m$ found by L. Trichet et al..

In oder to gain insight into the biophysical processes resulting in the observed traction forces,

the protein composition of the focal adhesions was investigated. Therefore, fixed REFs adherent on the functionalized GPPP fields were stained for zyxin, paxillin and actin and were analyzed in two ways. The first way compared the maximum zyxin and paxillin fluorescence of the focal adhesions on three neighboring pillars from the edge to the inner part of the cell. This value corresponds to the highest protein densities on the pillars. Two histograms of the normalized obtained intensities for both ligands on the three pillars are shown in Figure 4.10. On both ligands the normalized intensity of paxillin was constant (within the error) on all three pillars. Also, on the $\alpha_v\beta_3$-integrin ligand, the zyxin intensity was constant over the analyzed pillar rows. Only on the $\alpha_5\beta_1$-integrin ligand a drop of the normalized zyxin intensity from the pillar located at edge to the ones at the inner part of the cells, was observed. Zyxin localization correlates with the acting forces [19, 56, 106, 171]. This drop in the intensity indicates a higher localization of the zyxin at the cell periphery on the $\alpha_5\beta_1$-integrin ligand, whereas on the $\alpha_v\beta_3$-integrin ligand the zyxin is homogeneously distributed over the cell. A higher zyxin concentration at the focal adhesions at the rim of the cells resembled a higher force concentration and thus higher maximum forces. The homogeneous distribution of the zyxin implies a more evenly distributed force thereby suggesting more lower maximum forces. These findings are well in line with the results of the force evaluations, where more high maximum force counts could be observed on the $\alpha_5\beta_1$-integrin ligand, and more lower maximum force counts were distinguished on the $\alpha_v\beta_3$-integrin ligand.

To further investigate the variations in the protein recruitment on the two ligands the mean fluorescence intensity of actin and zyxin on peripheral GPPPs was determined. These values correlated with the overall protein number on the pillar top area. The ratio of the zyxin to actin mean fluorescence values were then calculated and visualized in the histogram of Figure 4.11. Both his histograms are normally distributed shown by the Lilliefors-test. Furthermore, a two tailed student's t-test revealed that the two normal distributions differ significantly from one another (p-value < 0.001). In consequence, on the $\alpha_5\beta_1$-integrin ligand, whose mean ratio distribution was higher than the one of the $\alpha_v\beta_3$-integrin ligand, the cells recruited more zyxin per actin at their peripheral focal adhesions. More zyxin, as aforementioned, indicates an increased tension or force. This consideration, again, suggested that higher forces are exerted by the cells on peripheral pillars on the GPPPs functionalized with the $\alpha_5\beta_1$-integrin ligand.

Both protein comparison analyses further support the force generation behavior findings, that also others have reported [82, 131]. Additional suggestions in the same direction were made by M. R. Morgan et al. concerning their intracellular cell signaling observations [100]. Here, changes in the integrin composition of focal complexes trigger changes in the intracellular signaling that regulate the adhesion maturation process. In the extreme cases presented here, where only one integrin type can bind and contribute to the adhesion formation, that would mean two possible signaling extremes. Either a RhoA-dominated GTPase signaling on the $\alpha_5\beta_1$-integrin ligand causing higher cytoskeletal tension, or on the $\alpha_v\beta_3$-integrin ligand a Roc1-

dominant signaling, which drives the formation of focal complexes. These signaling events would also influence the recruitment and clustering of proteins like zyxin and actin in a way it was monitored in the presented fixing and staining experiments of the cells. Their conclusions support both the outcomes of the protein fluorescence analyses, and the force generation results of this work.

5.2 Force Generation of Contractile Actin Networks on Microbead Functionalized PEG Pillars

One of the many advantages of the PEG pillars compared to other pillar systems are the ability to tune their stiffness and with it their spring constant in a very broad range. Microbead functionalized PEG pillars with the spring constants of $0.35 \pm 0.08\,^{\mathrm{nN}}/_{\mu\mathrm{m}}$ depict, with a tracking accuracy of 25 nm (see subsection 3.9.1), a force resolution of 9 ± 2 pN. Even softer pillars were produced but could not be calibrated, because of the difficulties using the very fragile cantilevers necessary for their calibration.

The basic technique of the microbead functionalized PEG pillar construction was based on the work of A. Lindner. and B. Rühle [83, 135] for the study of the forces generated by mitotic spindles during mitosis. To allow the formation of actin filament networks on these PEG pillars several modifications and enhancements were necessary. First, a microfluidic environment was constructed, providing the ability to exchange the buffer solutions in a controlled manner. Second, the general possibility of attaching biotinylated actin filaments to the streptavidin coated microbeads on the PEG pillars was tested by generating pillar fields and incubate dense biotinylated actin filament solutions on them. Third, interpillar distances were reduced to 15 ± 1 µm and the geometry to diameters of 6.0 ± 1.5 µm and lengths of 45 ± 2 µm. Fourth, pillar spring constants were adjusted to be under $0.5\,^{\mathrm{nN}}/_{\mu\mathrm{m}}$. Fifth, the pillar arrays were optimized for the observation of the contractile forces to hexagonal arrays. All these steps were successfully achieved, allowing the application of the PEG pillars as force sensors in force regions under 100 pN.

Forces generated by the bundling of actin filaments were the subject of different studies from the single filament to network level. Two filaments bundled by Mg^{2+}-ions were able to exert a maximum force of around 0.2 pN. M. Streichfuss et al. [155] measured this by monitoring the displacement of microspheres attached to the filaments and held by optical tweezers. They found out, that the bundling force scales with the Mg^{2+}-ion concentration. In an earlier experiment by K. Uhrig et al. [159] an actin network on a hexagonal array of microspheres trapped in optical tweezers was also bundled by Mg^{2+}-ions. Here, forces of up to 3 pN were observed. Based on this idea the system was scaled up by the utilization of the microparticle functionalized PEG pillar with high sensitivities of $\leq 0.5\,^{\mathrm{nN}}/_{\mu\mathrm{m}}$. It could be shown that the forces generated

by the contraction of these hexagonal actin networks bundled by Mg^{2+}-ions were between 10 and 120 pN. Under the assumption, that also in this network the bundling force between two filaments was 0.2 pN, several hundred of them were involved in the generation of the forces of 50 pN and higher. The measured contraction forces had a broad distribution which stemmed from the random organization of the actin filaments on the pillars before the Mg^{2+}-ion solution was flushed in. This random organization also led to the random distribution of the received contraction forces where no clear mean force was distinguishable from the received histogram shown in Figure 4.17. The experimental conditions did not allow correlation between the actin filament distribution with the measured forces. Furthermore, a variation of the Mg^{2+}-ion concentration in the bundling buffer had no significant impact on the received forces on the pillars, which led to the conclusion, that the actin filament distribution and density before the bundling had a much higher impact on the measured forces than the ion concentration. The not precisely enough controllable filament density and arrangement on the pillars led to the broad distribution of received bundling forces.

Nevertheless, the experiments showed a successful formation of actin filament networks on the PEG pillars functionalized with surface coated microspheres. In contrast to the already established techniques for the formation of actin networks on PDMS substrates [99, 133] the low spring constant of under 0.5 $^{\mathrm{nN}}/_{\mu\mathrm{m}}$ together with a modified pillar array made the measurement of contractile forces between 10 and 120 pN possible, proving the applicability of the PEG pillars as highly sensitive force sensors in force regions of under 100 pN with a resolution of 9 ± 2 pN.

Chapter 6

Conclusion and Outlook

The main focus of this thesis was the development and application of functionalized PEG micropillar fields as force sensor arrays in biological systems.

These micropillars had three main tunable parameters: elasticity, geometry, and type of functionalization on the pillar tops. By setting these parameters appropriately PEG pillars with the following characteristics were produced: spring constants between 0.35 and 100 $^{nN}/_{\mu m}$ (or higher), diameters of 2 to 20 µm with lengths corresponding to an aspect ratio of 1 : 10 and pillar array center-to-center distances $\geq$ 5 µm. The functionalization was either achieved by attaching surface coated microbeads or by coupling thiolated molecules to (quasi) hexagonal gold nanoparticle structures on the pillar tops. For the latter, the transfer of gold nanoparticles to PEG hydrogels and the PEG pillar fabrication was successfully combined, thereby allowing gold nanoparticle spacing of 30 - 300 nm on the pillar tops.

For the application as cell traction force sensor arrays, these parameters were set to obtain PEG pillars with diameters of 3.5 ± 0.5 µm, lengths of 13 ± 1 µm, center-to-center distances of 8 ± 1 µm, spring constants of 15 ± 2 $^{nN}/_{\mu m}$ and gold nanoparticle spacing of 55 ± 5 nm. Rat embryonic fibroblasts adhered and spread on these pillars functionalized with cRGD, $\alpha_v\beta_3$- or $\alpha_5\beta_1$-integrin selective ligands.

Live cell experiments (carried out for up to 12 h) of REFs on GPPPs functionalized with either the $\alpha_v\beta_3$- or $\alpha_5\beta_1$-integrin selective ligand were performed. Traction forces as well as focal adhesion proteins zyxin, paxillin and actin were analyzed. The evaluations of traction force experiments demonstrated a difference in the force generation. Cells seeded on the $\alpha_5\beta_1$-integrin selective ligand had a tendency to exert higher maximum forces on the GPPPs than cells on the $\alpha_v\beta_3$-integrin selective ligand. Both observed differences in the protein clustering behavior supported the findings of the force evaluations. The force and the protein recruitment results are in good agreement with the reported findings of other groups in the field of integrin dependent adhesion studies.

To demonstrate the applicability of PEG pillars in force ranges below 100 pN, highly sensitive

(spring constant $\leq 0.5\,^{\mathrm{nN}}/_{\mu\mathrm{m}}$) PEG pillars functionalized with streptavidin coated microbeads were fabricated in hexagonal coordinated islands. On these pillars, networks of biotinylated actin filaments were constructed. By bundling the filaments with a Mg^{2+}-ion solution, the networks contracted. This contraction led to forces between 10 and 120 pN, measured with a force resolution of 9 ± 2 pN.

With the employment of the PEG pillar fields for cell adhesion studies and the force measurement of bundling actin networks, their beneficial applicability was successfully demonstrated. The inherent advantages of the GPPP compared to the widely used PDMS pillar arrays are: their more variable Young's modulus, their protein repellent nature and their functionalization possibilities. All these advantages make them a versatile new tool for force measurements in biological systems.

The presented thesis showed that PEG pillar arrays are able to provide new insights into the cellular adhesion processes and allow the investigation of biophysical forces in the subnanonewton regime.

Future cell adhesion experiments can be done by using other ligands or by taking advantage of the parameters that were not varied for the experiments shown in this thesis. For example, changing the gold nanoparticle spacing to study the effect on adhesion and traction forces. Other possible experiments can bring more insight into the question, whether a small local part of the cell is sensing the substrate rigidity or whether larger scaled interactions within the cell are necessary. This can be investigated by changing the Young's moduli of the pillars while adjusting the geometry such, that the spring constants of the pillars remain unchanged. Cells reacting to the different Young's moduli of these pillars would indicate a small rigidity sensing mechanism measuring the local pillar elasticity. However, if cells behave in a similar way on both pillar types, it would suggest that the cells use a larger scaled force measurement interaction determining only the overall spring constants of the pillars. These are just a fraction of the manifolded possible continuative biophysical experiments enabled by the PEG micropillar systems.

Appendix

Actin Networks on PEG Pillar Fields Bundled with α-Actinin

In all experiments shown in section 4.2 the actin filaments were bundled by Mg^{2+}-ions. In addition, experiments with the actin binding protein α-actinin were performed. These experiments were conducted similar to the actin filament experiments described in subsection 4.2.1 with only two differences. First, the bundling agent was a solution of α-actinin[1] in t-buffer ($c = 0.2\,\mathrm{mg/ml}$) and second, the actin filaments were directly polymerized in the microfluidic chamber. The so-called "in situ" polymerization had the advantage to lead to more homogenous networks, but, as can be seen in the Figure 6.1, the pillars showed a very high fluorescence due to many small submicrometer actin filaments coupled to the pillars. After the formation of the unbundled actin filament network on the PEG pillars the α-actinin bundling solution was flushed in with a flow rate of $0.15\,\mu\mathrm{l/min}$ for 3 h. In contrast to the Mg^{2+}-ion bundling solution, where the whole actin network was bundled within seconds, the bundling process with α-actinin took at least 2 h. Approximately one hour after the chamber was flooded with the bundling solution, the first bundling signs were visible (Figure 6.1 b). After approximately 1 h more the actin filaments were fully bundled (Figure 6.1 c).

Compared to actin networks bundled by Mg^{2+}-ion the structure was qualitatively different. In that case (Figure 6.1 d) nearly all bundles were straight and tightened, whereas the α-actinin bundled actin network had many curved bundles (Figure 6.1 c). Furthermore, there seemed to be more thick α-actinin actin filament bundles and hardly any thin ones. This latter observation could be caused by the too low resolution and high background of the images, in which case the curved bundles were held together by smaller, not resolved filaments and bundles leading to the observed structures.

O. Pelletier et al. saw in their experiments similar structural differences between 3D-actin networks bundled with counterion solutions (like Mg^{2+}) or α-actinin [115]. They observe a typical mesh size in order of the persistence length (here, approximately 16 µm) of the actin filaments bundled with α-actinin. Due to their preparation procedure (which involved centrifuging), the fragile smaller bundles were destroyed, leaving only the thicker more robust structures for their observations.

In the two single filament experiments of M. Streichfuss [154], no bundling was observed by α-actinin within the time frame of 5 min. This indicated that there is a significant difference in the bundle formation kinetics and process between Mg^{2+}-ions and α-actinin.

The fundamental difference between the two bundling mediating agents is their size and type. On the one side, there is the magnesium ion with an atom radius of about 150 pm, on the other the much bigger α-actinin protein with a length of approximately 35 nm. Why the counterion

[1] AT01, Cytoskeleton, USA

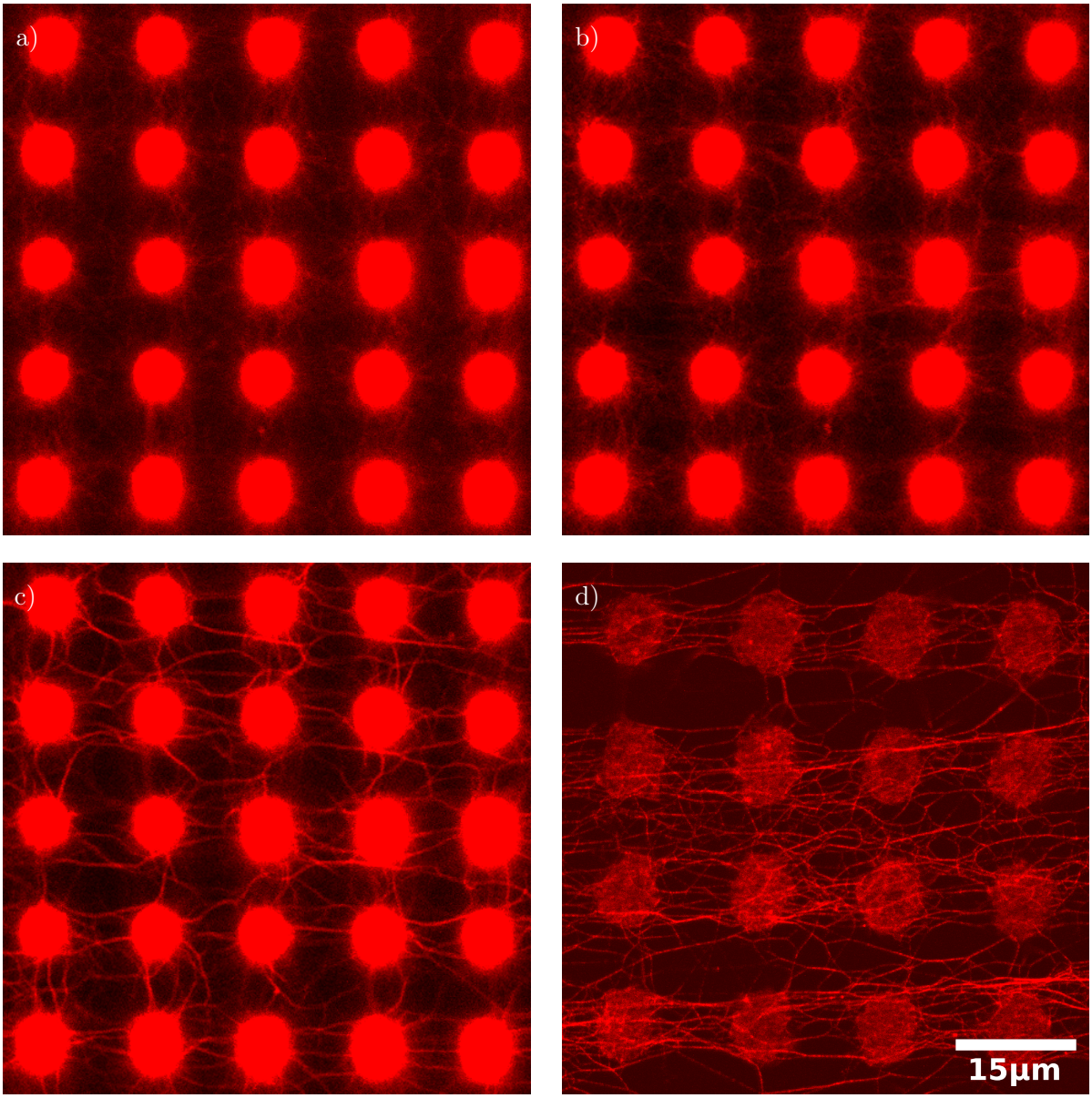

Figure 6.1: Fluorescence images of actin filaments on PEG micropillar arrays. The first three images show the time point during the bundling of the actin filaments with α-actinin, from a) the unbundled case to b) the beginning of the bundle formation after approximately 1 h after the flow in of the α-actinin solution to c) highly bundled actin filaments 1 h later. For comparison a actin network bundled by Mg^{2+}-ions is shown in d). Due to the polymerization in the microfluidic chamber much more sub micron filaments coupled to the pillar heads in a) - c) leading to a higher fluorescence of the pillars than in d) where the already polymerized actin filaments were flushed into the chamber. The scale bar is valid for all images.

induced bundle formation is so much faster than the bundling induced by α-actinin could be explained by the involved binding probabilities. α-actinin interacts with actin filaments only at its specific binding site. Two steps are required for a successful binding between two actin filaments with α-actinin: the α-actinin has to couple to one actin filament and another actin filament has to come close to the available end of the α-actinin with one of its unoccupied α-actinin binding sites. Both steps have a much lower probability than the counterion interaction mediated by the Mg^{2+}-ions. The ions can diffuse very quickly to the energetically most favorable position along the filament, arranging the attractive interaction between them, without having to bind specifically. These counterion interactions have a much higher probability due to their unspecific nature, leading to a significantly faster bundling process.

Bibliography

[1] B. Alberts, A. Johnson, J. Lewis, M. Raff, K. Roberts, and P. Walter. *Molecular Biology of the Cell*. Garland Science, 5th edition, 2008.

[2] T. E. Angelini, H. Liang, W. Wriggers, and G. C. L. Wong. Like-charge attraction between polyelectrolytes induced by counterion charge density waves. *Proceedings of the National Academy of Sciences of the United States of America*, 100(15):8634–8637, July 2003.

[3] N. J. Anthis and I. D. Campbell. The tail of integrin activation. *Trends in biochemical sciences*, 2011.

[4] S.-i. Aota, M. Nomizu, and K. M. Yamada. The short amino acid sequence Pro-His-Ser-Arg-Asn in human fibronectin enhances cell-adhesive function. *Journal of Biological Chemistry*, 269(40):24756–24761, 1994.

[5] M. Arnold, E. A. Cavalcanti-Adam, R. Glass, J. Blümmel, W. Eck, M. Kantlehner, H. Kessler, and J. P. Spatz. Activation of integrin function by nanopatterned adhesive interfaces. *Chemphyschem : a European journal of chemical physics and physical chemistry*, 5(3):383–388, Mar. 2004.

[6] M. Barczyk, S. Carracedo, and D. Gullberg. Integrins. *Cell and tissue research*, 339(1):269–280, 2010.

[7] C. Barentin, Y. Sawada, and J.-P. Rieu. An iterative method to calculate forces exerted by single cells and multicellular assemblies from the detection of deformations of flexible substrates. *European Biophysics Journal*, 35(4):328–339, Mar. 2006.

[8] G. I. Bell. Models for the specific adhesion of cells to cells. *Science (New York, NY)*, 200(4342):618–627, 1978.

[9] D. ben Avraham and M. M. Tirion. Dynamic and elastic properties of F-actin: a normal-modes analysis. *Biophysical Journal*, 68(4):15–15, Mar. 1995.

[10] C. P. Brangwynne, G. H. Koenderink, E. Barry, Z. Dogic, F. C. MacKintosh, and D. A. Weitz. Bending Dynamics of Fluctuating Biopolymers Probed by Automated High-Resolution Filament Tracking. *Biophysical Journal*, 93(1):14–14, June 2007.

[11] I. F. Burgess. The mode of action of dimeticone 4Pediculus capitis. *BMC Pharmacology*, 9:3, 2009.

[12] J. P. Butler, I. M. Tolić-Nørrelykke, B. Fabry, and J. J. Fredberg. Traction fields, moments, and strain energy that cells exert on their surroundings. *American Journal of Physiology - Cell Physiology*, 282(3):C595–C605, Feb. 2002.

[13] A. d. Campo and C. Greiner. SU-8: a photoresist for high-aspect-ratio and 3D submicron lithography. *Journal of Micromechanics and Microengineering*, 17(6):R81–R95, May 2007.

[14] C. V. Carman and T. A. Springer. Integrin avidity regulation: are changes in affinity and conformation underemphasized? *Current opinion in cell biology*, 15(5):10–10, Sept. 2003.

[15] E. A. Cavalcanti-Adam, T. Volberg, A. Micoulet, H. Kessler, B. Geiger, and J. P. Spatz. Cell spreading and focal adhesion dynamics are regulated by spacing of integrin ligands. *Biophysical Journal*, 92(8):2964–2974, Apr. 2007.

[16] J.-W. Chu and G. A. Voth. Allostery of actin filaments: molecular dynamics simulations and coarse-grained analysis. *Proceedings of the National Academy of Sciences of the United States of America*, 102(37):13111–13116, Sept. 2005.

[17] M. Cohen, E. Klein, B. Geiger, and L. Addadi. Organization and Adhesive Properties of the Hyaluronan Pericellular Coat of Chondrocytes and Epithelial Cells. *Biophysical Journal*, 85(3):10–10, Aug. 2003.

[18] D. L. Coleman, D. E. Gregonis, and J. D. Andrade. Blood-materials interactions: the minimum interfacial free energy and the optimum polar/apolar ratio hypotheses. *Journal of Biomedical Materials Research Part A*, 16(4):381–398, June 1982.

[19] J. Colombelli, A. Besser, H. Kress, E. G. Reynaud, P. Girard, E. Caussinus, U. Haselmann, J. V. Small, U. S. Schwarz, and E. H. K. Stelzer. Mechanosensing in actin stress fibers revealed by a close correlation between force and protein localization. *Journal of cell science*, 122(11):1928–1928, May 2009.

[20] J. C. Crocker and D. Grier. Methods of Digital Video Microscopy for Colloidal Studies. *Journal of colloid and interface science*, 179(1):13–13, Apr. 1996.

[21] P. Dancker, I. Löw, W. Hasselbach, and T. Wieland. Interaction of actin with phalloidin: Polymerization and stabilization of F-actin. *Biochimica et Biophysica Acta (BBA)-Protein Structure*, 400(2):407–414, Aug. 1975.

[22] E. H. J. Danen, P. Sonneveld, C. Brakebusch, R. Fässler, and A. Sonnenberg. The fibronectin-binding integrins alpha5beta1 and alphavbeta3 differentially modulate RhoA-GTP loading, organization of cell matrix adhesions, and fibronectin fibrillogenesis. *The Journal of cell biology*, 159(6):1071–1086, Dec. 2002.

[23] N. O. Deakin and C. E. Turner. Paxillin comes of age. *Journal of cell science*, 121(Pt 15):2435–2444, July 2008.

[24] M. Dembo, T. Oliver, A. Ishihara, and K. Jacobson. Imaging the traction stresses exerted by locomoting cells with the elastic substratum method. *Biophysical Journal*, 70(4):2008–2022, 1996.

[25] M. Dembo and Y. l. Wang. Stresses at the Cell-to-Substrate Interface during Locomotion of Fibroblasts. *Biophysical Journal*, 76(4):10–10, Mar. 1999.

[26] R. Dominguez and K. C. Holmes. Actin Structure and Function. *Annual Review of Biophysics*, 40(1):169–186, June 2011.

[27] C. G. Dos Remedios, D. Chhabra, M. Kekic, I. V. Dedova, M. Tsubakihara, D. A. Berry, and N. J. Nosworthy. Actin binding proteins: regulation of cytoskeletal microfilaments. *Physiological reviews*, 83(2):433–473, Apr. 2003.

[28] O. du Roure, A. Saez, A. Buguin, R. H. Austin, P. Chavrier, P. Silberzan, P. Siberzan, and B. Ladoux. Force mapping in epithelial cell migration. *Proceedings of the National Academy of Sciences of the United States of America*, 102(7):2390–2395, Feb. 2005.

[29] D. C. Duffy, J. C. McDonald, O. J. A. Schueller, and G. M. Whitesides. Rapid Prototyping of Microfluidic Systems in Poly(dimethylsiloxane). *Analytical Chemistry*, 70(23):4974–4984, Dec. 1998.

[30] T. Erdmann and U. S. Schwarz. Stability of adhesion clusters under constant force. *Physical review letters*, 92(10):108102–108102, Mar. 2004.

[31] T. Erdmann and U. S. Schwarz. Bistability of cell-matrix adhesions resulting from nonlinear receptor-ligand dynamics. *Biophysical Journal*, 91(6):L60–2, Sept. 2006.

[32] M. Evangelista, S. Zigmond, and C. Boone. Formins: signaling effectors for assembly and polarization of actin filaments. *Journal of cell science*, 116(Pt 13):2603–2611, June 2003.

[33] E. Evans and K. Ritchie. Dynamic strength of molecular adhesion bonds. *Biophysical Journal*, 72(4):1541–1555, 1997.

[34] H. Faulstich, S. Zobeley, D. Heintz, and G. Drewes. Probing the phalloidin binding site of actin. *FEBS letters*, 318(3):218–222, 1993.

[35] M. J. Footer, J. W. J. Kerssemakers, J. A. Theriot, and M. Dogterom. Direct measurement of force generation by actin filament polymerization using an optical trap. *Proceedings of the National Academy of Sciences of the United States of America*, 104(7):2181–2186, Feb. 2007.

[36] C. Frieden. Actin and tubulin polymerization: the use of kinetic methods to determine mechanism. *Annual Review of Biophysics and Biophysical Chemistry*, 14(1):189–210, June 1985.

[37] J. C. Friedland, M. H. Lee, and D. Boettiger. Mechanically Activated Integrin Switch Controls alpha5beta1 Function. *Science (New York, NY)*, 323(5914):642–644, Jan. 2009.

[38] E. Frixione. Recurring views on the structure and function of the cytoskeleton: a 300-year epic. *Cell Motility and the Cytoskeleton*, 46(2):73–94, May 2000.

[39] J. Fu, Y.-K. Wang, M. T. Yang, R. A. Desai, X. Yu, Z. Liu, and C. S. Chen. Mechanical regulation of cell function with geometrically modulated elastomeric substrates. *Nature Methods*, 7(9):733–736, Aug. 2010.

[40] I. Fujiwara, D. Vavylonis, and T. D. Pollard. Polymerization kinetics of ADP- and ADP-Pi-actin determined by fluorescence microscopy. *Proceedings of the National Academy of Sciences of the United States of America*, 104(21):8827–8832, May 2007.

[41] C. G. Galbraith and M. P. Sheetz. A micromachined device provides a new bend on fibroblast traction forces. *Proceedings of the National Academy of Sciences of the United States of America*, 94(17):9114–9118, Aug. 1997.

[42] B. Geiger, A. Bershadsky, R. Pankov, and K. M. Yamada. Transmembrane crosstalk between the extracellular matrix and the cytoskeleton : Abstract : Nature Reviews Molecular Cell Biology. *Nature Reviews Molecular Cell Biology*, 2(11):793–805, Nov. 2001.

[43] B. Geiger, J. P. Spatz, and A. D. Bershadsky. Environmental sensing through focal adhesions. *Nature Reviews Molecular Cell Biology*, 10(1):21–33, Jan. 2009.

[44] S. Ghassemi, G. Meacci, S. Liu, A. A. Gondarenko, A. Mathur, P. Roca-Cusachs, M. P. Sheetz, and J. Hone. Cells test substrate rigidity by local contractions on submicrometer pillars. *Proceedings of the National Academy of Sciences of the United States of America*, pages –, Mar. 2012.

[45] S. Gibson, R. J. Hubbold, J. Cook, and T. L. J. Howard. Interactive reconstruction of virtual environments from video sequences. *Computers & Graphics*, 27(2):293–301, Apr. 2003.

[46] D. Goodsell. Integrin. Biological Macromolecular Resource, Feb. 2011.

[47] S. V. Graeter, J. Huang, N. Perschmann, M. López-García, H. Kessler, J. Ding, and J. P. Spatz. Mimicking cellular environments by nanostructured soft interfaces. *Nano Letters*, 7(5):1413–1418, Apr. 2007.

[48] A. M. Greiner, B. Richter, and M. Bastmeyer. Micro-Engineered 3D Scaffolds for Cell Culture Studies. *Macromolecular Bioscience*, 12(10):1301–1314, Sept. 2012.

[49] N. Grønbech-Jensen, R. Mashl, R. Bruinsma, and W. Gelbart. Counterion-Induced Attraction between Rigid Polyelectrolytes. *Physical review letters*, 78(12):2477–2480, Mar. 1997.

[50] C. Hansen and S. R. Quake. Microfluidics in structural biology: smaller, faster... better. *Current Opinion in Structural Biology*, 13(5):7–7, Sept. 2003.

[51] P. Harder, M. Grunze, R. Dahint, G. M. Whitesides, and P. E. Laibinis. Molecular conformation in oligo (ethylene glycol)-terminated self-assembled monolayers on gold and silver surfaces determines their ability to resist protein adsorption. *The Journal of Physical Chemistry B*, 102(2):426–436, 1998.

[52] A. K. Harris, P. Wild, and D. Stopak. Silicone rubber substrata: a new wrinkle in the study of cell locomotion. *Science (New York, NY)*, 208(4440):177–179, 1980.

[53] J. P. Heath. Behaviour and structure of the leading lamella in moving fibroblasts. I. Occurrence and centripetal movement of arc-shaped microfilament bundles beneath the dorsal cell surface. *Journal of cell science*, 60:331–354, Feb. 1983.

[54] J. P. Heath and G. A. Dunn. Cell to substratum contacts of chick fibroblasts and their relation to the microfilament system. A correlated interference-reflexion and high-voltage electron-microscope study. *Journal of cell science*, 29:197–212, Jan. 1978.

[55] D. Heckmann, A. Meyer, B. Laufer, G. Zahn, R. Stragies, and H. Kessler. Rational design of highly active and selective ligands for the alpha5beta1 integrin receptor. *ChemBioChem*, 9(9):1397–1407, June 2008.

[56] H. Hirata, H. Tatsumi, and M. Sokabe. Mechanical forces facilitate actin polymerization at focal adhesions in a zyxin-dependent manner. *Journal of cell science*, 2008.

[57] L. M. Hoffman, C. C. Jensen, S. Kloeker, C.-L. A. Wang, M. Yoshigi, and M. C. Beckerle. Genetic ablation of zyxin causes Mena/VASP mislocalization, increased motility, and deficits in actin remodeling. *The Journal of cell biology*, 172(5):771–782, Feb. 2006.

[58] T. W. Houk and K. Ue. The measurement of actin concentration in solution: a comparison of methods. *Analytical biochemistry*, 62(1):66–74, Nov. 1974.

[59] J. Huang, S. V. Grater, F. Corbellini, S. Rinck, E. Bock, R. Kemkemer, H. Kessler, J. Ding, and J. P. Spatz. Impact of order and disorder in RGD nanopatterns on cell adhesion. *Nano Letters*, 9(3):1111–1116, Mar. 2009.

[60] J. D. Humphries, A. Byron, and M. J. Humphries. Integrin ligands at a glance. *Journal of cell science*, 2006.

[61] R. O. Hynes. Cell adhesion: old and new questions. *Trends in Cell Biology*, 9(12):M33–M37, Nov. 1999.

[62] R. O. Hynes. Integrins: bidirectional, allosteric signaling machines. *Cell*, 110(6):673–687, Sept. 2002.

[63] H. Isambert, P. Venier, A. C. Maggs, A. Fattoum, R. Kassab, D. Pantaloni, and M. F. Carlier. Flexibility of actin filaments derived from thermal fluctuations. Effect of bound nucleotide, phalloidin, and muscle regulatory proteins. *Journal of Biological Chemistry*, 270(19):11437–11444, May 1995.

[64] R. F. Ismagilov. Integrated microfluidic systems. *Angewandte Chemie (International ed. in English)*, 42(35):4130–4132, Sept. 2003.

[65] P. Janmey, J. Tang, and C. Schmidt. Actin filaments. *Supramolecular Assemblies*, 2001.

[66] S. I. Jeon, J. H. Lee, J. D. Andrade, and P. G. De Gennes. Protein—surface interactions in the presence of polyethylene oxide: I. Simplified theory. *Journal of colloid and interface science*, 142(1):149–158, 1991.

[67] P. Kanchanawong, G. Shtengel, A. M. Pasapera, E. B. Ramko, M. W. Davidson, H. F. Hess, and C. M. Waterman. Nanoscale architecture of integrin-based cell adhesions. *Nature*, 468(7323):580–584, Nov. 2010.

[68] F. Klein, B. Richter, T. Striebel, C. M. Franz, G. von Freymann, M. Wegener, and M. Bastmeyer. Two-Component Polymer Scaffolds for Controlled Three-Dimensional Cell Culture. *Advanced materials (Deerfield Beach, Fla)*, 23(11):1341–1345, Mar. 2011.

[69] F. Klein, T. Striebel, J. Fischer, Z. Jiang, C. M. Franz, G. von Freymann, M. Wegener, and M. Bastmeyer. Elastic Fully Three-dimensional Microstructure Scaffolds for Cell Force Measurements. *Advanced Materials*, 22(8):868–871, Feb. 2010.

[70] F. Kong, A. J. Garcia, A. P. Mould, M. J. Humphries, and C. Zhu. Demonstration of catch bonds between an integrin and its ligand. *The Journal of cell biology*, 185(7):1275–1284, June 2009.

[71] D. R. Kovar and T. D. Pollard. Insertional assembly of actin filament barbed ends in association with formins produces piconewton forces. *Proceedings of the National Academy of Sciences of the United States of America*, 101(41):14725–14730, Oct. 2004.

[72] H. A. Kramers. Brownian motion in a field of force and the diffusion model of chemical reactions. *Physica*, 7(4):284–304, Apr. 1940.

[73] T. Kuehne, R. Lipowsky, and J. Kierfeld. Zipping mechanism for force generation by growing filament bundles. *EPL (Europhysics Letters)*, 86(6):68002, 2009.

[74] L. D. Landau and E. M. Lifschitz. Lehrbuch der Theoretischen Physik VII Elastizitätstheorie. Akademie Verlag, Berlin, Jan. 1991.

[75] A. Lau, D. Lukatsky, P. Pincus, and S. Safran. Charge fluctuations and counterion condensation. *Physical Review E*, 65(5):051502, Apr. 2002.

[76] T. Lecuit, P.-F. Lenne, and E. Munro. Force generation, transmission, and integration during cell and tissue morphogenesis. *Annual review of cell and developmental biology*, 27:157–184, Nov. 2011.

[77] J. H. Lee, H. B. Lee, and J. D. Andrade. Blood compatibility of polyethylene oxide surfaces. *Progress in Polymer Science*, 20(6):37–37, Dec. 1994.

[78] J. N. Lee, X. Jiang, D. Ryan, and G. M. Whitesides. Compatibility of mammalian cells on surfaces of poly(dimethylsiloxane). *Langmuir*, 20(26):11684–11691, Dec. 2004.

[79] T. P. Lele, J. Pendse, S. Kumar, M. Salanga, J. Karavitis, and D. E. Ingber. Mechanical forces alter zyxin unbinding kinetics within focal adhesions of living cells. *Journal of Cellular Physiology*, 207(1):187–194, Apr. 2006.

[80] C. A. Lemmon, N. J. Sniadecki, S. A. Ruiz, J. L. Tan, L. H. Romer, and C. S. Chen. Shear force at the cell-matrix interface: enhanced analysis for microfabricated post array detectors. *Mechanics & Chemistry of Biosystems*, 2(1):1–16, Dec. 2004.

[81] B. Li, L. Zhuang, and B. Trueb. Zyxin interacts with the SH3 domains of the cytoskeletal proteins LIM-nebulette and Lasp-1. *Journal of Biological Chemistry*, 279(19):20401–20410, May 2004.

[82] G. L. Lin, D. M. Cohen, R. A. Desai, M. T. Breckenridge, L. Gao, M. J. Humphries, and C. S. Chen. Activation of beta 1 but not beta 3 integrin increases cell traction forces. *FEBS letters*, pages –, Feb. 2013.

[83] A. Lindner. *Kraftsensoren im Nanonewton-Bereich: Biofunktionalisierte Mikrosaeulen aus Poly-Ethylenglykol zur Untersuchung fusionierender Mitosespindeln*. PhD thesis, Universität Heidelberg, Sept. 2009.

[84] X. Liu and G. H. Pollack. Mechanics of F-Actin Characterized with Microfabricated Cantilevers. *Biophysical Journal*, 83(5):11–11, Oct. 2002.

[85] H. Lodish, A. Berk, S. L. Zipursky, P. Matsudaira, D. Baltimore, and J. Darnell. *Molecular Cell Biology*, volume 4. W H Freeman, New York, Jan. 2000.

[86] T. Lohmüller, D. Aydin, M. Schwieder, C. Morhard, I. Louban, C. Pacholski, and J. P. Spatz. Nanopatterning by block copolymer micelle nanolithography and bioinspired applications. *Biointerphases*, 6(1):MR1–MR1, Feb. 2011.

[87] I. Louban. *Mimicking the Cellular Environment: effects of elastic nanopatterned substrates on integrin-mediated cellular interactions* . PhD thesis, Universität Heidelberg, Nov. 2009.

[88] J. C. Love, D. B. Wolfe, H. O. Jacobs, and G. M. Whitesides. Microscope Projection Photolithography for Rapid Prototyping of Masters with Micron-Scale Features for Use in Soft Lithography. *Langmuir*, 17(19):6005–6012, Sept. 2001.

[89] S. MacLean-Fletcher and T. D. Pollard. Identification of a factor in conventional muscle actin preparations which inhibits actin filament self-association. *Biochemical and Biophysical Research Communications*, 96(1):18–27, Sept. 1980.

[90] G. S. Manning. The molecular theory of polyelectrolyte solutions with applications to the electrostatic properties of polynucleotides. *Quarterly Reviews of Biophysics*, 11(2):179–246, Apr. 1978.

[91] R. Maoz and J. Sagiv. On the formation and structure of self-assembling monolayers. I. A comparative atr-wettability study of Langmuir—Blodgett and adsorbed films on flat substrates and glass microbeads. *Journal of colloid and interface science*, 100(2):465–496, 1984.

[92] L. Marinelli, A. Meyer, D. Heckmann, A. Lavecchia, E. Novellino, and H. Kessler. Ligand binding analysis for human alpha5beta1 integrin: strategies for designing new alpha5beta1 integrin antagonists. *Journal of medicinal chemistry*, 48(13):4204–4207, June 2005.

[93] B. R. McCullough, L. Blanchoin, J.-L. Martiel, and E. M. De La Cruz. Cofilin Increases the Bending Flexibility of Actin Filaments: Implications for Severing and Cell Mechanics. *Journal of molecular biology*, 381(3):9–9, Sept. 2008.

[94] R. L. Meeusen and W. Z. Cande. N-ethylmaleimide-modified heavy meromyosin. A probe for actomyosin interactions. *The Journal of cell biology*, 82(1):57, July 1979.

[95] R. K. Meyer and U. Aebi. Bundling of actin filaments by alpha-actinin depends on its molecular length. *The Journal of cell biology*, 110(6):2013–2024, May 1990.

[96] N. Michael Green. Avidin and streptavidin. In M. W. Bayer and E. A, editors, *Methods in Enzymology*, pages 51–67. Academic Press, 1990.

[97] A. Mogilner and G. Oster. Cell motility driven by actin polymerization. *Biophysical Journal*, 71(6):3030–3045, 1996.

[98] A. Mogilner and B. Rubinstein. The physics of filopodial protrusion. *Biophysical Journal*, 89(2):782–795, 2005.

[99] C. Mohrdieck, F. Dalmas, E. Arzt, R. Tharmann, M. M. A. E. Claessens, A. R. Bausch, A. Roth, E. Sackmann, C. H. J. Schmitz, J. Curtis, W. Roos, S. Schulz, K. Uhrig, and J. P. Spatz. Biomimetic models of the actin cytoskeleton. *Small (Weinheim an der Bergstrasse, Germany)*, 3(6):1015–1022, June 2007.

[100] M. R. Morgan, A. Byron, M. J. Humphries, and M. D. Bass. Giving off mixed signals-Distinct functions of $\alpha_5\beta_1$ and $\alpha_v\beta_3$ integrins in regulating cell behaviour. *IUBMB Life*, 61(7):731–738, July 2009.

[101] M. Moser, K. R. Legate, R. Zent, and R. Fässler. The tail of integrins, talin, and kindlins. *Science (New York, NY)*, 324(5929):895–899, May 2009.

[102] S. Munevar, Y. Wang, and M. Dembo. Traction force microscopy of migrating normal and H-ras transformed 3T3 fibroblasts. *Biophysical Journal*, 80(4):1744–1757, Apr. 2001.

[103] D. Nelson and B. Halperin. Dislocation-mediated melting in two dimensions. *Physical Review B*, 19(5):2457–2484, Mar. 1979.

[104] P. C. Nicolson and J. Vogt. Soft contact lens polymers: an evolution. *Biomaterials*, 22(24):3273–3283, Nov. 2001.

[105] D. A. Nix and M. C. Beckerle. Nuclear-cytoplasmic shuttling of the focal contact protein, zyxin: a potential mechanism for communication between sites of cell adhesion and the nucleus. *The Journal of cell biology*, 138(5):1139–1147, Sept. 1997.

[106] D. A. Nix, J. Fradelizi, S. Bockholt, B. Menichi, D. Louvard, E. Friederich, and M. C. Beckerle. Targeting of zyxin to sites of actin membrane interaction and to the nucleus. *Journal of Biological Chemistry*, 276(37):34759–34767, Sept. 2001.

[107] P. W. Oakes, Y. Beckham, J. Stricker, and M. L. Gardel. Tension is required but not sufficient for focal adhesion maturation without a stress fiber template. *The Journal of cell biology*, 196(3):363–374, Feb. 2012.

[108] A. Olziersky, P. Barquinha, A. Vilà, L. Pereira, G. Gonçalves, E. Fortunato, R. Martins, and J. R. Morante. Insight on the SU-8 resist as passivation layer for transparent Ga[sub 2]O[sub 3]–In[sub 2]O[sub 3]–ZnO thin-film transistors. *Journal of Applied Physics*, 108(6):064505–064505–7, 2010.

[109] F. Oosawa. Interaction between parallel rodlike macroions. *Biopolymers*, 6(11):1633–1647, Nov. 1968.

[110] A. Ott, M. Magnasco, A. Simon, and A. Libchaber. Measurement of the persistence length of polymerized actin using fluorescence microscopy. *Physical review. E, Statistical physics, plasmas, fluids, and related interdisciplinary topics*, 48(3):R1642–R1645, Sept. 1993.

[111] R. N. Palchesko, L. Zhang, Y. Sun, and A. W. Feinberg. Development of polydimethylsiloxane substrates with tunable elastic modulus to study cell mechanobiology in muscle and nerve. *PloS one*, 7(12):e51499–e51499, Dec. 2011.

[112] J. D. Pardee and J. A. Spudich. Purification of Muscle Actin. *Methodes of Enzymology*, pages 164–181, Jan. 1982.

[113] R. J. Pelham and Y. l. Wang. Cell locomotion and focal adhesions are regulated by substrate flexibility. *Proceedings of the National Academy of Sciences of the United States of America*, 94(25):13661–13665, Dec. 1997.

[114] S. Pellegrin and H. Mellor. Actin stress fibres. *Journal of cell science*, 120(Pt 20):3491–3499, Oct. 2007.

[115] O. Pelletier, E. Pokidysheva, L. S. Hirst, N. Bouxsein, Y. Li, and C. R. Safinya. Structure of actin cross-linked with alpha-actinin: a network of bundles. *Physical review letters*, 91(14):148102–148102, Oct. 2003.

[116] N. Perschmann. *Synthese und quantitative Analyse von strukturierten und funktionellen Hydrogelsystemen zur Regulierung der Adhäsionseigenschaften unterschiedlicher Zellphänotypen an Grenzflächen.* PhD thesis, Universität Heidelberg, Dec. 2010.

[117] A. J. Pertsin and M. Grunze. Computer simulation of water near the surface of oligo (ethylene glycol)-terminated alkanethiol self-assembled monolayers. *Langmuir*, 16(23):8829–8841, 2000.

[118] C. S. Peskin, G. M. Odell, and G. F. Oster. Cellular motions and thermal fluctuations: the Brownian ratchet. *Biophysical Journal*, 65(1):9–9, June 1993.

[119] S. Petronis, J. Gold, and B. Kasemo. Microfabricated force-sensitive elastic substrates for investigation of mechanical cell–substrate interactions. *Journal of Micromechanics and Microengineering*, 13(6):900–913, Aug. 2003.

[120] S. V. Plotnikov, A. M. Pasapera, B. Sabass, and C. M. Waterman. Force Fluctuations within Focal Adhesions Mediate ECM-Rigidity Sensing to Guide Directed Cell Migration. *Cell*, 151(7):1513–1527, Dec. 2012.

[121] T. D. Pollard. Rate constants for the reactions of ATP- and ADP-actin with the ends of actin filaments. *The Journal of cell biology*, 103(6 Pt 2):2747–2754, Nov. 1986.

[122] T. D. Pollard and G. G. Borisy. Cellular Motility Driven by Assembly and Disassembly of Actin Filaments. *Cell*, 112(4):13–13, Feb. 2003.

[123] T. D. Pollard and J. A. Cooper. Actin and actin-binding proteins. A critical evaluation of mechanisms and functions. *Annual review of biochemistry*, 55(1):987–1035, 1986.

[124] D. C. Pregibon, K. Y. Suh, M. Toner, J. Seong, P. S. Doyle, A. Khademhosseini, P. E. Laibinis, and R. Langer. A simple soft lithographic route to fabrication of poly(ethylene glycol) microstructures for protein and cell patterning. *Biomaterials*, 25(3):7–7, Jan. 2004.

[125] D. C. Pregibon, M. Toner, and P. S. Doyle. Magnetically and biologically active bead-patterned hydrogels. *Langmuir*, 22(11):5122–5128, May 2006.

[126] J. Ray and G. S. Manning. An attractive force between two rodlike polyions mediated by the sharing of condensed counterions. *Langmuir*, 10(7):2450–2461, July 1994.

[127] F. Rechenmacher, S. Neubauer, J. Polleux, C. Mas-Moruno, M. De Simone, E. A. Cavalcanti-Adam, J. P. Spatz, R. Fässler, and H. Kessler. Functionalizing αvβ3- or α5β1-selective integrin antagonists for surface coating: a method to discriminate integrin subtypes in vitro. *Angewandte Chemie (International ed. in English)*, 52(5):1572–1575, Jan. 2013.

[128] M. Reinhard, J. Zumbrunn, D. Jaquemar, M. Kuhn, U. Walter, and B. Trueb. An α-actinin binding site of zyxin is essential for subcellular zyxin localization and α-actinin recruitment. *Journal of Biological Chemistry*, 274(19):13410–13418, 1999.

[129] A. Revzin, R. J. Russell, V. K. Yadavalli, W.-G. Koh, C. Deister, D. D. Hile, M. B. Mellott, and M. V. Pishko. Fabrication of Poly(ethylene glycol) Hydrogel Microstructures Using Photolithography. *Langmuir*, 17(18):5440–5447, Sept. 2001.

[130] D. Riveline, E. Zamir, N. Q. Balaban, U. S. Schwarz, T. Ishizaki, S. Narumiya, Z. Kam, B. Geiger, and A. D. Bershadsky. Focal contacts as mechanosensors: externally applied local mechanical force induces growth of focal contacts by an mDia1-dependent and ROCK-independent mechanism. *The Journal of cell biology*, 153(6):1175–1186, June 2001.

[131] P. Roca-Cusachs, N. C. Gauthier, A. Del Rio, and M. P. Sheetz. Clustering of alpha(5)beta(1) integrins determines adhesion strength whereas alpha(v)beta(3) and talin enable mechanotransduction. *Proceedings of the National Academy of Sciences of the United States of America*, 106(38):16245–16250, Sept. 2009.

[132] W. Roos. *Biomimetic cytoskeleton assemblies and living cells on micropillar force sensor array.* PhD thesis, Universität Heidelberg, Dec. 2004.

[133] W. H. Roos, A. Roth, J. Konle, H. Presting, E. Sackmann, and J. P. Spatz. Freely suspended actin cortex models on arrays of microfabricated pillars. *Chemphyschem : a European journal of chemical physics and physical chemistry*, 4(8):872–877, Aug. 2003.

[134] O. Rossier, V. Octeau, J.-B. Sibarita, C. Leduc, B. Tessier, D. Nair, V. Gatterdam, O. Destaing, C. Albigès-Rizo, R. Tampé, L. Cognet, D. Choquet, B. Lounis, and G. Giannone. Integrins β1 and β3 exhibit distinct dynamic nanoscale organizations inside focal adhesions. *Nature cell biology*, 14(10):1057–1067, Sept. 2012.

[135] B. Rühle. Functionalized PEG Pillar Arrays acting as Force Sensors for the Investigation of Mitotic Spindle Mechanics. Master's thesis, Universität Heidelberg, Dec. 2008.

[136] E. Ruoslahti. RGD AND OTHER RECOGNITION SEQUENCES FOR INTEGRINS. *Annual review of cell and developmental biology*, 12(1):697–715, Nov. 1996.

[137] E. Ruoslahti and M. D. Pierschbacher. Arg-Gly-Asp: A versatile cell recognition signal. *Cell*, 44(4):517–518, Feb. 1986.

[138] E. Sackmann and R. F. Bruinsma. Cell adhesion as wetting transition? *Chemphyschem : a European journal of chemical physics and physical chemistry*, 3(3):262–269, Mar. 2002.

[139] A. Saez, E. Anon, M. Ghibaudo, O. du Roure, J.-M. Di Meglio, P. Hersen, P. Silberzan, A. Buguin, and B. Ladoux. Traction forces exerted by epithelial cell sheets. *Journal of Physics: Condensed Matter*, 22(19):194119–194119, May 2010.

[140] I. F. Sbalzarini and P. Koumoutsakos. Feature point tracking and trajectory analysis for video imaging in cell biology. *Journal of Structural Biology*, 151(2):182–195, Aug. 2005.

[141] J. Schindelin, I. Arganda-Carreras, E. Frise, V. Kaynig, M. Longair, T. Pietzsch, S. Preibisch, C. Rueden, S. Saalfeld, B. Schmid, J.-Y. Tinevez, D. J. White, V. Hartenstein, K. Eliceiri, P. Tomancak, and A. Cardona. Fiji: an open-source platform for biological-image analysis. *Nature Methods*, 9(7):676–682, July 2012.

[142] U. S. Schwarz, N. Q. Balaban, D. Riveline, A. Bershadsky, B. Geiger, and S. A. Safran. Calculation of Forces at Focal Adhesions from Elastic Substrate Data: The Effect of Localized Force and the Need for Regularization. *Biophysical Journal*, 83(3):15–15, Aug. 2002.

[143] U. S. Schwarz, T. Erdmann, and I. B. Bischofs. Focal adhesions as mechanosensors: the two-spring model. *Biosystems*, 83(2-3):225–232, Jan. 2006.

[144] M. Schwieder. *Hierarchical Nanopatterns for Cell Adhesion Studies*. PhD thesis, Universität Heidelberg, Mar. 2009.

[145] U. Seifert. Rupture of multiple parallel molecular bonds under dynamic loading. *Physical review letters*, 84(12):2750–2753, Mar. 2000.

[146] U. Seifert. Dynamic strength of adhesion molecules: Role of rebinding and self-consistent rates. *Europhysics Letters (EPL)*, 58(5):792–798, Jan. 2002.

[147] C. Selhuber-Unkel, T. Erdmann, M. Lopez-García, H. Kessler, U. S. Schwarz, and J. P. Spatz. Cell adhesion strength is controlled by intermolecular spacing of adhesion receptors. *Biophysical Journal*, 98(4):543–551, Feb. 2010.

[148] J.-H. Seo, K. Sakai, and N. Yui. Adsorption state of fibronectin on poly(dimethylsiloxane) surfaces with varied stiffness can dominate adhesion density of fibroblasts. *Acta Biomaterialia*, pages –, Oct. 2012.

[149] S. J. Shattil, C. Kim, and M. H. Ginsberg. The final steps of integrin activation: the end game. *Nature Reviews Molecular Cell Biology*, 11(4):288–300, Mar. 2010.

[150] J. V. Small, K. Rottner, I. Kaverina, and K. I. Anderson. Assembling an actin cytoskeleton for cell attachment and movement. *Biochimica et Biophysica Acta (BBA) - Bioenergetics*, 1404(3):271–281, Sept. 1998.

[151] Y.-A. Song, C. Batista, R. Sarpeshkar, and J. Han. Rapid fabrication of microfluidic polymer electrolyte membrane fuel cell in PDMS by surface patterning of perfluorinated ion-exchange resin. *Journal of Power Sources*, 183(2):4–4, Aug. 2008.

[152] J. A. Spudich and S. Watt. The Regulation of Rabbit Skeletal Muscle Contraction. *Journal of Biological Chemistry*, 1971.

[153] M. O. Steinmetz, D. Stoffler, A. Hoenger, A. Bremer, and U. Aebi. Actin: from cell biology to atomic detail. *Journal of Structural Biology*, 119(3):295–320, Aug. 1997.

[154] M. Streichfuss. *Force Generation by Bundle Formation of Two Actin Filaments* . PhD thesis, Universität Heidelberg, Feb. 2013.

[155] M. Streichfuss, F. Erbs, K. Uhrig, R. Kurre, A. E.-M. Clemen, C. H. J. Böhm, T. Haraszti, and J. P. Spatz. Measuring forces between two single actin filaments during bundle formation. *Nano Letters*, 11(9):3676–3680, Sept. 2011.

[156] Z. Sun, S. Huang, Z. Li, and G. A. Meininger. Zyxin is involved in regulation of mechanotransduction in arteriole smooth muscle cells. *Frontiers in Physiology*, 3, 2012.

[157] J. L. Tan, J. Tien, D. M. Pirone, D. S. Gray, K. Bhadriraju, and C. S. Chen. Cells lying on a bed of microneedles: an approach to isolate mechanical force. *Proceedings of the National Academy of Sciences of the United States of America*, 100(4):1484–1489, Feb. 2003.

[158] L. Trichet, J. le Digabel, R. J. Hawkins, S. R. K. Vedula, M. Gupta, C. Ribrault, P. Hersen, R. Voituriez, and B. Ladoux. Evidence of a large-scale mechanosensing mechanism for cellular adaptation to substrate stiffness. *Proceedings of the National Academy of Sciences of the United States of America*, 109(18):6933–6938, Apr. 2012.

[159] K. Uhrig, R. Kurre, C. Schmitz, J. E. Curtis, T. Haraszti, A. E.-M. Clemen, and J. P. Spatz. Optical force sensor array in a microfluidic device based on holographic optical tweezers. *Lab on a Chip*, 9(5):661–668, Mar. 2009.

[160] Y. van Kooyk and C. G. Figdor. Avidity regulation of integrins: the driving force in leukocyte adhesion. *Current opinion in cell biology*, 12(5):542–547, Sept. 2000.

[161] J. van Mameren, K. C. Vermeulen, F. Gittes, and C. F. Schmidt. Leveraging Single Protein Polymers To Measure Flexural Rigidity. *The Journal of Physical Chemistry B*, 113(12):3837–3844, Mar. 2009.

[162] G. Velve-Casquillas, M. Le Berre, M. Piel, and P. T. Tran. Microfluidic tools for cell biological research. *Nano Today*, 2010.

[163] D. Vignjevic, D. Yarar, M. D. Welch, J. Peloquin, T. Svitkina, and G. G. Borisy. Formation of filopodia-like bundles in vitro from a dendritic network. *The Journal of cell biology*, 160(6):951–962, Mar. 2003.

[164] R. L. C. Wang, H. J. Kreuzer, and M. Grunze. Molecular Conformation and Solvation of Oligo(ethylene glycol)-Terminated Self-Assembled Monolayers and Their Resistance to Protein Adsorption. *The Journal of Physical Chemistry B*, 101(47):9767–9773, Nov. 1997.

[165] J. L. Wilbur, A. Kumar, H. A. Biebuyck, E. Kim, and G. M. Whitesides. Microcontact printing of self-assembled monolayers: applications in microfabrication. *Nanotechnology*, 7(4):452–457, Jan. 1996.

[166] Y. Xia and G. M. Whitesides. Soft lithography. *Annual review of materials science*, 28(1):153–184, 1998.

[167] Y. Xiang and D. A. LaVan. Analysis of soft cantilevers as force transducers. *Applied Physics Letters*, 90(13):133901, 2007.

[168] J.-P. Xiong, T. Stehle, R. Zhang, A. Joachimiak, M. Frech, S. L. Goodman, and M. A. Arnaout. Crystal structure of the extracellular segment of integrin alpha Vbeta3 in complex with an Arg-Gly-Asp ligand. *Science (New York, NY)*, 296(5565):151–155, Apr. 2002.

[169] J. Xu, W. H. Schwarz, J. A. Käs, T. P. Stossel, P. A. Janmey, and T. D. Pollard. Mechanical Properties of Actin Filament Networks Depend on Preparation, Polymerization Conditions, and Storage of Actin Monomers. *Biophysical Journal*, 74(5):10–10, Apr. 1998.

[170] T. Yeung, P. C. Georges, L. A. Flanagan, B. Marg, M. Ortiz, M. Funaki, N. Zahir, W. Ming, V. Weaver, and P. A. Janmey. Effects of substrate stiffness on cell morphology, cytoskeletal structure, and adhesion. *Cell Motility and the Cytoskeleton*, 60(1):24–34, Dec. 2004.

[171] M. Yoshigi, L. M. Hoffman, C. C. Jensen, H. J. Yost, and M. C. Beckerle. Mechanical force mobilizes zyxin from focal adhesions to actin filaments and regulates cytoskeletal reinforcement. *The Journal of cell biology*, 171(2):209–215, Oct. 2005.

[172] X. Yu and A. E. Carlsson. Multiscale Study of Counterion-Induced Attraction and Bundle Formation of F-Actin Using an Ising-like Mean-Field Model. *Biophysical Journal*, 85(6):12–12, Nov. 2003.

[173] R. Zaidel-Bar, C. Ballestrem, Z. Kam, and B. Geiger. Early molecular events in the assembly of matrix adhesions at the leading edge of migrating cells. *Journal of cell science*, 116(Pt 22):4605–4613, Nov. 2003.

[174] E. Zamir and B. Geiger. Components of cell-matrix adhesions. *Journal of cell science*, 114(20):3577–3579, 2001.

[175] E. Zamir and B. Geiger. Molecular complexity and dynamics of cell-matrix adhesions. *Journal of cell science*, 114(Pt 20):3583–3590, Oct. 2001.

[176] E. Zamir, M. Katz, Y. Posen, N. Erez, K. M. Yamada, B. Z. Katz, S. Lin, D. C. Lin, A. Bershadsky, Z. Kam, and B. Geiger. Dynamics and segregation of cell-matrix adhesions in cultured fibroblasts. *Nature cell biology*, 2(4):191–196, Mar. 2000.

Acknowledgment

Als Erstes möchte ich mich ganz herzlich bei Prof. Dr. Joachim P. Spatz dafür bedanken, dass er mir die Möglichkeit gegeben hat auf diesem spannenden und interdisziplinären Thema zu promovieren. Er gab mir all die nötigen Freiheiten und war doch immer erreichbar.

Prof. Dr. Ulrich S. Schwarz gilt mein Dank für seine bereitwillige Zusage als Zweitgutachter meiner Arbeit zu fungieren. Außerdem danke ich den weiteren Mitgliedern der Prüfungskommission, Prof. Dr. Ulrich Uwer und Prof. Dr. Karlheinz Meier, für ihre Zusagen.

Sehr bedanken möchte ich mich bei der gesamten Arbeitsgruppe Spatz, die alle gemeinsam für eine extrem kollegiales und angenehmes Arbeitsumfeld gesorgt haben. Dabei möchte ich mich besonders bei Tamás Haraszti und Ada Cavalcanti-Adam, sowohl für das fleißige Korrekturlesen meiner Arbeit, als auch für das immer offene Ohr bedanken. Sie haben mir immer mit Rat und Tat zur Seite gestanden. Aaron Lindner und Bastian Rühle danke ich dafür, dass Sie den Grundstein der PEG-Säulenherstellung gelegt haben, auf dem meine Arbeit beruht. Bei Rebecca Medda bedanke ich mich ~~auf gar keinen Fall~~ für die tatkräftige Hilfe beim Umgang mit dem "ganzen Zellkram" und der Korrektur meiner Arbeit. Für letzteres möchte ich auch Martin Streichfuss und Sebastian Rausch danken.

Für die Übernahme so mancher Laborarbeiten möchte ich noch herzlich Sigrid Riese (Zellkultur), Christine Mollenhauer (Aktinaufbereitung) und Yvonne Schön (Gold Nanostrukturen) danken.

Bei Jutta Hess, Elisabeth Pfeilmeier und Renate Ulshöfer bedanke ich mich für die Abnahme all der administrativen Aufgaben und die stets prompte Reaktion auf all meine Anfragen.

Nicht zuletzt bedanke ich mich bei meiner Familie. Meinen Eltern Christine und Amor Rahmouni denen ich all das was ich bin und erreicht habe verdanke. Ohne ihre bedingungslose Unterstützung wäre ich nie soweit gekommen. Natürlich danke ich auch meinen Schwestern Jamila und Delila, die ich trotz so manchem Zwist, immer in meinem Leben wissen will.

Der letzte Dank gilt meiner Frau Fatin Rahmouni, für ihre uneingeschränkte Unterstützung und dafür dass sie mir bald den wohl größten Wunsch meines Lebens erfüllen wird.

Hiermit erkläre ich, Sabri Rahmouni, dass ich die vorgelegte Dissertation selbst verfasst und nur die angegebenen Quellen und Hilfsmittel benutzt habe.

Heidelberg, den ....

Sabri Rahmouni